

2014

Modification of Adhesion and Friction by Surface Structuring

Ying Bai
Lehigh University

Follow this and additional works at: <http://preserve.lehigh.edu/etd>

 Part of the [Chemical Engineering Commons](#)

Recommended Citation

Bai, Ying, "Modification of Adhesion and Friction by Surface Structuring" (2014). *Theses and Dissertations*. Paper 1419.

This Dissertation is brought to you for free and open access by Lehigh Preserve. It has been accepted for inclusion in Theses and Dissertations by an authorized administrator of Lehigh Preserve. For more information, please contact preserve@lehigh.edu.

**MODIFICATION OF
ADHESION AND FRICTION BY
SURFACE STRUCTURING**

by

Ying Bai

A Dissertation

Presented to the Graduate and Research Committee

of Lehigh University

in Candidacy for the Degree of

Doctor of Philosophy

in

Chemical Engineering

Lehigh University

January 2014

Copyright by Ying Bai

2014

Certificate of Approval

Approved and recommended for acceptance as a dissertation in partial fulfillment of the requirements for the degree of Doctor of Philosophy.

Date

Professor Anand Jagota
Dissertation Advisor

Accepted Date

Committee Members:

Professor Manoj K. Chaudhury

Professor James F. Gilchrist

Professor Chung-Yuen Hui

Professor Richard P. Vinci

Acknowledgements

I wish to express my sincere thanks and appreciation to:

- Prof. Anand Jagota for his guidance and constant support as my academic advisor and mentor throughout the entire course of study.
- Prof. Chung-Yuen Hui for his helpful guidance and advice on many theoretical issues of this research, and for his endless support.
- Prof. Manoj Chaudhury, Prof. James Gilchrist and Prof. Richard Vinci for serving as my committee members, as well as their invaluable assistance and advice.
- Dr. Shilpi Vajpayee for her valuable training and suggestions early in this project.
- Dr. Congrui Jin for the collaboration in the study of electrostatic complementarity.
- Dr. Arun Singh for his preliminary experimental work in the study of shape complementarity, and Dr. Nichole Nadermann for helping me with the micro-fabrication process at Cornell NanoScale Science and Technology Facility.
- Mr. Bill Mushock for his assistance in using the SEM.
- My fellow graduate students and post-doctoral associates in our group for enlightening technical discussions, suggestions and most of all, their friendship.
- The Department of Energy and Michelin[®] International Corporation, for financial support.
- Finally, my parents, Jingsheng Bai and Danlei Liang for their love and support throughout my entire academic career.

Table of Contents

List of Figures	ix
List of Tables	xiv
Abstract	1
Chapter 1 Introduction	3
1.1 Adhesion selectivity by complementarity.....	4
1.1.1 Electrostatic complementarity	5
1.1.2 Shape complementarity	6
1.2 Controlled sliding friction.....	9
1.2.1 Friction on surface with spatial variation in property	10
1.2.2 How roughness affects friction on a structured surface	11
1.3 Outline.....	13
1.4 References.....	13
Chapter 2 Adhesion Selectivity by Electrostatic Complementarity: One- Dimensional Stripes of Charge	18
2.1 Introduction.....	19
2.2 Two uniformly charged plates	21
2.2.1 Electric potential between two uniformly charged plates under Debye- Hückel electrostatics.....	22
2.2.2 Force and interaction energy between two uniformly charged plates.....	24
2.3 Interaction between rigid surfaces with striped patterns of charge.....	26
2.3.1 Electrostatics between two rigid surfaces	28
2.3.2 Numerical results and discussion	33

2.4 Interaction between elastic surfaces with striped patterns of charge	35
2.4.1 One-dimensional model of elastically deformable surfaces patterned with stripes of charge.....	36
2.4.2 Model and algorithm	38
2.4.3 Analysis of a simple case, $(m,n)=(1,3)$	44
2.4.4 How deformability affects selectivity	46
2.5 Summary and conclusions	48
2.6 References.....	49
Chapter 3 Adhesion of Micro-channel Based Complementary Surfaces	51
3.1 Introduction.....	52
3.2 Experimental methods	54
3.2.1 Sample fabrication.....	54
3.2.2 Adhesion testing.....	56
3.2.3 Relating crack length to energy release rate.....	59
3.3 Results and discussion	59
3.3.1 Defects accommodate relative shear and rotation between strips	59
3.3.2 Adhesion measurements of complementary interfaces	63
3.3.3 Adhesion measurements of non-complementary interfaces.....	66
3.4 Mechanisms of adhesion modulation for complementary interfaces	69
3.4.1 Crack-trapping.....	69
3.4.2 Effect of friction	73
3.4.3 Energy release by misfit dislocations.....	75
3.5 Summary and discussion.....	83
3.6 References.....	84

Chapter 4 Frictional Auto-Roughening of a Surface with Spatially Varying	
Stiffness	87
4.1 Introduction.....	88
4.2 Experimental methods	89
4.2.1 Sample fabrication.....	89
4.2.2 Friction measurement	93
4.3 Results and discussion	94
4.3.1 Friction test on homogeneous control samples	94
4.3.2 Friction test on samples with 1-D and 2-D periodic variation in properties	96
4.3.3 Friction test under different normal loads	102
4.3.4 Apparent shear stress.....	104
4.4 Mechanism of auto-roughening effect	107
4.5 Summary and conclusion	115
4.6 References.....	116
Chapter 5 Enhancement of Friction against a Rough Surface by a Ridge-	
Channel Surface Microstructure.....	119
5.1 Introduction.....	120
5.2 Experimental methods	122
5.2.1 Sample preparation.....	122
5.2.2 Friction measurement	125
5.3 Results.....	126
5.3.1 Smooth indenter	126
5.3.2 Roughened indenter.....	129
5.3.3 Influence of normal load and geometry	132

5.3.4 Apparent and real shear stress	135
5.4 Discussion and summary	145
5.5 References	145
Chapter 6 Summary & Conclusions	149
6.1 Main results.....	149
6.2 Ongoing and future work	150
6.3 References.....	151
Appendices.....	152
A: Model for electrostatic complementarity	152
B: Surface profilometry of the composite samples.....	161
C: Friction test on backfilled fibrillar samples under large normal load	163
D: Estimating the mean and variance of the apparent shear stress	164
E: Contact pressure on flat homogenous elastomer	165
F: Simple beam model for auto-roughening	166
References.....	170
Vita	171

List of Figures

Figure 1.1	<i>Schematic diagram of surfaces patterned with stripes of charge.</i>	6
Figure 1.2	<i>SEM images of a pair of complementary surfaces with interchannel spacing $c = 35 \mu\text{m}$</i>	7
Figure 1.3	<i>Schematic illustration of the experimental set-up for measuring adhesion energy</i>	8
Figure 1.4	<i>Schematic diagram of the surfaces with 1-D & 2-D periodic variation in stiffness.....</i>	11
Figure 1.5	<i>Schematic drawing of the apparatus used for friction experiments.....</i>	11
Figure 2.1	<i>Schematic diagram of a 1-D model comprising two uniformly charged plates</i>	22
Figure 2.2	<i>Force and interaction energy per unit area between two uniformly charged surfaces as a function of distance between them</i>	26
Figure 2.3	<i>Schematic diagram of surfaces patterned with stripes of charge ($mb=nc$, in this case, $3b=5c$).....</i>	27
Figure 2.4	<i>Equilibrium distance between two charged surfaces as a function of area fraction α of like charges across the gap</i>	31
Figure 2.5	<i>Interaction energy and total force when $mn=3$.....</i>	32
Figure 2.6	<i>Plots of interaction energy between two patterned surfaces for different m and n.....</i>	34
Figure 2.7	<i>Schematic diagram of a 1-D elastic surface with patterned charge (half unit cell: $3b=5c$)</i>	37
Figure 2.8	<i>Illustration of deformation of $(m,n)=(1,3)$ pattern.....</i>	44
Figure 2.9	<i>Middle node displacement (δ) and total energy at equilibrium as a function of stiffness when $L = 1$ (stripe combination $b=3c$)</i>	45
Figure 2.10	<i>Initial and equilibrium nodal positions for a $(3,5)$ surface</i>	47

Figure 3.1	<i>Schematic illustration of the sample fabrication process</i>	<i>55</i>
Figure 3.2	<i>SEM images of a pair of complementary surfaces with interchannel spacing $c = 35 \mu\text{m}$</i>	<i>56</i>
Figure 3.3	<i>(a) Schematic illustration of the experimental set-up for measuring adhesion energy. (b) Photograph of the experimental set-up showing the wire that serves as a wedge opening a crack.....</i>	<i>58</i>
Figure 3.4	<i>Micrographs of defects in micro-channel complementary surfaces</i>	<i>62</i>
Figure 3.5	<i>Optical micrographs of the region behind and ahead of the crack front....</i>	<i>64</i>
Figure 3.6	<i>Normalized energy release rate required to open the interface for different interchannel spacing, and three different channel depths</i>	<i>65</i>
Figure 3.7	<i>Low magnification pictures of complementary samples with channel depth, $d = 30 \mu\text{m}$.....</i>	<i>66</i>
Figure 3.8	<i>(a) Normalized energy release rate versus periodic spacing of the bottom sheet for non-complementary interfaces. (b) shows an optical micrograph for channel width of $30 \mu\text{m}$. (c) shows an optical micrograph with pillar width of $30 \mu\text{m}$.....</i>	<i>68</i>
Figure 3.9	<i>Schematic diagram showing directions of crack propagation along both the flat interface and the structured interface.....</i>	<i>70</i>
Figure 3.10	<i>Finite element model of crack-trapping mechanism for two different channel depths</i>	<i>72</i>
Figure 3.11	<i>Fraction of dislocation area in a series of complementary samples with depth $d = 10 \mu\text{m}$ and variable interchannel spacing, c.....</i>	<i>76</i>
Figure 3.12	<i>Schematic diagram showing how dislocations accommodate shear and rotation</i>	<i>81</i>
Figure 4.1	<i>Schematic diagram of the process that creates surfaces with (a) 1-D and (b) 2-D periodic variation in stiffness.....</i>	<i>90</i>
Figure 4.2	<i>SEM images of different structured composite samples</i>	<i>92</i>
Figure 4.3	<i>Experimental set-up for the friction tests</i>	<i>94</i>

Figure 4.4	<i>Optical micrographs of spherical glass indenter sliding on a flat homogenous control sample</i>	96
Figure 4.5	<i>(a) Shear force as a function of shear displacement for samples with 1-D periodic variation of stiffness and both homogeneous controls; (b) optical micrographs taken during a friction test on a sample with spatially varying stiffness (depth $d = 10 \mu\text{m}$, spacing $c = 35 \mu\text{m}$)</i>	99
Figure 4.6	<i>(a) Shear force as a function of shear displacement for samples with 2-D variation in stiffness and both homogeneous controls; (b) optical micrographs taken during a friction test on composite fibrillar samples (depth $d = 10 \mu\text{m}$, spacing $c = 20 \mu\text{m}$)</i>	101
Figure 4.7	<i>(a) Optical micrographs taken during a friction test on backfilled micro-channel samples ($d = 10 \mu\text{m}$, $c = 20 \mu\text{m}$); (b) Shear force as a function of shear displacement</i>	103
Figure 4.8	<i>(a) Apparent shear stress of composite samples compared to both stiff and compliant flat controls, under the same normal load ($F_N = 3.5 \text{ mN}$). (b) Apparent shear frictional stress for four different normal loads and fixed spacing of $20 \mu\text{m}$</i>	105
Figure 4.9	<i>(a) Schematic of the cross-section of an elastic sample that is infinite in the out-of-plane direction; (b) contact pressure along the interface during normal indentation without shear (end of step one)</i>	108
Figure 4.10	<i>(a) Contact pressure along the interface under combined normal and shear displacement; (b) relative displacement of the surface profile with respect to the indenter; (c) Shear traction distribution along the interface; (d) schematic illustration of the deformed structure during sliding phase</i>	110
Figure 4.11	<i>(a) 3-D surface plots of contact opening percentage. (b) Fraction of lost contact area as a function of normalized displacement</i>	114
Figure 5.1	<i>(a) Schematic illustration of structured elastomeric samples. (b) Scanning electron micrograph of a typical structured surface</i>	123
Figure 5.2	<i>Surface morphology of glass surface on roughened spherical indenter, examined by optical profilometer</i>	125
Figure 5.3	<i>Schematic illustration of the apparatus used for friction tests (side view)</i>	126

Figure 5.4	<i>(a) ~ (e): Optical micrographs of flat control and micro-channel structured samples under shear by a smooth spherical indenter (f) Typical force-displacement response of a smooth spherical indenter</i>	128
Figure 5.5	<i>(a) ~ (d): Optical micrographs of flat control and micro-channel structured samples under shear by the roughened spherical indenter. (f) Typical force-displacement curves of roughened spherical indenter sliding against micro-channel structured surfaces (same depth, different spacing)</i>	131
Figure 5.6	<i>Comparison of sliding friction on micro-channel based samples using smooth (dashed lines) and roughened (solid lines) indenters, normalized by the sliding friction of a flat control sample</i>	135
Figure 5.7	<i>Apparent shear stress (a,c,e) and real shear stress (b,d,f) of micro-channel samples sliding against the roughened indenter, compared to a flat control.....</i>	137
Figure 5.8	<i>Typical contact region between the smooth indenter and micro-channel based surface with spacing, $c = 20 \mu\text{m}$</i>	139
Figure 5.9	<i>Typical contact region between the randomly rough surface and micro-channel based surface with spacing, $c = 20 \mu\text{m}$</i>	141
Figure 5.10	<i>Typical contact region between the smooth indenter and micro-channel based surface with channel depth, $d = 13.0 \mu\text{m}$.....</i>	142
Figure 5.11	<i>Typical contact region between the randomly rough surface and micro-channel based surface with channel depth, $d = 13.0 \mu\text{m}$</i>	143
Figure 5.12	<i>(a) ~ (c): Schematic illustration of contact region between the randomly rough surface and micro-channel based surface with large depth and inter-channel spacing (side view). (d) Optical micrograph of the contacting area under shear</i>	144
Figure A.1	<i>$mn - 12mn$ versus fraction of repulsive part for different m & n combinations.....</i>	159
Figure A.2	<i>The fraction α depends on the shift δ. For $m = 1$ and $n = 1,3,5,\dots$, it is minimized when $\delta = 0$.....</i>	160
Figure A.3	<i>The fraction α depends on the shift δ. For $m > 1$ and $n = 1,3,5,\dots$, it is a periodic function of, δ, with a minimum at $\delta = 0$.....</i>	160

Figure B.1	<i>Typical surface morphology of composite ridge/channel samples.....</i>	161
Figure B.2	<i>Friction measurement on a over-backfilled 1-D micro-channel sample..</i>	162
Figure C.1	<i>Optical micrographs taken during a friction test on backfilled fibrillar samples ($h = 17.8 \mu\text{m}$, $s = 20 \mu\text{m}$)</i>	163
Figure C.2	<i>Shear force as a function of shear displacement for 2-D periodic samples with spacing of 20, 35 and 50 μm and fixed fibril length $h = 17.8 \mu\text{m}$, and both flat control samples</i>	163
Figure E.1	<i>Half-space contact pressure distribution along the interface due to indentation by a flat rigid punch</i>	166
Figure F.1	<i>Schematic illustration of an elastic beam under a uniformly distributed pressure P</i>	167
Figure F.2	<i>Schematic illustration of a beam model for auto-roughening</i>	168

List of Tables

Table 2.1 <i>Examples of arrangements for a given node, i, and definition of terms $sign(opp)$ and $sign(local)$ that determine the change in electrostatic energy per unit movement of node i.</i>	39
Table F.1 <i>Boundary conditions of analytical beam theory model</i>	169

Abstract

Enhanced and selective adhesion, and controlled friction between contact surfaces are highly desirable mechanical properties for high-level functional materials. There are many instances in nature where such properties have been obtained by design of near-surface architecture. Inspired by many highly functional biological systems, we have explored bio-mimetic materials with different surface patterning, with the goal of designing surfaces that have unique combinations of contact mechanical properties. In the studies presented here, we show how: (a) highly selective adhesion can be achieved by complementarity of patterned charge and shape, and (b) how friction can be modulated by spatial variation in stiffness, and how structured surfaces interact with surface roughness.

We consider how adhesion selectivity can be accomplished by complementarity of shape and inter-surface forces. We have studied an example each of charge and shape complementarity for selective adhesion between extended surfaces. First, we studied theoretically how surfaces patterned with stripes of charge interact with each other, and exhibit strong selectivity on rigid surfaces. However, deformability of the surfaces plays a crucial role in modulating adhesion by accommodating mismatches. To achieve shape complementarity, we designed and fabricated patterned elastomeric surfaces with lines of channels and complementary ridges with dimensions at the micrometer scale. We show that such surfaces have highly enhanced effective adhesion for shape complementary

pairs and low adhesion between surfaces with a shape mismatch. We find that the pillar/channel combinations form defects to accommodate interfacial misalignment. These defects are interfacial dislocations. Adhesion between complementary surfaces is enhanced by crack trapping and friction, and attenuated due to the energy released by dislocation structures.

In addition to enhanced adhesion, we studied the deliberate control of friction through near-surface micro-structures. Friction measurements on elastomeric surfaces patterned with periodic variation in stiffness show that it undergoes an “auto-roughening” transition under shear and this process can strongly attenuate overall sliding friction. Friction reduction is due to reduction of real contact area, as the initially full contact breaks up into partial contact at the interface. Finite element analysis demonstrates how auto-roughening depends on the modulus mismatch, frictional stress and normal displacement.

A surface with random roughness is used to study sliding friction against micro-channel structures under fixed normal force. In contrast to a smooth surface, against which structured surfaces all have highly reduced sliding friction, the roughened surface can exhibit significantly larger frictional force on a structured surface. The enhancement of sliding friction is governed by channel depth, spacing and applied normal force.

Chapter 1 Introduction

In nature, highly controllable contact mechanical properties, such as adhesion, friction and compliance have been achieved by many biological attachment structures^{1,2}. These near-surface architectures are widely utilized for animal locomotion, such as in insects, spiders and lizards³⁻⁷. One well-known example is the features on the toe-pad of the gecko, a hierarchical fibrillar design. It enables a relatively heavy living creature to run, climb and traverse walls and ceilings⁸⁻¹⁰. Recent biological studies of such reversible dry adhesion and locomotion have sparked considerable interest both in studying the mechanisms involved and in developing functional bio-mimetic and bio-inspired materials¹¹⁻¹⁷.

Inspired by the adhesive structures on the gecko toepads, many mimetic materials have been designed, fabricated and modeled. They are based on a fibrillar motif, including designs such as spatulated fibrils¹⁸, mushroom-shaped structures¹⁹ and arrays of micro-fibrils with a thin film on top^{20,21}. Other synthetic surface designs for modification of contact mechanical properties include a flat elastomeric surface with embedded air- or oil-filled microchannels^{22,23}, shallow “chocolate”^{24,25}, “pancake” structures²⁶ and wrinkled surfaces²⁷⁻³⁰, etc. Most of these structures are fabricated to have periodic spatial variation in properties.

Selectivity of adhesion is a common feature in biology and is also a highly desirable property. Achieving it usually requires complementarity of some sort between

surfaces. The majority of the work just cited on bio-inspired attachment systems has been on one-sided surface structures, intended to modulate properties against any other generic surface. However, there are plenty of common “perfectly matched” surfaces in nature ³¹⁻
³⁴ that provide inspiration for selectivity in adhesion over an extended surface. Here, we have investigated two types of complementary interfaces, one based on patterned charges and the other on surface topography.

Friction is another important surface mechanical property. A growing emphasis has been placed in topographical surfaces, for controlling interfacial friction behavior ^{35,36}. Here, two questions have been asked related to the study of sliding friction of elastomers: What is the influence on sliding friction of periodic variation in stiffness? Can structured surfaces interact with surface roughness in a synergistic fashion to enhance friction?

1.1 Adhesion selectivity by complementarity

The study of selective adhesion via complementarity involves well-distinguished and opposite properties that undergo strong attraction between the matching pairs. In nature, various types of complementarity have been observed, such as charge ³⁷, shape ³⁸, hydrogen-bond ³⁹ and hydrophobicity ⁴⁰.

Although it is noticed that the interfacial properties can be highly enhanced between complementary surfaces, a deliberate control of adhesion selectivity by complementarity has not been much studied yet. In this thesis, two aspects of surface complementarity have been investigated for enhanced adhesion and selectivity: (1) Theoretical study of adhesion between two flat surfaces patterned with stripes of surface

charge; (2) Experimental work on elastomeric surfaces patterned with an array of ridges and channels.

1.1.1 Electrostatic complementarity

Previously, electrostatic complementarity has been found to play important roles in ligand binding systems and help to make hydrogen bonds with enzymes³⁷. A substrate can always find its favorable active sites of the synthesize enzyme, driven by charge complementarity. Moreover, the complementary aspect of charge is reported to have great potential for the study of chemical bonds⁴¹. However, we notice that most of the studies about electrostatic complementarity are related to biological systems³²⁻³⁴ and molecular interactions. In this thesis, we try to develop a generic method for designing in adhesion selectivity by charge complementarity.

As a model for surfaces with charge complementarity, we consider two surfaces, each with striped patterns of alternating positive and negative surface charge, and each with zero net charge (Figure 1.1). In one-dimension, the interaction between these two pattern-charged plates is governed by Debye–Hückel equation^{42,43}. In addition to the rigid surfaces, we also consider the material on either side to be deformable, modeled by hyperelastic neo-Hookean materials^{44,45}.

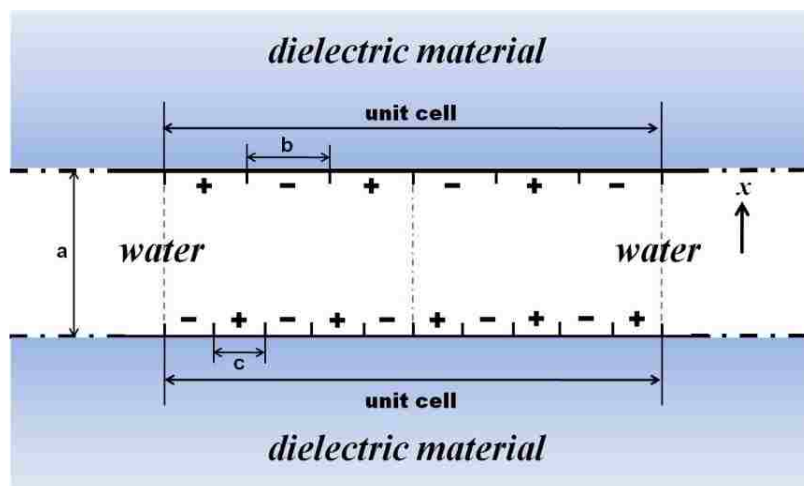


Figure 1.1 Schematic diagram of surfaces patterned with stripes of charge ($mb=nc$, in this case, $3b=5c$). Two infinitely large surfaces with striped patterns of alternating positive and negative charges on a dielectric material face each other in aqueous medium.⁴⁶

1.1.2 Shape complementarity

Barnes⁴⁷ points out that mechanical interlocking is the first main mechanism which enables animals to stick on substrates and oppose gravity, out of the other three (friction, bonding and gluing). The interlocking mechanism is found to be responsible in many biological attachment devices, such as in dragonfly head-arresting system⁴⁸ and beetles' wing-locking systems⁴⁹. Such interlocking system can be viewed as an example in application of shape complementarity in nature. Another celebrated example of the mechanical complementarity is the development of hook-loop fasteners, such as the Velcro® adhesive⁵⁰.

Enhanced adhesion also exhibits between complementary surface structures^{51,52}. Vajpayee *et al*⁵³ has shown that highly selective adhesion can be achieved between complementary elastic surfaces patterned with ripples. Complementary surfaces show an

enhanced interfacial adhesion with increasing ripple amplitude. In contrast, interfaces with mismatched amplitudes had nearly negligible adhesion.

We investigated a related shape-complementary structure, one in which the surface is patterned with a parallel array of ridges and channels with varying channel depths and inter-channel spacing (Figure 1.2). We found a much larger enhancement of adhesion between complementary micro-channel/ridge combinations, with relative misalignment being accommodated by dislocation-defects in the form of visible striations. The first set of elastomeric sample by molding and curing an elastomer, poly (dimethylsiloxane) (PDMS), into etched silicon masters with parallel micro-channel structures patterned by photolithography. Samples with a complementary surface profile were obtained by a second molding and curing step on this first set of PDMS samples. The fabrication technique of the samples is discussed later in Chapter 3.

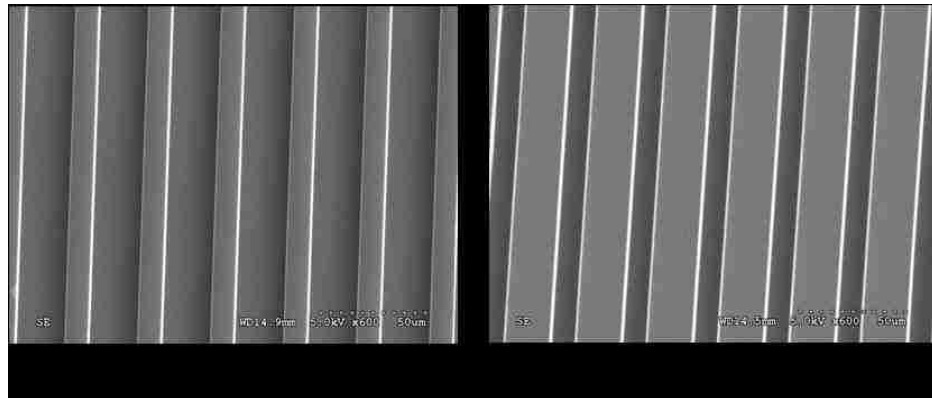


Figure 1.2 SEM images of a pair of complementary surfaces with interchannel spacing $c = 35 \mu\text{m}$. (a) pillar-side with pillar width of $10 \mu\text{m}$, (b) channel side with channel width of $10 \mu\text{m}$.

The performance of micro-channel samples are measured through wedge tests. A wire serves as a wedge, applying an opening displacement approximately equal to its diameter. As a result a crack propagates away from the wire (Figure 1.3). The effective adhesion (energy release rate) at the structured interface can be calculated from measurement of equilibrium crack length.

In Chapter 3, we report that a sizable increase in adhesion can be achieved, over the flat control in these complementary structures. We also show that this enhancement is due to a combination of frictional losses and crack-trapping⁵⁴.

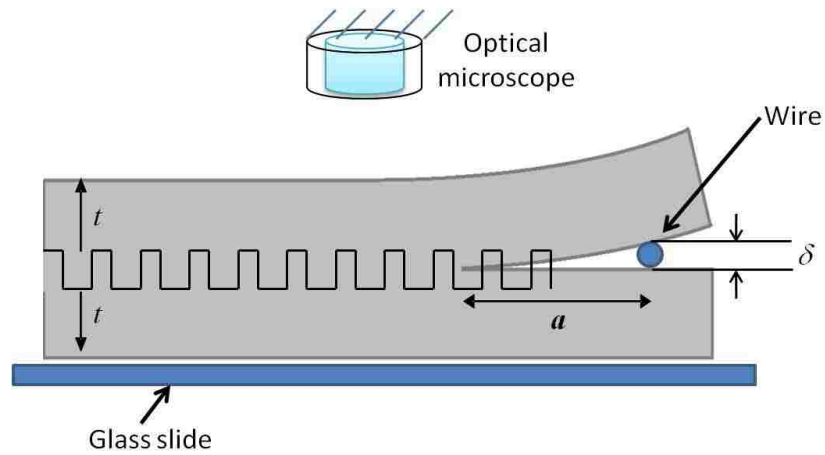


Figure 1.3 Schematic illustration of the experimental set-up for measuring adhesion energy.

1.2 Controlled sliding friction

The study of frictional behavior can be traced back to over 300 years ago, when the model for friction between non-adhering surfaces was first published by Amontons⁵⁵. The Amontons' laws state that the frictional force is proportional to the normal load and independent of apparent contact area⁵⁶. The clear distinction between static and dynamic friction is made in Coulomb's friction law⁵⁵, which states that a static frictional force should be exceeded to initiate sliding, and a smaller dynamic friction is needed to maintain sliding. It is also pointed out that the dynamic friction is independent of sliding velocity. However, the classic Amontons-Coulomb Law fails to explain many aspects of friction, especially for soft materials in contact with rigid surfaces. For example, Chateauminois et al^{57,58} studied the shear stress between a glass lens on a flat PDMS rubber, they found that the friction stress is nearly constant and independent of the sliding rate and distance. Many experiments also show that a hard indenter does not slide uniformly on a soft substrate^{59,60}, formation of Schallamach waves is usually observed during sliding, which is possibly due to surface instabilities such as the buckling effect⁶¹.

Although the frictional behavior of soft materials has not been completely understood, many related investigations have been actively pursued for over half a century⁶², due to its great practical importance in many applications, such as tires, rubber seals and belts, etc. In order to achieve a deliberate control of friction on elastic materials, a number of researchers have shown their interests in modification of frictional property by near-surface architecture, especially the bio-mimetic fibrillar structures^{35,63,64}. Gorb and Varenberg⁶⁵ showed that fibrillar surfaces can exhibit smooth and stable sliding with

much lower friction force, compared to a flat control sample. Additionally, film-terminated fibrillar surfaces who significantly increase in static friction, but little change in the sliding friction compared to a flat control ^{60,66}. Highly reduced sliding friction can also be observed over other type of surface structures, e.g. the wrinkled surfaces ⁶⁷. In this thesis, we have studied the control of friction by samples with spatial variation in stiffness (which are fabricated from both 1-D micro-channel and 2-D fibrillar structured surfaces), and interaction of surface roughness with a structured surface.

1.2.1 Friction on surface with spatial variation in property

Although we have shown that many bio-inspired surface structures are design for modifying the interfacial mechanical properties. Only a few experiments have been carried out for studying surfaces with spatially varying properties. Ghatak and co-workers have reported strong enhancement of adhesion with sub-surface micro-structures filled with fluids (e.g. oil or air) ^{22,23}. The control of adhesion was investigated by Kendall using a composite material with periodic variation in stiffness ⁶⁸.

In Chapter 4, we consider an elastomer with a flat surface but periodic variation in stiffness. We begin with an elastomer having a patterned surface. In a subsequent step, the patterned surface is filled with a second elastomer with different elastic modulus. Two backfilling techniques are applied to fill the gaps in the structured surfaces (Figure 1.4). Friction is measured by shearing the sample relative to an indenter placed on it under controlled normal load ⁶⁶ (Figure 1.5). Experiments show a strong reduction in friction during sliding occurs due to an “auto-roughening” phenomenon in which a fully

connected contact region breaks into partial contact. This thesis also presents a finite element model to show how the auto-roughening depends on the contact openings of interfacial structures, resulting in reduced overall friction.

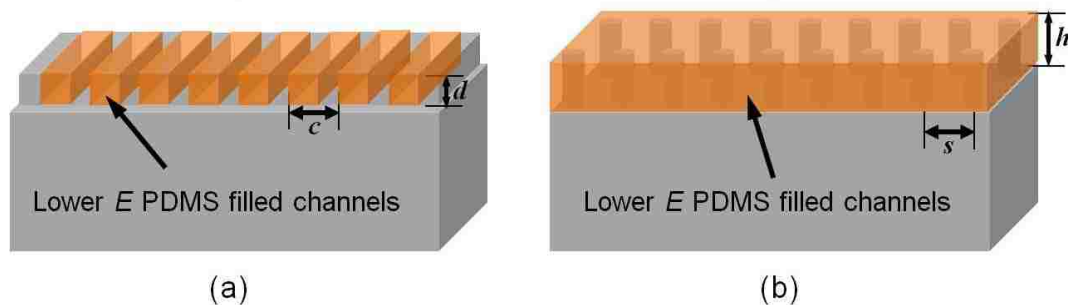


Figure 1.4 Schematic diagram of the surfaces with 1-D & 2-D periodic variation in stiffness.

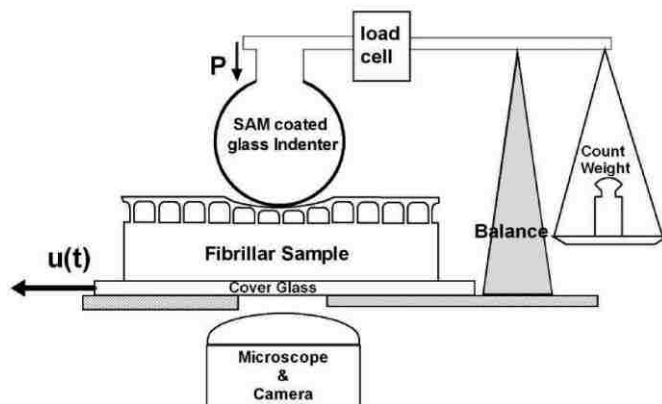


Figure 1.5 Schematic drawing of the apparatus used for friction experiments ^{66, a}.

1.2.2 How roughness affects friction on a structured surface

Much of the work on friction of structured surfaces has been conducted against smooth surfaces. However surface roughness is ubiquitous and has an enormous

^a Reprinted with permission from: Vajpayee, S.; Long, R.; Shen, L.; Jagota, A.; Hui, C-Y. *Langmuir* 2009, 25, 2765-2771. Copyright 2009 American Chemical Society.

influence on contact mechanical properties, including both adhesion and friction. The area of intimate contact is extremely smaller between rough surfaces than their apparent contact area ⁶⁹⁻⁷¹, however rises linearly with the applied normal load ⁷². Theoretical study of contact mechanics between surface roughness and elastomeric materials has been pursued by many researchers, such as Persson ^{73,74}, Johnson ⁷⁵, Hui ^{76,77} and Robbins ^{72,78}. Experimentally, Fuller and Tabor ⁷⁹ found that even a small surface roughness with a few microns in amplitude can remove the adhesion completely between a smooth elastic surface and rigid roughness. Guduru has observed an adhesion enhancement between a wavy punch on a soft gel by testing the pull-off force ⁸⁰, he showed that if there is an initial complete contact, the surface separation is alternately stable and unstable, which leads to an increased effective adhesion ⁸¹.

Interfacial fibrillar structures have also been considered to be a good textured substrate for controlling sliding friction against surface roughness. In theoretical perspective, the interaction between near-surface architecture and roughness was first discussed by Persson ^{82,83}. But not much experimental work has been carried out on this aspect of structured interfaces. Vajpayee *et al* ⁸⁴ showed that a film-terminated fibrillar interface exhibits a reduction in adhesion against rough surfaces, however retains considerable adhesion compared to that of flat surfaces.

In Chapter 5, we studied the sliding friction between a roughened indenter and elastomeric surface patterned with ridges and channels. The sliding friction is measured on series of micro-channel structured samples, with varied channel depth, inter-

channel spacing and applied normal load. We show that the certain structured surfaces have significantly higher friction against a rough surface compared to a flat control.

1.3 Outline

The outline of the remainder of this thesis is presented below:

- Chapter 2 presents a theoretical study of enhanced and selective adhesion between surfaces patterned with stripes of charge.
- Chapter 3 studies the effect of adhesion and selectivity between surfaces patterned with complementary ridge-channel structures, and their underlying mechanism.
- Chapter 4 demonstrates that the friction of a nominally flat surface with spatial variation in stiffness is much reduced compared to a homogeneous control because of an auto-roughening transition.
- Chapter 5 explores friction between random roughness and micro-channel structured surfaces.
- Chapter 6 concludes the thesis with major findings, ongoing work and future work.

1.4 References

- [1] Scherge, M.; Gorb, S. N. *Biological Micro- and Nano-Tribology, Nature's Solutions*; Springer Verlag: Berlin, 2001.
- [2] Arzt, E.; Gorb, S.; Spolenak, R. *Proc. Natl. Acad. Sci.* **2003**, *100*, 10603-10606.
- [3] Eisner T.; Aneshansley, D. J. *Proc. Natl. Acad. Sci.* **2000**, *97*, 6568-6573.
- [4] Stork, N. E. *J. Exp. Biol.* **1980**, *88*, 91-107.

- [5] Kesel, A.B.; Martin, A.; Seidl, T. *J. Exp. Biol.* **2003**, *206*, 2733-2738.
- [6] Russell, A. P. *Integr. Comp. Biol.* **2002**, *42*, 1154-1163.
- [7] Autumn, K. *Am. Sci.* **2006**, *94*, 124.
- [8] Autumn, K.; Liang, Y. A.; Hsieh, S. T.; Zesch, W.; Wai, P. C.; Kenny, T. W. ; Fearing, R.S.; Full, R. J. *Nature* **2000**, *405*, 681-685.
- [9] Autumn, K.; Peattie, A. M. *Integr. Comp. Biol.* **2002**, *42*, 1081-1090.
- [10] Autumn, K.; Sitti, M.; Liang, Y. A.; Peattie, A. M.; Hansen, W. R.; Sponberg, S.; Kenny, T. W.; Fearing, R. S.; Israelachvili J. N.; Full, R. J. *Proc. Natl Acad. Sci.* **2002**, *99*, 12252-12256.
- [11] Jagota, A.; Hui, C-Y. *Materials Science and Engineering R* **2011**, *72*, 253-292.
- [12] Kamperman, M.; Kroner, E.; del Campo, A.; McMeeking R.M.; Arzt, E. *Adv. Eng. Mater.* **2010**, *12*, 335-348.
- [13] Boesel, L.F.; Greiner, C.; Arzt, E.; del Campo A. *Adv. Mater.* **2010**, *22*, 2125-2137.
- [14] Reddy, S.; Arzt E.; del Campo A. *Adv. Mater.* **2007**, *19*, 3833-3837.
- [15] Jagota, A.; Hui, C-Y.; Glassmaker, N. J.; Tang, T. *MRS Bull.* **2007**, *32*, 492.
- [16] del Campo, A.; Greiner C.; Arzt, E. *Langmuir* **2007**, *23*, 10235-10243.
- [17] A. Majumder, A. Sharma and A. Ghatak, *Bio-Inspired Adhesion and Adhesives: Controlling Adhesion by Micro-nano Structuring of Soft Surfaces in Microfluids and Microfabrication*, 2010, Springer, USA.
- [18] Kim, S.; Sitti, M. *Appl. Phys. Lett.* **2006**, *89*, 261911-261913.
- [19] Gorb, S.; Varenberg, M.; Peressadko, A.; Tuma, J. *J. R. Soc. Interface* **2007**, *4*, 271-275.
- [20] Glassmaker, N.J.; Jagota, A.; Hui, C-Y.; Noderer, W.L.; Chaudhury, M.K. *Proc Natl. Acad. Sci.* **2007**, *104*, 10786-10791.
- [21] Noderer, W. L.; Shen, L.; Vajpayee, S.; Glassmaker, N.J.; Jagota, A.; Hui, C-Y. *Proc. R. Soc. A* **2007**, *463*, 2631-2654.
- [22] Majumder, A.; Ghatak A.; Sharma, A. *Science* **2007**, *318*, 258-261.
- [23] Ghatak, A. *Phys. Rev. E* **2010**, *81*, 021603.
- [24] Chung, J.Y.; Chaudhury, M.K. *J. R. Soc. Interface* **2005**, *2*, 55-61.

- [25] Ghatak, A.; Mahadevan, L.; Chung, J.Y.; Chaudhury, M.K.; Shenoy, V. *Proc. Roy. Soc. Lond. Ser. A* **2004**, *460*, 2725-2735.
- [26] Crosby, A.; Hageman, M.; Duncan, A. *Langmuir* **2005**, *21*, 11738-11743.
- [27] Chan, E. P.; Crosby, A. J. *Adv. Mater.* **2006**, *18*, 3238-3242.
- [28] Bowden, N.; Brittain, S.; Evans, A. G.; Hutchinson, J. W.; Whitesides, G. M. *Nature* **1998**, *393*, 146-149.
- [29] Chung, J. Y.; Nolte, A. J.; Stafford, C. M. *Adv. Mater.* **2011**, *23*, 349-368.
- [30] Lin, P. C.; Vajpayee, S.; Jagota, A.; Hui, C.-Y.; Yang, S. *Soft Matter* **2008**, *4*, 1830-1835.
- [31] Alberts, B.; Johnson, A.; Lewis, J.; Raff, M.; Roberts, K.; Walter, P. *Molecular Biology of the Cell* 5th edition, Garland Science, Taylor & Francis Group: New York, 2008.
- [32] McCoy, A.; Chandana Epa, V.; Colman, P. *J. Mol. Biol.* **1997**, *268*, 570.
- [33] Weiner, P.; Langridge, R.; Blaney, J.; Schaefer, R.; Kollman, P. *Proc. Natl. Acad. Sci.* **1982**, *79*, 3754.
- [34] Náráy-Szabó, G. *J. Mol. Graphics* **1989**, *7*, 76.
- [35] Majidi, C.; Groff, R. E.; Maeno, Y.; Schubert, B.; Baek, S.; Bush, B.; Maboudian, R.; Gravish, N.; Wilkinson, M.; Autumn K.; Fearing, R.S. *Phys. Rev. Lett.* **2006**, *97*, 076103-076107.
- [36] Kim, S.; Aksak B.; Sitti, M. *Appl. Phys. Lett.* **2007**, *91*, 221913.
- [37] Kangas, E.; Tidor, B. *J. Phys. Chem. B* **2001**, *105*, 880-888.
- [38] Bowden, N.; Terfort, A.; Carbeck, J.; Whitesides, G. M. *Science* **1997**, *276*, 233-235.
- [39] Mbindyo, J. K.; Reiss, B. D.; Martin, B. R.; Keating, C. D.; Natan, M. J.; Mallouk, T. E. *Adv. Mater.* **2001**, *13*, 249-254.
- [40] Chothia, C.; Janin, J. *Nature* **1975**, *256*, 705-708.
- [41] Becker, P. J.; Gillet, J. M.; Cortona, P.; Ragot, S. *Theor. Chem. Acc.* **2001**, *105*, 284-291.
- [42] Schlick, T. *Molecular Modeling and Simulation, An Interdisciplinary Guide*, Springer: New York, 2002.

- [43] Russel, W.B.; Saville, D. A.; Schowalter, W.R. *Colloidal Dispersions*, Cambridge University Press, 1989.
- [44] Ogden, R. *Non-linear Elastic Deformations*, Dover: New York 1984.
- [45] Yeoh, O.H. *Rubber Chem. Technol.* **1993**, *66*, 754.
- [46] Bai, Y.; Jin, C.; Jagota, A.; Hui, C.-Y. *J. Appl. Phys.* **2011**, *110*, 054902.
- [47] Barnes, W. Jon. P., *MRS Bull.* **2007**, *32*, 479-485.
- [48] Gorb, S. N. *Proc. R. Soc. Lond. B: Biol. Sci.* **1999**, *266*, 525-535.
- [49] Gorb, S. N. *et al. Integr. Comp. Biol.* **2002**, *42*, 1127-1139.
- [50] de Mestral, G. *U.S. patent 2,717,437*, 1955.
- [51] Lamblet, M.; Verneuil, E. ; Vilmin, T.; Buguin, A.; Silberzan, P.; Leger L. *Langmuir* **2007**, *23*, 6966-6974.
- [52] Shahsavan, H.; Zhao, B. *Langmuir* **2011**, *27*, 7732-7742.
- [53] Vajpayee, S.; Khare, K.; Yang, S.; Hui, C-Y.; Jagota, A. *Adv. Func. Mater.* **2011**, *21*, 547-555.
- [54] Singh, A.K.; Bai, Y.; Nadermann, N; Jagota, A; Hui, C-Y. *Langmuir* **2012**, *28*, 4213-4222.
- [55] Dowson, D. *History of Tribology* Longman: New York, 1979.
- [56] Amontons, G. *Memoires de l'Academie Royale A* 1699, 257-282.
- [57] Chateauminois, A.; Fretigny, C.; Olanier, L. *Phys. Rev. E* **2010**, *81*, 026106.
- [58] Chateauminois A. ; Fretigny, C. *Eur. Phys. J. E* **2008**, *27*, 221-227.
- [59] Rand, C. J.; Crosby, A. J. *Apply. Phys. Lett.* 2007, *91*, 261909.
- [60] Shen, L.; Jagota A.; Hui, C-Y. *Langmuir* **2009**, *25*, 2772-2780.
- [61] Schallamach, A. *Wear* **1971**, *17*, 301-312.
- [62] Sills, S.; Vorvolakos, K.; Chaudhury, M.; Overney, R; *Molecular origins of elastomeric friction*. In E. Gnecco, E. Meyer (eds.) *Nanotribology: Friction and Wear on the Atomic Scale*. Springer: Berlin, 2007.
- [63] Aksak, B.; Sitti, M.; Cassell, A.; Li, J.; Meyyappan, M.; Callen, P. *Appl. Phys. Lett.* **2007**, *91*, 061906.
- [64] Tian, Y.; Pesika, N.; Zeng, H.; Rosenberg, K.; Zhao, B.; McGuiggan, P.; Autumn, K.; Israelachvili, J. *Proc. Nat. Acad. Sci.* **2006**, *103*, 19320-19325.

- [65] Varenberg M.; Gorb, S. *J. R. Soc. Interface* **2007**, *4*, 721-725.
- [66] Vajpayee, S.; Long, R.; Shen, L.; Jagota A.; Hui, C-Y. *Langmuir* **2009**, *25*, 2765-2771.
- [67] Rand C.; Crosby, A. *J. Appl. Phys.* **2009**, *106*, 064913.
- [68] Kendall, K. *Proc. R. Soc. London A: Math. Phys. Sci.* **1975**, *341*, 409-428.
- [69] Bowden, F. P.; Tabor, D. *Friction and Lubrication* Wiley: New York, 1956.
- [70] Persson, B. N. J. *J. Chem. Phys.* **2001**, *115*, 3840.
- [71] Hyun, S.; Pei, L.; Molinari, J.-F.; Robbins, M. O. *Phys. Rev. E* **2004**, *70*, 026117.
- [72] Akarapu, S.; Sharp T.; Robbins, M. O. *Phys. Rev. Lett.* **2011**, *106*, 204301.
- [73] Persson, B. N. J. *Surf. Sci. Rep.* **2006**, *61*, 201.
- [74] Persson, B. N. J. *Phys. Rev. Lett.* **2001**, *87*, 116101.
- [75] Johnson, K. L. *Int. J. Solids Struct.* **1995**, *32*, 423-430.
- [76] Hui, C.-Y.; Lin, Y. Y.; Baney J. M.; Kramer, E. J. *J. Polym. Sci. B. Polym. Phys.* **2001**, *39*, 1196-1214.
- [77] Hui, C.-Y.; Lin Y. Y.; Creton, C. *J. Polym.Sci. Part B. Polym. Phys.* **2002**, *40*, 545-561.
- [78] Pastewka, L.; Prodanov, N.; Lorenz, B.; Müser, M. H.; Robbins, M. O.; Persson, B. N. J. *Phys. Rev. E* **2013**, *87*, 062809.
- [79] Fuller K. N. G.; Tabor, D. *Proc. Roy. Soc. London A* **1975**, *345*, 327-342.
- [80] Guduru P. R.; Bull, C. *J. Mech. Phys. Solids* **2007**, *55*, 473-488.
- [81] Guduru, P. R. *J. Mech. Phys. Solids* **2007**, *55*, 445-472.
- [82] Persson B. N. J.; Gorb, S. *J. Chem. Phys.* **2003**, *119*, 11437-11444.
- [83] Persson, B. N. J. *MRS Bull.* **2007**, *32*, 486-490.
- [84] Vajpayee, S.; Jagota A.; Hui, C-Y. *J. Adh* **2010**, *86*, 39-61.

Chapter 2 Adhesion Selectivity by Electrostatic Complementarity: One- Dimensional Stripes of Charge^b

Highly enhanced and selective adhesion can be achieved between surfaces patterned with charges even when each one has no net charge. In this chapter, we analyze the possibility of adhesion selectivity between two flat surfaces patterned with stripes of surface charge chosen such that each surface initially carries no net charge. A few combinations, with appropriately matching strip widths, are predicted to adhere to each other. We also find that the deformability of the materials plays a critical role in defining the range of patterns that recognize each other, i.e., their selectivity. With increasing compliance, a significant enhancement of adhesion can be achieved by deformation that allows better matching between charge patterns.

^b Reprinted with permission from: Bai, Y.; Jin, C.; Jagota, A.; Hui, C-Y. "Adhesion selectivity by electrostatic complementarity. I. One-dimensional stripes of charge." *Journal of Applied Physics* 110, 5 (2011): 054902. Copyright 2011, AIP Publishing LLC.

2.1 Introduction

Enhanced, selective, and controllable adhesion between surfaces is a highly desired property. At the macroscopic scale it manifests in a variety of fastening devices and designs based on shape complementarity. As the property of a material surface, it can endow the ability to reject any surface other than its complementary one. That is, adhesive and friction energy can be large between two complementary surfaces, and highly attenuated when they are not matched. Selectivity usually requires complementarity of some sort between surfaces. In nature, this idea of selectivity extends all the way from the organism to individual molecules. For example, several interlocking mesoscale structures are responsible for attachment of forewings to the thorax in beetles (Coleoptera)¹, as well as in the dragonfly head-arresting system². At the much smaller length scale of intermolecular interactions, one finds complementarity leading to recognition due to shape, charge, and hydrogen-bonding. For example, it is well known that molecular shape plays an important role in the recognition and binding of biological molecules³. Over the years, shape complementarity has been confirmed by inspection of a large number of complex structures in the protein data bank (PDB, Bernstein et al.⁴). However, it has been demonstrated that antibody/ antigen interfaces have a poorer geometric match than other protein/protein interfaces. Usually, specificity of interactions between antigen and antibody also involve non-covalent binding of an antigenic determinant to the variable region (complementarity determining region, CDR). Thus specificity arises due to a combination of complementarity in shapes, hydrophobic interactions, hydrogen bonds and Van der Waals forces⁵⁻⁷. In nature, biochemistry

demonstrates that intermolecular attraction between complementary surfaces can assemble complex structures from solution. For example, the complex machinery of the ribosome self-assembles from more than 50 different protein molecules and can do so *in vitro*^{8,9}.

The deliberate control of adhesion selectivity of material surfaces by complementarity has not been much studied. Examples include the celebrated case of loop-clasp designs that led to the development of Velcro®¹⁰. In other examples, selectivity in adhesion has been accomplished by design of surface chemistry¹¹⁻¹⁴, using fibrillar structures¹⁵, or between two complementary rippled surfaces¹⁶. A study about surface pattern recognition by using hydrophobic complementarity was reported by E. Kokkoli and C.F. Zukoski¹⁷.

Electrostatic complementarity presents a promising approach. In this work we ask: Is it possible to achieve high selectivity, as measured via adhesion, using relatively smooth and flat extended surfaces patterned with charges? Although a number of measurements and explanations for electrostatic complementarity have been developed for biological systems¹⁸⁻²⁰, its use as a generic method for designing in selectivity has not been studied. We consider the interaction between two flat surfaces separated by water, with simple striped patterns of alternating positive and negative surface charges, summing to zero net charge on either one. We predict that such surfaces will have highly selective adhesion depending on the matching between charge patterns on the two surfaces. This selectivity is modulated strongly by deformability of the materials.

2.2 Two uniformly charged plates

We imagine an experimental realization in which the surfaces of two flat dielectric solids are patterned by self-assembled monolayers with surface groups that protonate or de-protonate in aqueous medium (e.g., NH^2 to NH^{3+} or COOH to COO^-), creating stripes of surface charges. The interaction between these charges is modeled by the Debye–Hückel equation ²¹, which is a linearized form of the Poisson-Boltzmann equation ²²⁻²⁵ and is strictly valid for low ionic concentrations and potential.

Anticipating that often the gap between surfaces will be much smaller than the lateral length scale of charge patterns, we expect to be able to represent the total interaction by a sum of local interactions between two uniformly charged infinite plates in water in the presence of ions. (We have also analyzed ³⁰ the full two-dimensional potential field.) The two plates can have different charge densities (σ_1 and σ_2), but the charge distribution on each plate is uniform. They are placed parallel to each other at a distance of “ a ”, as shown in Figure 2.1. We begin by establishing the force and energy of interaction between two such surfaces.

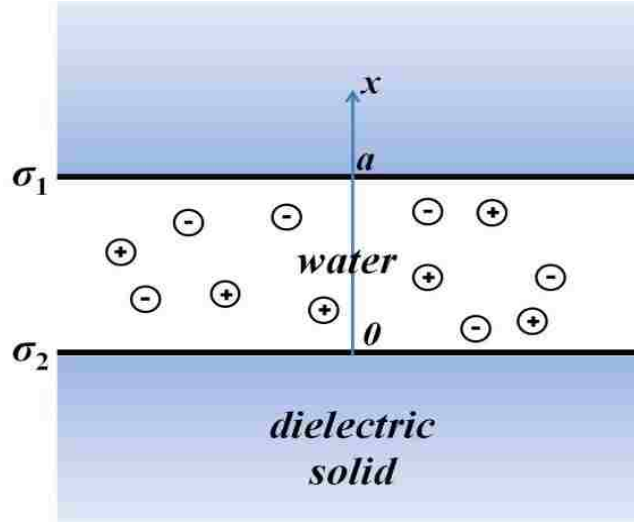


Figure 2.1 Schematic diagram of a 1-D model comprising two uniformly charged plates, with different charge densities (σ_1 and σ_2) separated by a distance, a .

2.2.1 Electric potential between two uniformly charged plates under Debye-Hückel electrostatics

In one-dimension, the variation in electrostatic potential in the region between the two plates is governed by the Debye–Hückel equation.^{24, 25}

$$\frac{d^2\varphi}{dx^2} = \frac{\varphi}{l_D^2} \quad (2.1)$$

where l_D is the Debye screening length²⁵ that, for a z - z electrolyte (e.g., 1-1 for NaCl) is

$$l_D = \sqrt{\frac{\epsilon\epsilon_0 k_B T}{2q^2 z^2 c_0}} \quad (2.1a)$$

where ϵ is the dielectric constant of water, ϵ_0 is the permittivity of free space, q is the charge of an electron, z is the unsigned valence of each of the two ions, c_0 is the concentration of the ions, T is temperature, and k_B is Boltzmann's constant.

The potential at either interface decays on the dielectric side over a length approximately equal to the sample thickness. On the water side it decays over the Debye screening length. Because the sample thickness (\sim mm) is much larger than the Debye screening length (\sim nm), the dielectric can be modeled as a conductor (constant potential) in comparison with the strongly decaying field on the water side ^c. As a result, the boundary conditions at the two interfaces that relate the field to surface charge density take the form

$$\begin{aligned} \text{a.} \quad & -\epsilon\epsilon_0 \frac{d\varphi}{dx} = \sigma_1 & (x=0), \\ \text{b.} \quad & \epsilon\epsilon_0 \frac{d\varphi}{dx} = \sigma_2 & (x=a). \end{aligned} \tag{2.1b}$$

The general solution of Eq. (2.1) is:

$$\varphi(x) = A \cosh\left(\frac{x}{l_D}\right) + B \sinh\left(\frac{x}{l_D}\right) \tag{2.2}$$

and

$$\frac{d\varphi}{dx} = \frac{A}{l_D} \sinh\left(\frac{x}{l_D}\right) + \frac{B}{l_D} \cosh\left(\frac{x}{l_D}\right) \tag{2.3}$$

Applying the boundary conditions, we find:

$$\varphi(x) = \frac{[\sigma_1 \cosh\left(\frac{a}{l_D}\right) + \sigma_2] l_D}{\epsilon\epsilon_0} \frac{\cosh\left(\frac{x}{l_D}\right)}{\sinh\left(\frac{a}{l_D}\right)} - \frac{\sigma_1 l_D}{\epsilon\epsilon_0} \sinh\left(\frac{x}{l_D}\right) \tag{2.4}$$

When the two plates have the same charge density, σ , the result is:

^c We have separately analyzed the electric potential distribution in an infinite open system with five regions: a narrow gap between the two charged plates, the plates themselves, and the exterior region on either side of the plates (results available from authors). We find that, under the conditions of interest to us, i.e., when the gap is on the order of Debye screening length (a few nm), the field inside the charged plates is negligible. The solution is then nearly identical to that of a single domain between the two charged plates with a jump in the electric field balanced by the charge density on the two surfaces.

$$\varphi(x) = \frac{\sigma l_D}{\epsilon \epsilon_0} \frac{\cosh(\frac{a/2-x}{l_D})}{\sinh(\frac{a/2}{l_D})} \quad (2.5)$$

Note that, as expected, this function is even about $x = a/2$. When both surfaces have the same magnitude of charge density, but of opposite sign ($\sigma_2 = \sigma; \sigma_1 = -\sigma$), then the electric potential is:

$$\varphi(x) = \frac{\sigma l_D}{\epsilon \epsilon_0} \frac{\sinh(\frac{a/2-x}{l_D})}{\cosh(\frac{a/2}{l_D})} \quad (2.6)$$

As expected, this function is odd about $x = a/2$.

2.2.2 Force and interaction energy between two uniformly charged plates

Using the Maxwell stress ²⁶, the force, f , (per unit area) ^d on the plate at $x = a$ can be expressed by:

$$f = -\frac{\epsilon \epsilon_0}{2} \left(\frac{d\varphi}{dx}\right)^2 + \frac{\epsilon \epsilon_0}{2} \frac{\varphi^2}{l_D^2} \quad (2.7)$$

which can be evaluated at any point $0 \leq x \leq a$. Introduce the normalization

$$\hat{\varphi} = \frac{\epsilon \epsilon_0 \varphi}{\sigma l_D}, \quad \hat{x} = \frac{x}{l_D}, \quad \hat{a} = \frac{a}{l_D}, \quad \frac{d\hat{\varphi}}{d\hat{x}} = \frac{\epsilon \epsilon_0}{\sigma} \frac{d\varphi}{dx}, \quad \hat{f} = \frac{\epsilon \epsilon_0 f}{\sigma^2}, \quad \hat{E} = \frac{\epsilon \epsilon_0 E}{\sigma^2 l_D} \quad (2.8)$$

where E is the interaction energy per unit area. The potential between plates with the same charge density, Eq. (2.5), becomes

$$\hat{\varphi}(\hat{x}) = \frac{\cosh(\hat{a}/2 - \hat{x})}{\sinh(\hat{a}/2)} \quad (2.5a)$$

the potential between plates with equal and opposite charge density, Eq. (2.6), becomes

$$\hat{\varphi}(\hat{x}) = \frac{\sinh(\hat{a}/2 - \hat{x})}{\cosh(\hat{a}/2)} \quad (2.6a)$$

^d Here we assume that each surface has a unit thickness out of plane.

and the force per unit area, Eq.(2.7), becomes

$$\hat{f} = \frac{\hat{\varphi}^2}{2} - \frac{1}{2} \left(\frac{d\hat{\varphi}}{d\hat{x}} \right)^2 \quad (2.9)$$

For plates with equal charge densities, we use Eq. (2.5a) in Eq. (2.9), evaluated at $\hat{x} = \hat{a}/2$, where, by symmetry, $\frac{d\hat{\varphi}}{d\hat{x}} = 0$. Then,

$$\hat{f}_R = \frac{\hat{\varphi}^2}{2} = \frac{1}{2 \sinh^2(\frac{\hat{a}}{2})} = \frac{1}{2} \operatorname{csch}^2\left(\frac{\hat{a}}{2}\right) \quad (2.10)$$

where the subscript ‘R’ denotes ‘repulsion’, since the force on the plate at $x=a$ is always positive, i.e., the interaction is always repulsive. The interaction energy can be computed by calculating the work done (per unit area) to move one of the two plates from a very long distance to the position $x = a$:

$$E \equiv -\frac{\text{Work}}{\text{Area}} = -\int_{\infty}^a f da' \quad (2.11)$$

Also, in normalized form:

$$\hat{E} = \frac{\epsilon\epsilon_0 E}{\sigma^2 l_D} = -\int_{\infty}^{\hat{a}} \hat{f} d\hat{a}' \quad (2.12)$$

Therefore, the repulsive energy per unit area can be calculated by,

$$\hat{E}_R = -\frac{1}{2} \int_{\infty}^{\hat{a}} \operatorname{csch}^2\left(\frac{\hat{a}'}{2}\right) d\hat{a}' = \frac{2}{e^{\hat{a}-1}} \quad (2.13)$$

For equal and opposite charge densities, $\sigma_2 = \sigma$; $\sigma_1 = -\sigma$. Following the same procedure, we find that at $(x = a/2)$, the potential is zero so that,

$$\hat{f}_A = -\frac{1}{2} \left(\frac{d\hat{\varphi}}{d\hat{x}} \right)^2 = -\frac{1}{2} \operatorname{sech}^2\left(\frac{\hat{a}}{2}\right) \quad (2.14)$$

where the subscript ‘A’ denotes ‘attraction’, since the interaction between opposite-charged surfaces is attractive. The normalized work of bringing the surfaces together is

$$\hat{E}_A = \frac{1}{2} \int_{\infty}^{\hat{a}} \operatorname{sech}^2\left(\frac{\hat{a}'}{2}\right) d\hat{a}' = -\frac{2}{e^{\hat{a}+1}} \quad (2.15)$$

where \hat{E}_A is the attractive energy per unit area. Figure 2.2 plots dimensionless force and energy for both the repulsive and attractive cases as a function of separation, \hat{a} . Note that, for the same magnitude of charge densities, the repulsive force is always higher in magnitude than the attractive force.

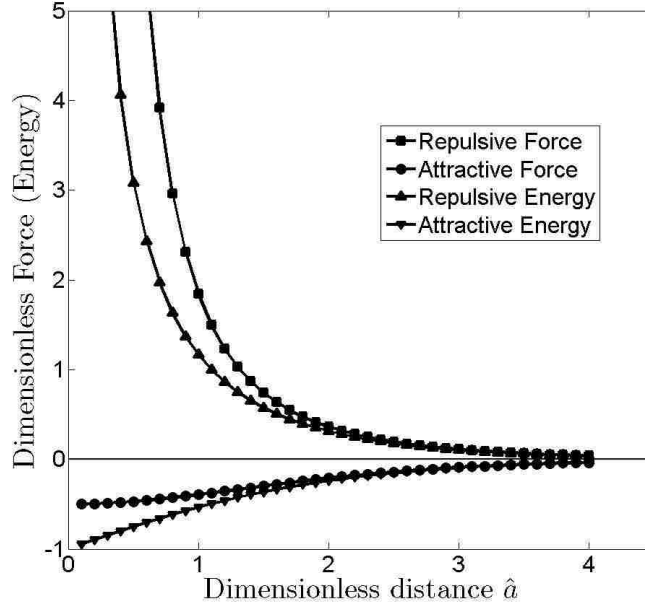


Figure 2.2 Force and interaction energy per unit area between two uniformly charged surfaces as a function of distance between them. For small separation distance, both force and energy of repulsion diverge to infinity whereas the force and energy of attraction remain finite. With increasing separation distance repulsion and attraction both decrease in magnitude, becoming equal and opposite for large separation.

2.3 Interaction between rigid surfaces with striped patterns of charge

As a first model for complementary surfaces we consider two surfaces, each with striped patterns of alternating positive and negative surface charge, and each with zero net charge (Figure 2.3). These two surfaces are set some distance, a , apart from each other. The width of each charged strip on the upper surface is b ; that of strips on the

lower surface is c . In this chapter, we assume both b and c to be much larger than the separation, a . In an experimental realization, the characteristic length scale of the gap, a , is expected to be the Debye screening length that is on the order of a few nm. On the other hand, length scales b and c , if generated by micro-contact printing, will have characteristic dimensions in the microns. Also, we imagine patterning an extended surface such that the total length of the striped surface will be in centimeters, much larger than length scales b and c . If the lateral length scales, b and c are not much larger than the gap, a , the problem of determining electrostatic interactions is two-dimensional and is considered in Ref. (30).

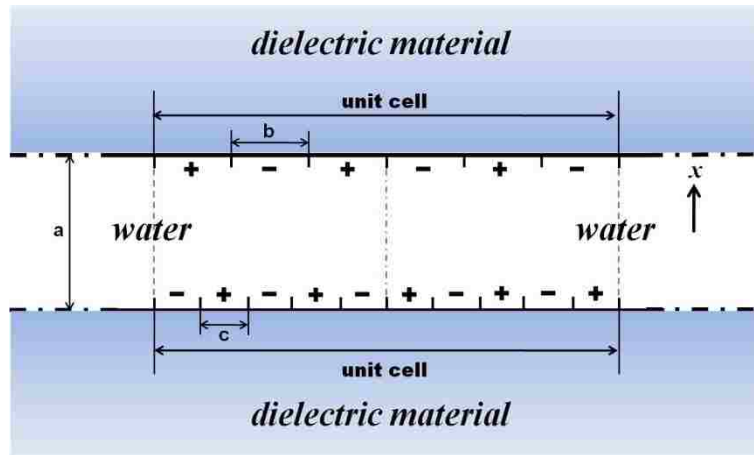


Figure 2.3 Schematic diagram of surfaces patterned with stripes of charge ($mb=nc$, in this case, $3b=5c$). Two infinitely large surfaces with striped patterns of alternating positive and negative charges on a dielectric material face each other in aqueous medium. The surface comprises repeats of a periodic unit cell with length $L=2mb=2nc$. This figure is not to scale since b and c are both assumed to be much larger than a .

If each charged strip faces a strip with charge of opposite sign, we have a perfectly matched pair of complementary surfaces that we expect would adhere well to each other. In another limit, let us say that the lateral size of the strips on one of the surfaces is very different from the other, e.g. $a \ll b \ll c$. Then, each strip of width ‘ c ’ on the lower surface is opposed by a surface with net zero charge. As we will show, in such a case we expect overall repulsion between the two surfaces. These two simple cases suggest that this family of surfaces should exhibit high selectivity in adhesion.

2.3.1 Electrostatics between two rigid surfaces

We begin by regarding the two surfaces as rigid and asking how the interaction force and energy between two surfaces with striped patterns of charge depends on the geometrical parameters such as stripe dimensions and separation between the surfaces. Since a is assumed to be much smaller than either b or c , we can assume that the interaction force and energy is dominated by 1-D interactions computed in the previous section. Specifically, we assume that the 2-D state near the region where charge density switches carries negligible contributions to the overall force and interaction energy. Therefore, in regions where similar charges face each other, the force and interaction energy per unit area are computed using Eqs. (2.10) and (2.13), respectively. Where opposite charges face each other the force and interaction energy per unit area are computed using Eqs. (2.14) and (2.15), respectively.

Suppose that the charged strips have been distributed as shown in Figure 2.3 with zero net charge on both surfaces. Consider a family of surfaces such that the lengths b and c are related as

$$mb = nc \quad (2.16)$$

where m and n are both positive integers and have no common factors other than unity. Assume that the surfaces are extended indefinitely. The surface then comprises repeats of a periodic unit cell with length $L_c = 2mb = 2nc$.

Let α be the fraction of area within a unit cell where like charges face each other. In the remaining fraction of the unit cell, $1 - \alpha$, charges are equal and opposite on two sides of the gap. Then, the net force and electrostatic interaction energy per unit area are:

$$\alpha \cdot \hat{f}_R + (1 - \alpha) \cdot \hat{f}_A \quad (2.17a)$$

$$\alpha \cdot \hat{E}_R + (1 - \alpha) \cdot \hat{E}_A \quad (2.17b)$$

Let us consider the situation where the two surfaces can adjust in the plane of the interface to find the configuration most favorable for adhesion (minimization of interaction energy). In Appendix A, we demonstrate that this favorable configuration is one in which the unit cell starts with segments on the opposite surfaces aligned and with opposite charges. For example, if $m=n=1$, the surfaces adjust so that $\alpha = 0$, i.e., charges are equal and opposite throughout the interface. Again, Figure 2.3 shows the configuration that minimizes interaction energy for $3b=5c$. For arbitrary combinations of m and n , we find:

i) If either m or n is even, $\alpha = 1/2$. This is because in the second half of the unit cell the charge pattern on the side with even divisions is repeated whereas on the side with odd divisions it is reversed.

Therefore, the minimum interaction energy and the corresponding force are

$$\hat{E}_I = \frac{1}{2}\hat{E}_A + \frac{1}{2}\hat{E}_R = \frac{2}{e^{2\hat{a}}-1}, \quad (2.18a)$$

$$\hat{f}_T = \frac{1}{2}\hat{f}_A + \frac{1}{2}\hat{f}_R = \frac{1}{\sinh^2(\hat{a})} \quad (2.18b)$$

Since $\frac{1}{\sinh^2(\hat{a})} > 0$, the overall interaction between such two surfaces is always repulsive.

ii) If m and n are both odd, interaction energy is minimized if each unit cell begins with aligned regions of opposite charge, for example, as shown in Figure 2.3. Also, we demonstrate in Appendix A that $\alpha = \frac{mn-1}{2mn}$. Thus, α is always less than 0.5 for this case.

The interaction energy and force are

$$\hat{E}_I = \alpha \cdot \hat{E}_R + (1 - \alpha) \cdot \hat{E}_A = \frac{mn+1}{2mn} \hat{E}_A + \frac{mn-1}{2mn} \hat{E}_R = \frac{2(mn-e^{\hat{a}})}{mn(e^{2\hat{a}}-1)} \quad (2.19)$$

$$\hat{f}_T = \alpha \cdot \hat{f}_R + (1 - \alpha) \cdot \hat{f}_A = \frac{mn+1}{2mn} \hat{f}_A + \frac{mn-1}{2mn} \hat{f}_R = \frac{2(mn-\cosh(\hat{a}))}{mn(\cosh(2\hat{a})-1)} \quad (2.20)$$

It is clear from Eq. (2.19) that at large distances $\hat{E}_I = \frac{-2e^{-\hat{a}}}{mn}$; the interaction is attractive and decreases in magnitude exponentially with distance. As distance $\hat{a} \rightarrow 0$ the energy and force both diverge to $+\infty$, and there is always repulsion, unless $m=n=1$, in which case normalized interaction energy and the interaction force go to a limiting value of -1 and -1/2, respectively. Therefore, except when $m=n=1$, there is always an equilibrium distance \hat{a}_e at which force is zero and where the two surfaces will come to rest naturally. Using Eq. (2.20), this condition is

$$\hat{f}_T = \alpha \cdot \hat{f}_R(\hat{a}_e) + (1 - \alpha) \cdot \hat{f}_A(\hat{a}_e) = \alpha \cdot \frac{1}{2} \operatorname{csch}^2\left(\frac{\hat{a}_e}{2}\right) - (1 - \alpha) \cdot \frac{1}{2} \operatorname{sech}^2\left(\frac{\hat{a}_e}{2}\right) = 0 \quad (2.21)$$

where we have used Eqs.(2.10) and (2.14). The dimensionless distance \hat{a}_e can be obtained by solving Eq. (2.21) (see Figure 2.4):

$$\hat{a}_e = 2 \operatorname{csch}^{-1}\left(\sqrt{\frac{1-2\alpha}{\alpha}}\right) \quad (2.22)$$

Eq. (2.22) provides the general relation between equilibrium separation \hat{a}_e and fraction,

α . For the special case under consideration in this section, $\alpha = \frac{mn-1}{2mn}$ and

$$\hat{a}_e = \operatorname{cosh}^{-1}(mn) \quad (2.23)$$

Substituting Eq. (2.22) or (2.23) into Eq. (2.19) give the interaction energy at equilibrium, \hat{E}_e . For two rigid surfaces, this quantity (if negative) is defined as the adhesion energy.

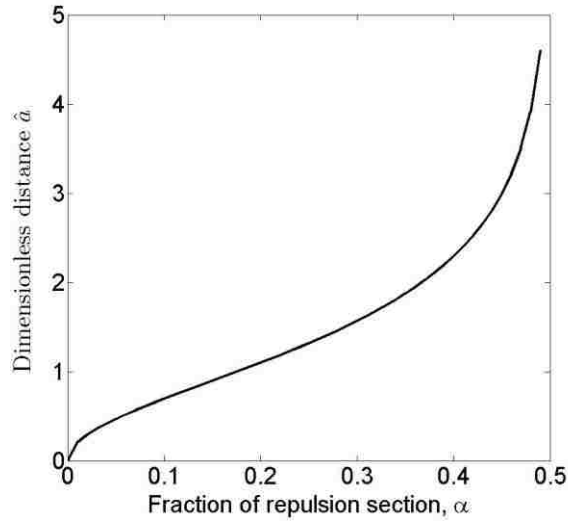


Figure 2.4 Equilibrium distance between two charged surfaces as a function of area fraction α of like charges across the gap.

For the special case of $m=n=1$, $\hat{a}_e = 0$, i.e., the force is always attractive, and within this model the surfaces come to rest in contact. Eq. (2.23) shows that, as the product mn increases, so does the equilibrium distance. Figure 2.5 plots the interaction force and energy versus \hat{a} for the case of $m=3$; $n=1$.

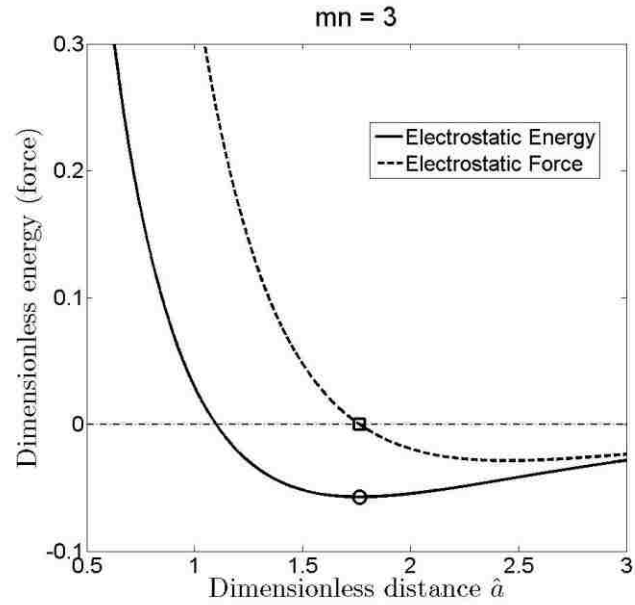


Figure 2.5 Interaction energy and total force when $mn=3$. The solid line represents the dimensionless total energy change as a function of distance between the two surfaces. The dashed line represents the force between the two surfaces. The square symbol indicates the point of zero force, corresponding to minimum energy (circular symbol).

When both m and n are odd, the pattern of surface charges in the second half of a unit cell is the reverse of that in the first half on both surfaces. Consider, for example, Figure 2.3 where $m=3$, $n=5$. Therefore for each region in the first half of the unit cell where the charges have the same sign, the corresponding region in the second half also has the same charge on the two sides. Similarly, for each region in the first half with

oppositely charged surfaces, the corresponding region in the second half also has oppositely signed charges. Due to this symmetry of electrostatic interactions, we only need to calculate the force and energy within half of one such unit cell. In addition, when later we allow the surfaces to deform, the node at the middle of the unit cell must remain fixed by symmetry.

2.3.2 Numerical results and discussion

In Figure 2.6 we show results for the adhesion energy per unit area, \hat{E}_I , for different combinations of m, n . Recall that when m, n are even numbers the surfaces repel so there is no adhesion. Normalized adhesion lies in the range $[-1, 0]$; greater adhesion is represented by a more negative number. Each square represents a single m, n combination and is colored using the non-linear scale shown to the right of the figure. The results of the case where the two surfaces are rigid and $m > n$ are shown below the diagonal of this matrix. The results shown above the diagonal will be discussed later.

From Figure 2.6, it is clear that $m=n$ represents the highest adhesion. Other combinations that show adhesion are $3m=n, 5m=n, 7m=n, \dots$, and $5m=3n, 7m=3n$, and so on. Note that configurations very ‘close’ to each other in this space can have very different adhesion energy. For example, the combination $(15, 5)$ is adhesive but $(15, 4)$ is repulsive. Even more dramatically, the combination $(20, 20)$ is highly adhesive but $(20, 19)$ is repulsive. (More strictly, the equilibrium separation \hat{a}_e increases to infinity for cases such as $(20, 19)$ that are repulsive. Therefore, the corresponding “adhesion” in these cases vanishes.) Therefore, this simple motif of two rigid surfaces patterned with

alternating stripes of equal and opposite charge is predicted to show strong selectivity of adhesion to surfaces with certain specific characteristic length, and to show overall repulsion against most other surfaces.

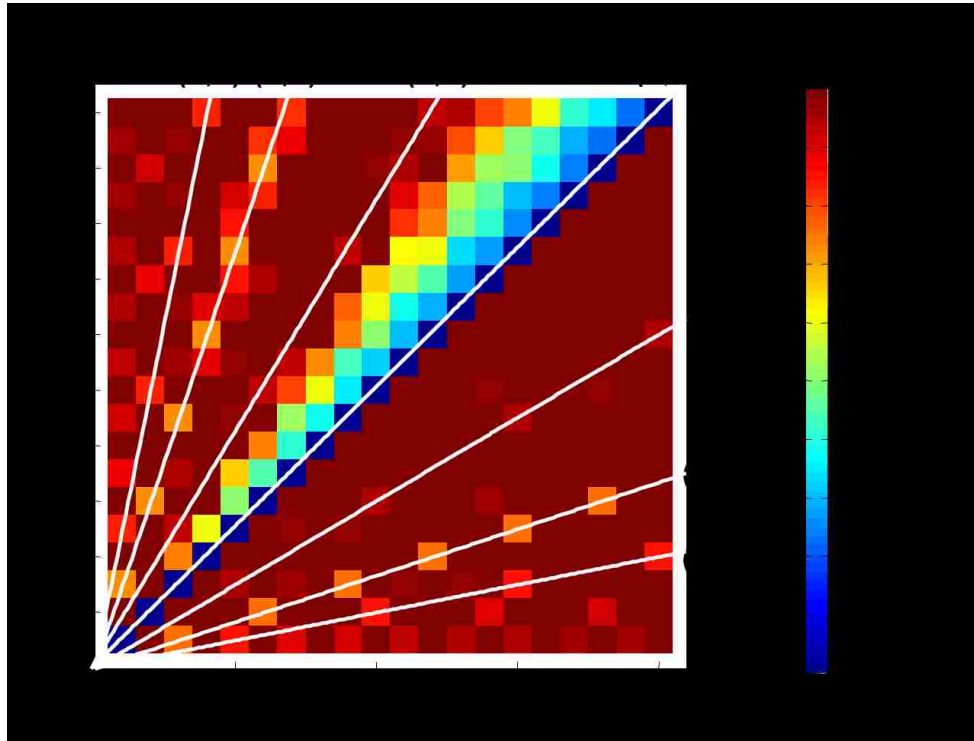


Figure 2.6 Plots of interaction energy between two patterned surfaces for different m and n . (Negative values represent adhesion.) Each square represents a single (m, n) combination and is colored using the (non-linear) scale shown to the right of the figure. Results below the diagonal, i.e., for $m > n$, are for two rigid surfaces; those above the diagonal ($m < n$) are for a deformable surface with normalized stiffness, $\hat{k}_0 = 10$. Note that the best combination is for $m = n$. Combinations of m and n on some other rays emanating from the origin, such as $m/n = 3/1$ or $1/3$; $m/n = 3/5$ or $5/3$, etc. also give rise to net attraction. Note that for rigid surfaces even the slightest variation from one of these combinations results in strong repulsion. For example, while $(20, 20)$ results in the highest adhesion, $(20, 19)$ results in net repulsion. There is therefore strong selectivity of one surface for another. The effect of deformability, shown above the diagonal reduces strong selectivity.

To estimate the sort of adhesion energies predicted by our model, let's consider an example of two rigid surfaces with a realistic charge density of one elementary charge per square nanometer, which is about 0.16 Coulombs per square meter. Suppose the surfaces are placed in an aqueous solution at 300 K and one mM concentration of a 1-1 electrolyte (e.g., NaCl), for which Debye screening length l_D is about 10 nanometers. According to Figure 2.6 and the normalization (Eq. (2.8)), the highest energy (adhesion) is achieved when $(m,n) = (1, 1)$, with a value that is approximately 361 mJ/m^2 . For the case of $(3, 1)$ combination, the equilibrium distance between the surfaces is found to be about 18 nanometers, and the total energy (adhesion) is only about 42.5 mJ/m^2 , which is much smaller than for the $(1, 1)$ combination. For case $(5, 1)$, the equilibrium distance increases to 23 nanometers and the adhesion energy decreases to about 34.6 mJ/m^2 .

2.4 Interaction between elastic surfaces with striped patterns of charge

So far we have considered rigid charged surfaces. This led to a conclusion that surfaces with patterned charges will show high selectivity. However, one might ask: how is it possible that two surfaces with, say $m=1000$, $n=999$, should have strong repulsion from each other while another two with $m=n=1000$ attract each other strongly? A related, practical question is, what use is such selectivity if the slightest misalignment or difference in dimensions will destroy adhesion? We notice that with just a small amount of deformation, $(1000, 999)$ can be transformed into $(1000, 1000)$, and this suggests that there exists a strong electrostatic driving force for such a deformation. That is, selectivity

is bound to be limited and conditioned by deformability. To explore this idea, we have created a simple model described below.

2.4.1 One-dimensional model of elastically deformable surfaces patterned with stripes of charge

In this 1-D problem, we start with the two surfaces introduced above, each with striped patterns of alternating positive and negative surface charges summing to zero net charge and aligned to be in phase, as defined previously. In addition, we allow nodes on both surfaces to move, but only sideways in the y direction, thus preserving the flatness of the dielectric layer. The movement of these nodes is driven by reduction in electrostatic free energy, and restrained by increase in elastic strain energy, until the system reaches a state of equilibrium. We assume that, although the materials on either side can deform (change the lengths on each side within every segment), the charge on each segment remains proportional to the current length, which means that the amount of surface charge can be changed by deformation. A physical realization of this assumption could be an elastomer in which additional surface groups would be exposed if the area of the surface were increased.

Suppose we have two plane surfaces (Figure 2.7). The upper surface has m segments with alternating positive and negative charges and $(m+1)$ nodes. Similarly, the lower surface has n segments with alternating charge, a different segment length, and $(n+1)$ nodes. We mark each segment by a Roman number and each node in an Arabic number. Let $y(i)$ and $u(i)$ be the location and displacement of node i , respectively

($1 \leq i \leq m+n+2$). We define displacement $u(i)$ to be positive if oriented in the positive y direction. We analyze the family of surfaces given by Eq. (2.16). We generally analyze a half of a unit cell arranged such that the first regions on opposite sides of the gap, starting at the left, have opposite charge. As discussed earlier, this ensures that the starting configuration has the lowest interaction energy and greatest adhesion energy for rigid surfaces. Therefore, as shown in Figure 2.7, $y(1) = y(m+2)$ and $y(m+1) = y(m+n+2)$. Moreover, we set $u(1) = u(m+1) = u(m+2) = u(m+n+2) = 0$, i.e., while we allow deformations within a unit cell we do not allow any overall change in area.

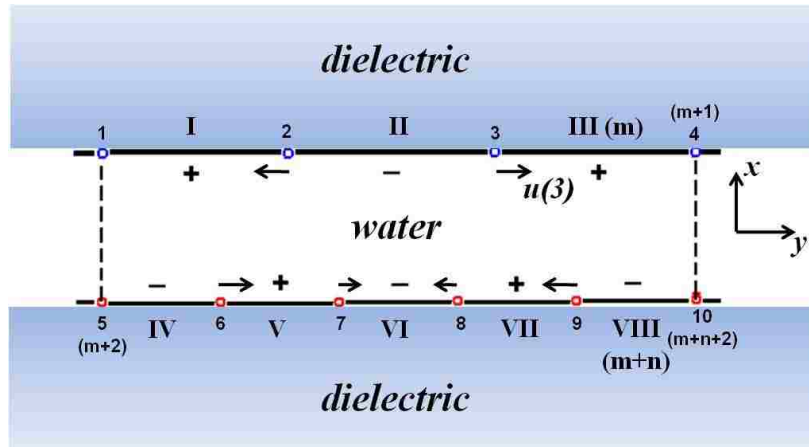


Figure 2.7 Schematic diagram of a 1-D elastic surface with patterned charge (half unit cell: $3b=5c$).

It turns out to be important to handle potentially large deformations of the surfaces to prevent collapse of two neighboring nodes. For this reason, we model the surfaces as one-dimensional hyperelastic neo-Hookean materials.^{27, 28} For small deformations, the behavior is linearly elastic.

2.4.2 Model and algorithm

2.4.2.1 Electrostatic energy

Consider a general node i , say on the upper surface. Holding all other nodes fixed, motion of this node i by $u(i)$ changes the electrostatic energy by a magnitude of $U_{ele}^i = |(-E_R + E_A) \cdot u(i)|$ (for unit out-of-plane width), as long as the motion is small enough so that the node does not cross another node on the lower surface. Define dimensionless displacement as $\hat{u}(i) = \frac{u(i)}{l_D}$. The sign of the electrostatic energy change (positive for increasing repulsion; negative for increasing attraction) can be obtained by examining the sign of charge density on the two sides in the segments adjacent to node i and the segment opposite to node i).

Define $sign(opp)$ as the sign of the segment opposite the node i , and $sign(local)$ as the sign of the step in charge density moving from the segment to the left of node i to its right (see Table 2.1 for examples).

Based on these quantities, for each node i , the change of dimensionless electrostatic energy after deformation is:

$$\hat{U}_{ele}^i = \frac{U_{ele}^i \epsilon \epsilon_0}{\sigma^2 l_D^2} = (-\hat{E}_R + \hat{E}_A) \cdot \hat{u}(i) \cdot sign(opp, i) \cdot sign(local, i) \quad (2.24)$$

The total change in electrostatic energy due to motion of nodes is obtained by summing up the contribution from each node:

$$\hat{U}_{ele} = \sum_{i=1}^{r+n+2} \Delta \hat{E}(i) \cdot \hat{u}(i) \cdot sign(opp, i) \cdot sign(local, i) \quad (2.25)$$

where $\Delta \hat{E}(i)$ is $(-\hat{E}_R + \hat{E}_A)$.

Table 2.1 Examples of arrangements for a given node, i , and definition of terms $sign(opp)$ and $sign(local)$ that determine the change in electrostatic energy per unit movement of node i .

Position of node i	Signs
	$sign(opp) = +1$ $sign(local) = -1$
	$sign(opp) = -1$ $sign(local) = +1$

2.4.2.2 Elastic energy

As an illustrative model to capture the penalty of imposing deformations, we model segments on both sides as springs under uniaxial strains imposed by differences in displacements on its two ends. The entire system is therefore composed by two strips of linked springs (the upper one has m springs in series, and the lower one has n springs in series). This model suppresses other deformation modes such as out of plane deformation which will change the electrostatic interaction. Nevertheless, we believe that this simple model captures the beneficial effect of deformation on adhesion.

Let $L_{0,i}$ and L_i be the initial and stretched lengths for a segment i , respectively.

The stretch ratio for this segment is,

$$\lambda_i = \frac{L_i}{L_{0,i}} = \frac{L_{0,i} + u_+ - u_-}{L_{0,i}} = \frac{\hat{L}_{0,i} + \hat{u}_+ - \hat{u}_-}{\hat{L}_{0,i}} \quad (2.26)$$

where u_+ is the displacement of the node at the right end of segment i and u_- is the displacement of the node at its left end. All u_+ , u_- and $L_{0,i}$ are normalized by the Debye screening length l_D ($\hat{u}_+ = \frac{u_+}{l_D}$, $\hat{u}_- = \frac{u_-}{l_D}$ and $\hat{L}_{0,i} = \frac{L_{0,i}}{l_D}$).

We model the spring as comprised of a Neo-Hookean solid[°] for which the strain energy density is given by^{27, 28}

$$\Phi = Y(I_1 - 3)/6 \quad (2.27)$$

$$I_1 = \lambda^2 + \frac{2}{\lambda} \quad (2.28)$$

where Y is the small strain Young's modulus²⁷. Substituting Eq. (2.28) into Eq. (2.27), the expression for strain energy density becomes

$$\Phi = Y(\lambda^2 + \frac{2}{\lambda} - 3)/6 \quad (2.29)$$

In this model, the spring cannot be compressed indefinitely ($\lambda \rightarrow 0$) since the strain energy density becomes unbounded in this limit. For any segment i , the elastic energy can be calculated by (in dimensionless form)

$$\hat{U}_{ela,i} = \hat{\Phi}_i \hat{L}_{0,i} \hat{A}_0 = \hat{Y}(\lambda_i^2 + \frac{2}{\lambda_i} - 3) \cdot \hat{L}_{0,i} \hat{A}_0 / 6 \quad (2.30)$$

where, $\hat{U}_{ela} = \frac{\epsilon \epsilon_0}{\sigma^2 l_D} \cdot U_{ela}$, and $\hat{Y} = \frac{\epsilon \epsilon_0 l_D}{\sigma^2} Y$ is the normalized modulus. The initial area of cross-section, A_0 , is normalized by l_D^2 ($\hat{A}_0 = \frac{A_0}{l_D^2}$) and we assume that A_0 is the same for every segment.

The total elastic energy in dimensionless form is

$$\hat{U}_{ela} = \sum_{i=1}^{m+n} \hat{Y}(\lambda_i^2 + \frac{2}{\lambda_i} - 3) \cdot \hat{L}_{0,i} \hat{A}_0 / 6 \quad (2.31)$$

[°] For small deformations, this model reduces to Hooke's law for a linear spring. For large deformations, it is nonlinear. Eq. (2.29) shows that the spring stiffens indefinitely under compression, removing the unphysical behavior predicted by a linear model, in which neighboring nodes can collapse.

For small strains, since $\lambda_i \approx 1$ for each segment, the expression for elastic energy is approximately:

$$\hat{U}_{ela} \approx \sum_{i=I}^{m+n} \frac{1}{2} \left(\frac{\hat{Y}\hat{A}_0}{\hat{L}_{0,i}} \right) \cdot (\hat{u}_+ - \hat{u}_-)^2 \quad (2.32)$$

Compare this to the case of a linear spring,

$$\hat{U}_{ela} = \sum_{i=I}^{m+n} \frac{1}{2} \hat{k}_i (\hat{u}_+ - \hat{u}_-)^2 \quad (2.33)$$

where k_i is the spring constant for segment i ($i=I, II, \dots, m+n$), which has the dimensionless form as $\hat{k}_i = \frac{\epsilon\epsilon_0}{\sigma^2} k_i$.

2.4.2.3 Equilibrium

The total energy consists of electrostatic and elastic contributions,

$$\hat{U}_{tot} = \hat{U}_{ele} + \hat{U}_{ela} \quad (2.34)$$

In equilibrium, for a given separation \hat{a} , the first derivative of the total energy with respect to each degree of freedom should vanish:

$$\frac{\partial \hat{U}_{tot}}{\partial \hat{u}_i} = \frac{\partial (\hat{U}_{ele} + \hat{U}_{ela})}{\partial \hat{u}_i} = \frac{\partial \hat{U}_{ele}}{\partial \hat{u}_i} + \frac{\partial \hat{U}_{ela}}{\partial \hat{u}_i} = 0 \quad (2.35)$$

According to Eq. (2.25),

$$\frac{\partial \hat{U}_{ele}}{\partial \hat{u}_i} = \Delta \hat{E}(i) \cdot \text{sign}(opp, i) \cdot \text{sign}(local, i) \quad (2.36)$$

The contribution to Eq. (2.35) from elastic energy generally is from each of the elements adjoining the node i . In our case, except for nodes at the ends that are handled by boundary conditions, each node has contributions from two terms in Eq. (2.31), which

are $\hat{U}_{ela,i-1}$ and $\hat{U}_{ela,i}$ (see Eq. (2.30)). So the derivative of elastic energy can be calculated by,

$$\frac{\partial \hat{U}_{ela}}{\partial \hat{u}_i} = \frac{\partial \hat{U}_{ela,i-1}}{\partial \lambda_{i-1}} \frac{\partial \lambda_{i-1}}{\partial \hat{u}_i} + \frac{\partial \hat{U}_{ela,i}}{\partial \lambda_i} \frac{\partial \lambda_i}{\partial \hat{u}_i} = \hat{Y} \hat{A}_0 \cdot \left(\lambda_{i-1} - \frac{1}{\lambda_{i-1}^2} - \lambda_i + \frac{1}{\lambda_i^2} \right) / 3 \quad (2.37)$$

For small strains, the linearized form of Eq. (2.37) is:

$$\frac{\partial \hat{U}_{ela}}{\partial \hat{u}_i} \approx \frac{\hat{Y} \hat{A}_0}{\hat{L}_{0,i-1}} (\hat{u}_i - \hat{u}_{i-1}) - \frac{\hat{Y} \hat{A}_0}{\hat{L}_{0,i}} (\hat{u}_{i+1} - \hat{u}_i) = \hat{k}_{i-1} (\hat{u}_i - \hat{u}_{i-1}) - \hat{k}_i (\hat{u}_{i+1} - \hat{u}_i) \quad (2.38)$$

The right hand side of Eq. (2.38) is the same as the first derivative of the elastic energy for small displacements (Eq. (2.33)) respect to \hat{u}_i .

Substituting Eq. (2.36) and Eq. (2.37) into Eq. (2.35), we find that for each node i :

$$\Delta \hat{E}(i) \cdot \text{sign}(opp, i) \cdot \text{sign}(local, i) + \hat{Y} \hat{A}_0 \cdot \left(\lambda_{i-1} - \frac{1}{\lambda_{i-1}^2} - \lambda_i + \frac{1}{\lambda_i^2} \right) / 3 = 0 \quad (2.39)$$

which represents a system of nonlinear equations for the unknown nodal displacements subject to boundary conditions $\hat{u}_1 = \hat{u}_{m+1} = \hat{u}_{m+2} = \hat{u}_{m+n+2} = 0$. Note that if we take the material on the two sides to be the same, the normalized set of Eq. (2.39) depend on a single dimensionless parameter, $\hat{k}_0 \equiv \hat{Y} \hat{A}_0$ since $\Delta \hat{E}(i)$ is a function only of the gap \hat{a} through Eqs. (2.13) and (2.15).

We solve the system of Eq. (2.39) for fixed \hat{a} using a *viscous relaxation* technique²⁹. Define the left-hand side of Eq. (2.39) to be the residual, and introduce a fictitious viscous term in the equation such that the rate of change of displacements is proportional to the residual:

$$\hat{\eta} \hat{u}_i = \Delta \hat{E}(i, t) \cdot \text{sign}(opp, i) \cdot \text{sign}(local, i) + \hat{k}_0 \cdot \left(\lambda_{i-1,t} - \frac{1}{\lambda_{i-1,t}^2} - \lambda_{i,t} + \frac{1}{\lambda_{i,t}^2} \right) / 3 \quad (2.40)$$

Approximating $\hat{u} = (\hat{u}_{t+\Delta t} - \hat{u}_t) / \Delta t$, Eq. (2.40) becomes:

$$\hat{u}_{i,t+\Delta t} = \Delta t \cdot \hat{\eta}^{-1} \cdot \left[\Delta \hat{E}(i, t) \cdot \text{sign}(\text{opp}, i) \cdot \text{sign}(\text{local}, i) + \hat{k}_0 \left(\lambda_{i-1,t} - \frac{1}{\lambda_{i-1,t}^2} - \lambda_{i,t} + \frac{1}{\lambda_{i,t}^2} \right) / 3 \right] + \hat{u}_{i,t} \quad (2.41)$$

Eq. (2.41) is marched forward in time with a sufficiently small time step to ensure stability until we obtain a solution with residual smaller than a specified tolerance. Two sorts of events need special handling. The first occurs if the deformation causes a node on one surface to cross a node on the other surface. Because such an event results in a sudden change in $\text{sign}(\text{opp}, i)$, often the solution will not converge. We handle such events by introducing a transition function that smoothly changes the value of $\text{sign}(\text{opp}, i)$. The second event occurs if a linear elastic model is used to represent deformation and if the electrostatic driving forces dominate over the elastic resistance. Under such a circumstance, some springs can be compressed to zero length, i.e., nodes can cross on the same side. In the neo-Hookean model such a situation does not arise but for the linearly elastic model it can and we terminate the computation when it does since node crossing on the same side violates the condition of small deformations and is not a physically meaningful event.

Once we have obtained new displacements for every node, we compute the area fraction of repulsive interactions, α , and then find a new value of \hat{a} using Eq. (2.22). This procedure is repeated iteratively until we achieve a converged equilibrium solution in which the total energy is minimized with respect to all \hat{u}_i and separation, \hat{a} .

2.4.3 Analysis of a simple case, (m,n)=(1,3)

We begin by examining a simple example in some detail. Consider the combination of $m=1$ and $n=3$ (Figure 2.8) and let $\hat{L} = 1$. Because the two ends are fixed for both sides, only two nodes on the lower surface are free to deform and, by symmetry, they must have equal and opposite deformations, defined as δ (dimensionless).

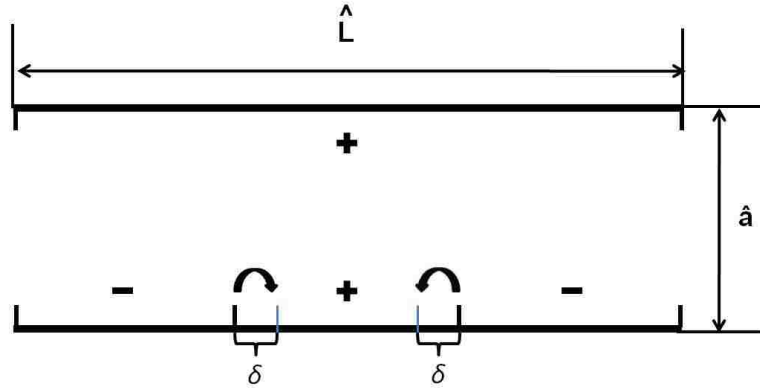


Figure 2.8 Illustration of deformation of $(m,n)=(1,3)$ pattern. The end-nodes are fixed and only the two central nodes on the lower surface can deform. By symmetry, their deformation is equal and opposite.

In this case, the upper surface does not deform, so its elastic energy remains fixed at zero. The total energy is the summation of the electrostatic energy and elastic energy of the lower surface:

$$\hat{U}_{tot} = \hat{U}_{ele} + \hat{U}_{ela} \quad (2.42)$$

where the electrostatic energy and elastic energy (Eq. (2.31)) can be expressed by:

$$\hat{U}_{ele} = \hat{E}_A \cdot \left(2\delta + \frac{2}{3}\right) + \hat{E}_R \cdot \left(\frac{1}{3} - 2\delta\right) = -\frac{2}{e^{\hat{a}+1}} \cdot \left(2\delta + \frac{2}{3}\right) + \frac{2}{e^{\hat{a}-1}} \cdot \left(\frac{1}{3} - 2\delta\right) \quad (2.43)$$

$$\hat{U}_{ela} = 2 \frac{\hat{Y}}{6} \left[\left(\frac{\delta + \frac{1}{3}}{\frac{1}{3}} \right)^2 + \frac{2 \cdot \frac{1}{3}}{\delta + \frac{1}{3}} - 3 \right] \cdot \frac{1}{3} \cdot \hat{A}_0 + \frac{\hat{Y}}{6} \left[\left(\frac{\frac{1}{3} - 2\delta}{\frac{1}{3}} \right)^2 + \frac{2 \cdot \frac{1}{3}}{\frac{1}{3} - 2\delta} - 3 \right] \cdot \frac{1}{3} \cdot \hat{A}_0$$

$$= \frac{1}{3} \frac{\hat{Y}}{6} \hat{A}_0 \left[54\delta^2 + \frac{4}{3\delta+1} + \frac{2}{1-6\delta} - 6 \right] = \frac{1}{18} \hat{k}_0 \cdot \left[54\delta^2 + \frac{4}{3\delta+1} + \frac{2}{1-6\delta} - 6 \right] \quad (2.44)$$

Summing up Eqs. (2.43) and (2.44), the total energy per unit area is

$$\hat{E}_{tot} = -\frac{2}{e^{\hat{a}+1}} \cdot \left(2\delta + \frac{2}{3} \right) + \frac{2}{e^{\hat{a}-1}} \cdot \left(\frac{1}{3} - 2\delta \right) + \frac{1}{18} \hat{k}_0 \left[54\delta^2 + \frac{4}{3\delta+1} + \frac{2}{1-6\delta} - 6 \right] \quad (2.45)$$

which is a function of two variables (δ, \hat{a}) . We find numerically the values of (δ, \hat{a}) at which the energy is minimized.

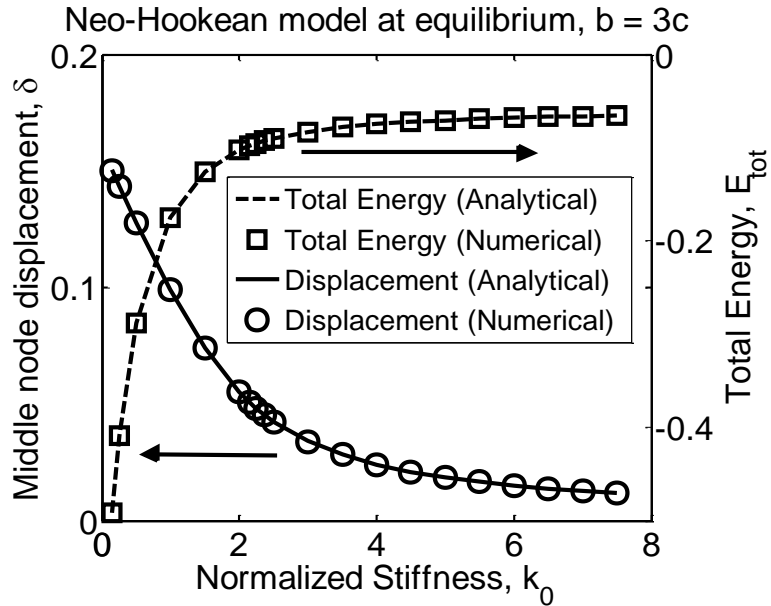


Figure 2.9 Middle node displacement (δ) and total energy at equilibrium as a function of stiffness when $\hat{L} = 1$ (stripe combination $b=3c$). As the stiffness reduces, deformation of the lower surface increases as the middle two nodes on that side move closer. The total energy at equilibrium shows that it can be reduced significantly due to increase of deformability.

Figure 2.9 shows the analytical predictions (which are consistent with the numerical results) for both the displacement of the two middle nodes on the lower surface and the total energy per unit area as functions of spring constant. For small stiffness, we find that the deformations can be quite large. We identify the total energy at equilibrium as the adhesion energy. It includes a negative contribution from (net) electrostatic attraction and a positive contribution due to elastic energy. That is, the release of elastic energy aids interfacial separation. However, one should be mindful that in more complex systems, not all the stored elastic energy is available to propagate an interfacial crack. Figure 2.9 also shows how the total energy (electrostatic + elastic), identified here with the adhesion energy of the system, decreases as the deformation increases.

2.4.4 How deformability affects selectivity

We now examine the entire family of surfaces given by Eq. (2.16) and return to the questions raised at the beginning of Section 2.4. To explore how deformability affects the adhesion selectivity seen in the right lower half of Figure 2.6 ($m > n$), we vary the elasticity by changing the parameter \hat{k}_0 . For convenience, in the following discussion, we take the total dimensionless length of each surface equal to one ($\hat{L}_{tot} = 1$). As an example, Figure 2.10 shows initial and final nodal positions for a (3,5) surface for two different values of stiffness as predicted by the neo-Hookean model.

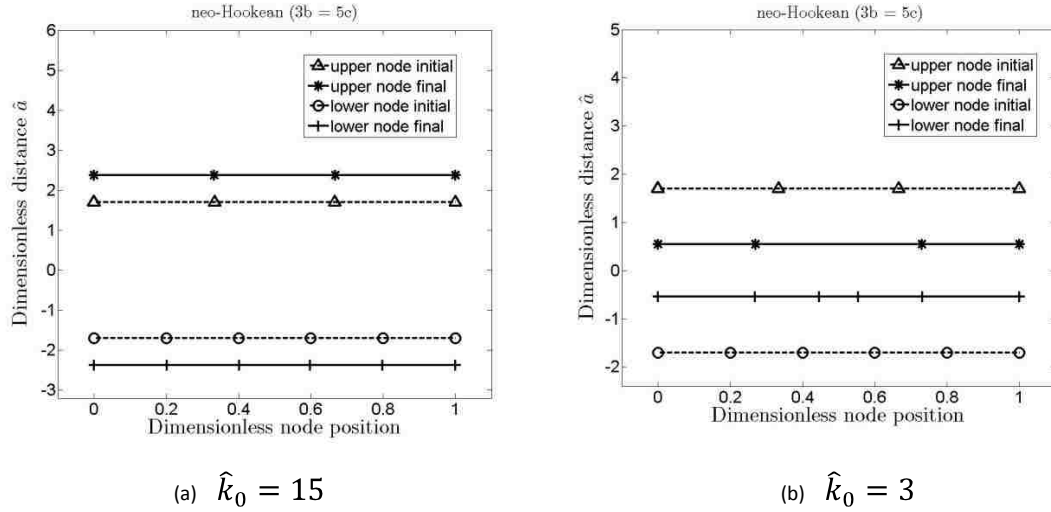


Figure 2.10 Initial and equilibrium nodal positions for a (3,5) surface. Plot (a) is the prediction of the neo-Hookean model for $\hat{k}_0 = 15$. For this relatively large stiffness, the deformation is small, and the associated reduction in energy is slight. Plot (b) shows the nodal displacements when $\hat{k}_0 = 3$; the deformation is significantly larger.

In Figure 2.6 we show results of the total adhesion energy, \hat{E}_e , for different (m,n) after deformation using the neo-Hookean model with $\hat{k}_0 = 10$. These results are presented above the diagonal of this matrix, i.e., for $m < n$. Again, $m = n$ represents the highest adhesion achievable. However, we notice that deformability has a profound influence on selectivity. It “smooths out” the sharp selectivity predicted for rigid surfaces. Specifically, ‘compositions’ close to the selective ones such as (1, 3) and (3, 5) in the space of m and n , find favorable modes of deformation to increase their adhesion. This is particularly true for compositions near $m = n$.

At the end of Section 2.3, we showed that for realistic charge densities in a 1 mM 1-1 electrolyte the (1, 1) combination is predicted to have significant adhesion but that this reduces significantly for other combinations; the second best (3, 1) is nearly a factor of ten lower in adhesion. To illustrate the beneficial effect of deformability, let us

consider the same example where now the patterned charge is on a deformable elastomer instead of a rigid surface. Young's modulus of a representative elastomer, e.g., polydimethylsiloxane (PDMS), is about 5MPa. If the dielectric has a thickness of 200 microns and width of about 3.6 mm, the parameter $\hat{k}_0 \approx 10$.

From the region of the Figure 2.6 above the diagonal, we observe that the maximum adhesion is still given by case (1, 1), and its value is the same as for rigid surfaces. However, for other combinations, the deformability allows greater adhesion. For example, for the case (1, 3), the total energy increases a little, to about 65 mJ/m². Much greater changes in adhesion are predicted when either m or n (Eq. (2.16)) is even, especially for combinations 'near' the diagonal in Figure 2.6. Recall that for the rigid case, if either m or n are even, the net force between the surfaces is repulsive. The originally repulsive case (4, 5) becomes adhesive and the adhesion energy is about 59 mJ/m²; the case (19, 20) has adhesion energy of 216 mJ/m², which is a great enhancement of adhesion and approaches that of (1, 1).

2.5 Summary and conclusions

To explore whether and how adhesion selectivity can be designed using electrostatic complementarity, we have analyzed the interactions between two surfaces patterned with stripes of charge. We have shown that strong adhesion can be achieved by exact complementarity between two such pattern-charged surfaces. If the materials are rigid, we predict strong selectivity, which can be rather more a bane than a benefit because even a slight difference in dimensions or misalignment can drastically reduce

adhesion. We show that deformability of the materials, modeled here by non-linear (neo-Hookean) elasticity, strongly alters adhesion selectivity. Specifically, by allowing the surfaces to deform, compositions similar to each other are found to have similar adhesion. The kind of striped charges we have analyzed can be achieved experimentally by microcontact printing of appropriate molecules onto an elastomer. We have specifically analyzed the case where charges result from ionization of terminal groups on such molecules in aqueous medium. As such, we expect that the predictions of our work are eminently realizable experimentally.

2.6 References

- [1] Scherge, M.; Gorb, S. N. *Biological Micro- and Nano-Tribology, Nature's Solutions*, Springer Verlag: Berlin, 2001.
- [2] Gorb, S. N. *Proc. R. Soc. Lond. B: Biol. Sci.* **1999**, 266, 525.
- [3] Alberts, B.; Johnson, A.; Lewis, J.; Raff, M.; Roberts, K.; Walter, P. *Molecular Biology of the Cell* 5th edition, Garland Science, Taylor & Francis Group: New York, 2008.
- [4] Bernstein, F.; Koetzle, T.; Williams, G.; Meyer, E.; Brice, M.; Rodgers, J.; Kennard, O.; Shimanouchi T.; Tasumi. M. *J. Mol. Biol.* **1977**, 112, 535.
- [5] Chothia, C.; Janin, J. *Nature* **1975**, 256, 705.
- [6] Colman, P. *Advan. Immunol.* **1988**, 43, 99.
- [7] Davies, D.; Padlan, E. *Annu. Rev. Biochem.* **1990**, 59, 439.
- [8] Nomura, M.; Held, W.; Nomura, M.; Tissiers, A.; Lengyel, P. *Ribosomes*, eds. 193, 1974.
- [9] Lamarche, O.; Platts, J. A. *Phys. Chem. Chem. Phys.* **2003**, 5, 677.
- [10] de Mestral, G. *U.S. patent* **1955**, 2717437.

- [11] Anastasiadis, S. H.; Retsos, H.; Pispas, S. ; Hadjichristidis, N.; Neophytides, S. *Macromolecules* **2003**, *36*, 1994.
- [12] Koberstein, J. T. *J. Poly. Sci. B* **2004**, *42*, 2942.
- [13] Koberstein, J. T.; Duch, D. E.; Hu, W.; Lenk, T. J.; Bhatia, R.; Brown, H. R.; Lingelser, J. P.; Gallot, Y. *J. Adh* **1998**, *66*, 229.
- [14] Zhou, F.; Huck, W. T. S. *Phys. Chem. Chem. Phys.* **2006**, *8*, 3815.
- [15] Ko, H.; Zhang, Z.; Chueh, Y.; Ho, J.; Lee, J.; Fearing, R.; Javey, A. *Adv. Func. Mater.* **2009**, *19*, 3098.
- [16] Vajpayee, S.; Khare, K.; Yang, S.; Hui, C.; Jagota, A. *Adv. Func. Mater.* **2010**, *21*, 547.
- [17] Kokkoli, E.; Zukoski, C. F. *Langmuir* **2001**, *17*, 369.
- [18] McCoy, A.; Chandana Epa, V.; Colman, P. *J. Mol. Biol.* **1997**, *268*, 570.
- [19] Weiner, P.; Langridge, R.; Blaney, J.; Schaefer, R.; Kollman, P. *Proc. Natl. Acad. Sci.* **1982**, *79*, 3754.
- [20] Naray-Szabo, G. *J. Mol. Graphics* **1989**, *7*, 76.
- [21] Debye, P.; Huckel, E. *Physikalische Zeitschrift* **1923**, *24*, 185.
- [22] Gouy, G. L. *J. de phys.* **1910**, *9*, 457.
- [23] Chapman, D. L. *Philos. Mag.* **1913**, *25*, 475.
- [24] Schlick, T. *Molecular Modeling and Simulation, an Interdisciplinary Guide*, Springer: New York, 2002.
- [25] Russel, W. B.; Saville, D. A.; Schowalter, W. R. *Colloidal Dispersions* Cambridge University Press, 1989.
- [26] Khripin, C.; Jagota, A. ; Hui, C-Y. *J. Chem. Phys.* **2005**, *123*, 134705.
- [27] Ogden, R. *Non-linear Elastic Deformations*, New York: Dover, 1984.
- [28] Yeoh, O. H. *Rubber Chem. Technol.* **1993**, *66*, 754.
- [29] Golub, G. H.; Van Loan, C. F. *Matrix Computations*, 2nd edition, Johns Hopkins: Baltimore MD, 1989.
- [30] Jin, C.; Bai, Y.; Jagota, A.; Hui, C-Y. *J. Appl. Phys.* **2011**, *110*, 054903.

Chapter 3 Adhesion of Micro-channel Based Complementary Surfaces^f

In this chapter, we show that highly enhanced and selective adhesion can be achieved between surfaces patterned with complementary micro-channel structures. An elastic material, poly (dimethylsiloxane) (PDMS), was used to fabricate such surfaces by molding into a silicon master with micro-channel profiles patterned by photolithography. We carried out adhesion tests on both complementary and mismatched micro-channel/micro-pillar surfaces. Adhesion, as measured by energy release rate required to propagate an interfacial crack, can be enhanced by up to forty times by complementary interfaces compared to a flat control, and slightly enhanced for some special non-complementary samples, despite the nearly negligible adhesion for other mismatched surfaces. For each complementary surface, we observe defects in the form of visible striations, where pillars fail to insert fully into the channels. The adhesion between complementary micro-channel surfaces is enhanced due to a combination of a crack-trapping mechanism and friction between a pillar and channel, and is attenuated by the presence of defects.

^f Adapted with permission from: Singh, A. K.; Bai, Y.; Nadermann, N.; Jagota, A.; Hui, C-Y."Adhesion of Microchannel-Based Complementary Surfaces." *Langmuir* **2012**, *28*(9), 4213-4222. Copyright 2012 American Chemical Society.

3.1 Introduction

Enhanced adhesion and selectivity between contact surfaces are highly desirable and have the potential for novel designs of high-level functional materials. In nature, biological attachment devices are functional systems for temporary or permanent attachment of an organism to the substrate, to another organism, or temporary interconnection of body parts within an organism. Their design varies enormously in relation to different functional loads ¹. For example, patterns of protuberances of different origin on surfaces play important roles in animals' locomotion, such as in insects, spiders, and lizards ²⁻⁸. Studies of these structures have shown that the contact mechanical properties (including adhesion and friction) can be modified by near-surface architecture independent of the surface chemistry. In fact, within the last decade, the development of these bio-mimetic and bio-inspired structured surfaces has been pursued actively by many research groups ^{3, 6-20}.

Although bio-inspired attachment systems have been broadly studied, most of the recent work has been on the adhesion and friction of one-sided surface structures against a generic flat surface ³. There are few studies on adhesion selectivity by surfaces with complementary architectures despite the fact that there are plenty of perfectly matched or complementary surfaces in nature. For example, insects use interlocking hard claws to attach to a wide variety of substrates ^{1, 21}. An interlocking meso-scale structure is responsible for attachments in the dragonfly head-arresting system ²². At the much smaller length scale of intermolecular associations, it is well-known that two nucleotides on opposite complementary DNA or RNA strands are connected via hydrogen bonds ²³;

formation of protein-protein complexes is based on shape complementarity²⁴. Selectivity in adhesion can be achieved by surface chemistry²⁵⁻²⁸, including a study about surface pattern recognition using hydrophobic complementarity²⁹. A celebrated example of achieving adhesion using mechanical complementary is Velcro[®]³⁰ which uses a loop-clasp mechanism. Recently, Vajpayee *et al*³¹ showed that highly selective adhesion can be achieved between complementary elastic surfaces patterned with ripples. The increase in adhesion in this case is due to a crack-trapping mechanism.

In this work, we investigate the adhesion of micro-channel structured periodic surfaces with different channel depths and inter-channel spacing. Leger and co-workers¹⁶ and Shahsavan & Zhao¹⁷ have recently shown that complementary structured surfaces have strongly enhanced adhesion. However, their studies were on the *first* separation of an as-molded shape-complementary interface. Here we pursue a somewhat different investigation; we ask: if patterned substrates are separated and then pressed into contact, will complementary shapes inter-penetrate sufficiently and with high recognition/selectivity? We find that adhesion, as determined by the energy release rate required to propagate an interface crack, can be highly enhanced when surfaces are complementary, but only for restricted ranges of geometrical parameters such as inter-channel spacing and channel depth. On the other hand, adhesion can be highly attenuated for mismatched samples, indicating that micro-channel/pillar structured interfaces can be used to achieve highly selective adhesion. Controlling adhesion and selectivity by structure provides a handle on this surface mechanical property that can be manipulated independently of

surface chemistry. It has a variety of potential applications including fasteners, moving small objects, and as bandages or adhesives in biomedical applications.

We also observe an interesting phenomenon in complementary samples: the appearance of defects in the form of visible striations. These defects are similar to atomic-scale dislocations in crystalline materials, for example metals. However, unlike metals, where dislocations cause plastic deformation that is responsible for their high toughness, our experiments indicate that while their presence accommodates orientational mismatch between the two surfaces, overall it is detrimental to adhesion. We have also carried out a preliminary analysis to explore some of the properties of these defects and to understand how geometrical parameters affect adhesion.

3.2 Experimental methods

3.2.1 Sample fabrication

The fabrication process is illustrated schematically in Figure 3.1. We began by molding an elastomer, poly (dimethylsiloxane) (PDMS), into etched silicon masters (with parallel micro-channels on the surface) patterned by photolithography. The channel width of the original masters was fixed at 10 μm , channel depth, d , was varied (10, 20, and 30 μm), and minimum center-to-center spacing or smallest period, c , was varied in the range 20-125 μm . Molding was done by mixing liquid PDMS precursor (silicone elastomer base), with curing agent (Sylgard 184, Dow Corning) in weight ratio of 10:1. The liquid silicone mixture was degassed under vacuum for 30 minutes before applying to the master and was cured at a temperature of 80°C for 2 hours.

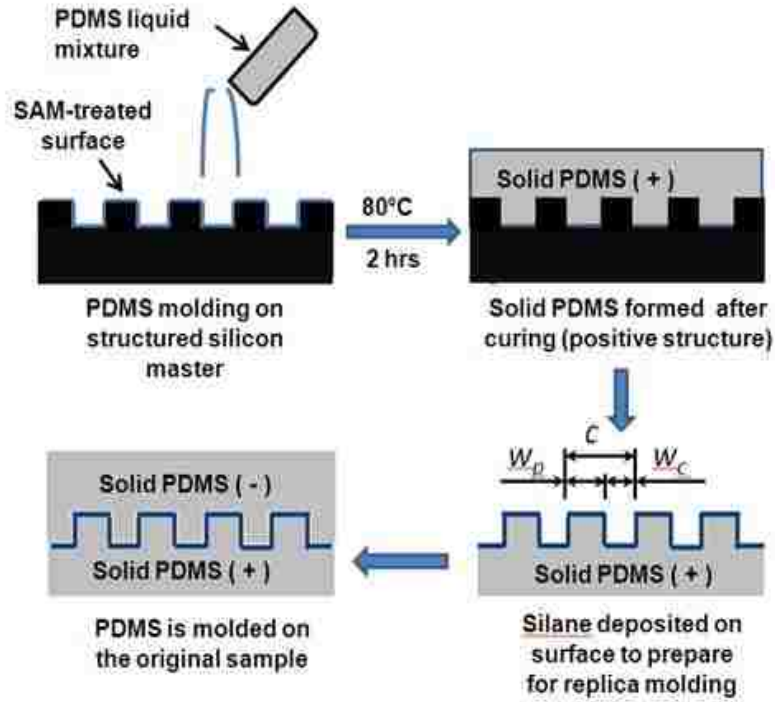


Figure 3.1 Schematic illustration of the sample fabrication process. The positive replica is called the pillar side and the negative replica is called the channel side.

After curing, we peel the solid PDMS replica off the silicon master. Samples have pillar and channel widths $w_p^+ = 10\mu m$, w_c^+ , and interchannel spacing $c = w_p^+ + w_c^+$. The positive replica is called the pillar side since the pillar width is fixed at $10\mu m$. A second set of PDMS samples complementary to the first set was fabricated by the following replica molding process. The original PDMS samples were coated by a monolayer of n-Hexadecyltrichlorosilane ($C_{16}H_{33}Cl_3Si$). Samples with a complementary surface profile were obtained by a second molding and curing of PDMS on this first set of PDMS samples with pillar and channel widths $w_p^- = w_c^+$; $w_c^- = w_p^+ = 10\mu m$. The negative replica is called the channel side since the channel width is fixed at $10\mu m$. A typical sample is

635 μm thick, 30 mm long and 10 mm wide. Figure 3.2 shows scanning electron microscope (SEM) images of a pair of complementary samples with 35 μm center-to-center spacing, c .

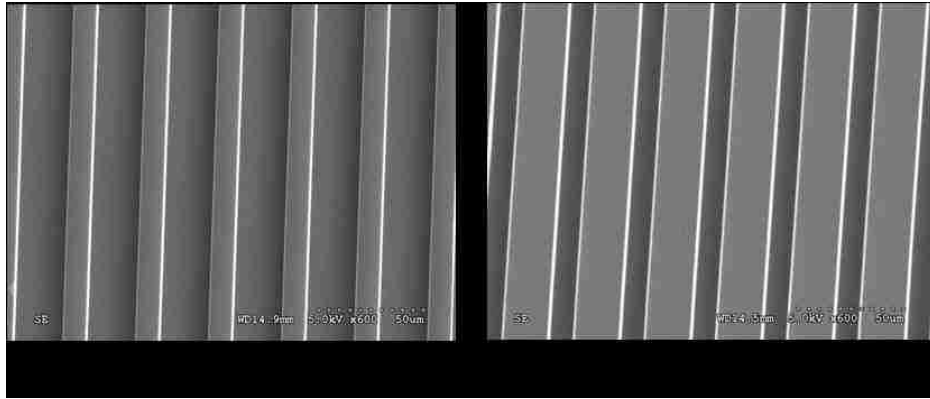
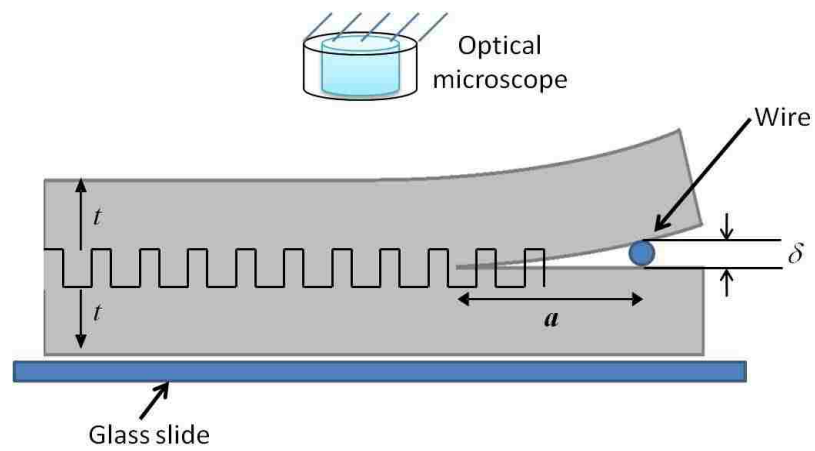


Figure 3.2 SEM images of a pair of complementary surfaces with interchannel spacing $c = 35 \mu\text{m}$. (a) pillar-side with pillar width of 10 μm , (b) channel side with channel width of 10 μm .

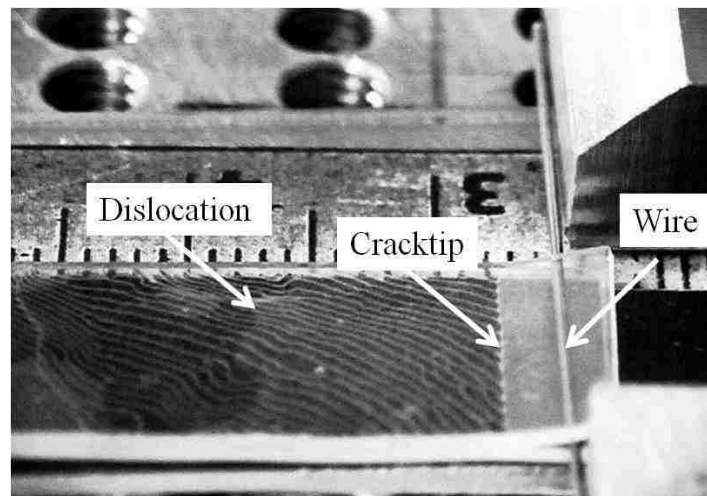
3.2.2 Adhesion testing

We begin by separating the pillar and channel sides samples obtained after the replica molding step (Figure 3.1). We then press two sheets against each other by hand, attempting to force pillars on one sheet to find and insert into the channels of the other. We found that the flexibility of the sheet was necessary for pillars to insert into channels with a minimal number of defects. For example, mounting just one of the two sheets on a glass slide or cover slip made the sample too stiff to allow protrusions to reproducibly find complementary grooves. We measured the adhesion of the resulting sandwich structure in the following manner (Figure 3.3). One sheet of the sandwich sample was placed on a glass slide and a wire of known diameter (typically either 0.49 or 0.65 mm) was placed along the micro-channel/pillar interface a fixed distance (~ 2.0 mm) from the

edge of the sample. The sample was then moved towards the wire and stopped. The wire serves as a wedge, applying an opening displacement approximately equal to its diameter. As a result a crack propagates away from the wire (Figure 3.3b), eventually arresting at an equilibrium length. We also carried out control experiments on flat, unstructured, samples of the same thickness. For flat samples we waited for at least one hour for the crack to achieve its equilibrium position; for structured samples we found thirty minutes to be sufficient. In the structured samples we always observed the formation of striations (Figure 3.3b) separating transparent regions where pillars were fully inserted into channels. As discussed in detail later, these striations are defects that allow pillars to find channels while accommodating relative shear and rotation between the two sheets.



(a)



(b)

Figure 3.3 (a) Schematic illustration of the experimental set-up for measuring adhesion energy. (b) Photograph of the experimental set-up showing the wire that serves as a wedge opening a crack. Also visible are a series of striations – these defects, which are similar to dislocations in crystalline materials, accommodate relative shear and rotation between the two PDMS strips while permitting alignment between the pillar and channels in regions between the defects.

3.2.3 Relating crack length to energy release rate

The equilibrium crack length results from a balance between energy release rate supplied by the wedged portion of the PDMS strip and the energy required to increase the crack area by a unit amount. If the crack length a is long compared to the strip thickness, t , the energy release comes primarily from the wedged-open upper strip. If the strip is modeled as a linearly elastic beam wedged open by a displacement equal to the diameter of the wire, δ , we obtain the well-known relationship between energy release rate, G , and crack length, a : ^{31, 32}

$$G = \frac{3E^* \delta^2 t^2}{8a^4} \quad (3.1)$$

where t is the thickness of the upper strip and E^* is its plane strain modulus. However, in our experiments, the crack length is comparable to the film thickness, so we conducted separate finite element calculations (using the commercial finite element package, ABAQUS[®], version 6.9) to relate the measured crack length to energy release rate over the entire experimental range of crack lengths, extending a similar analysis described previously ³¹.

3.3 Results and discussion

3.3.1 Defects accommodate relative shear and rotation between strips

For complementary samples, since we took no special care to align the two PDMS strips, the first question is whether pillars will insert into their complementary channels. Stated another way, one can ask whether and how the two strips will accommodate the

necessarily present misalignment. In Ref. (31), we studied adhesion selectivity and enhancement based on shape complementarity using rippled surfaces. There we reported that complementary rippled surfaces with moderate amplitudes (amplitude/wavelength ≤ 0.2) can readily be pressed into nearly perfect contact with no visible defects. In sharp contrast, for the photolithographically fabricated channel/pillar structures studied in this work (with much higher aspect ratios), we invariably observe defects in the form of visible striations tens to hundreds of microns in width and separated by distances on the order of millimeters.

Figure 3.4 (a-c) show three complementary samples with pillar-side pillar width of $10 \mu\text{m}$ and varying spacing, c . In each case, these low-magnification micrographs have clear, featureless regions where pillars have been inserted fully into channels. In addition there are white-ish, light-scattering, striations. These striations become wider as the inter-channel spacing, c , increases, occupying most of the interfacial area for larger spacings. We observe that striations can form with different orientations with respect to the pillar/channel direction. In addition, they either end on the sample boundaries (Figure 3.4b) or form internal loops (Figure 3.4a).

To understand the nature of these striations, consider Figures 3.4 (d,e), which shows a complementary sample with $c = 20 \mu\text{m}$. Figures 3.4d and 3.4e show two magnified views of a striation that runs approximately perpendicular to the channel direction. Figure 3.4d shows that the striation has a characteristic width comprising of two regions: an inner core with an outer region on either side of the core. Away from the striation are featureless regions where the pillars are fully inserted into the channels. The

vertical lines making up the striation are pillar/channel combinations that are no longer fully inserted, i.e., the striation is visible because of light scattering from interfacial regions in partial contact. A close examination (Figure 3.4e) reveals that in the core region pillars are extracted from their complementary channel and shifted over by one period (a distance, c) and partial inserted into another complementary channel. Because of the complementary and symmetric nature of the two PDMS sheets, each such shift in one sheet is mirrored by an equal and opposite shift in its complementary sheet. We have observed that these shifts *always* have a magnitude equal to one periodic spacing, i.e., when a pillar is forced out of its channel, it shifts over exactly one periodic spacing c to find a new channel into which to insert itself. In the last section, we show that the striations in Figure 3.4 can be viewed as “screw dislocations” that carry a Burgers vector of magnitude c aligned orthogonal to the channel direction in the plane of the sheet.

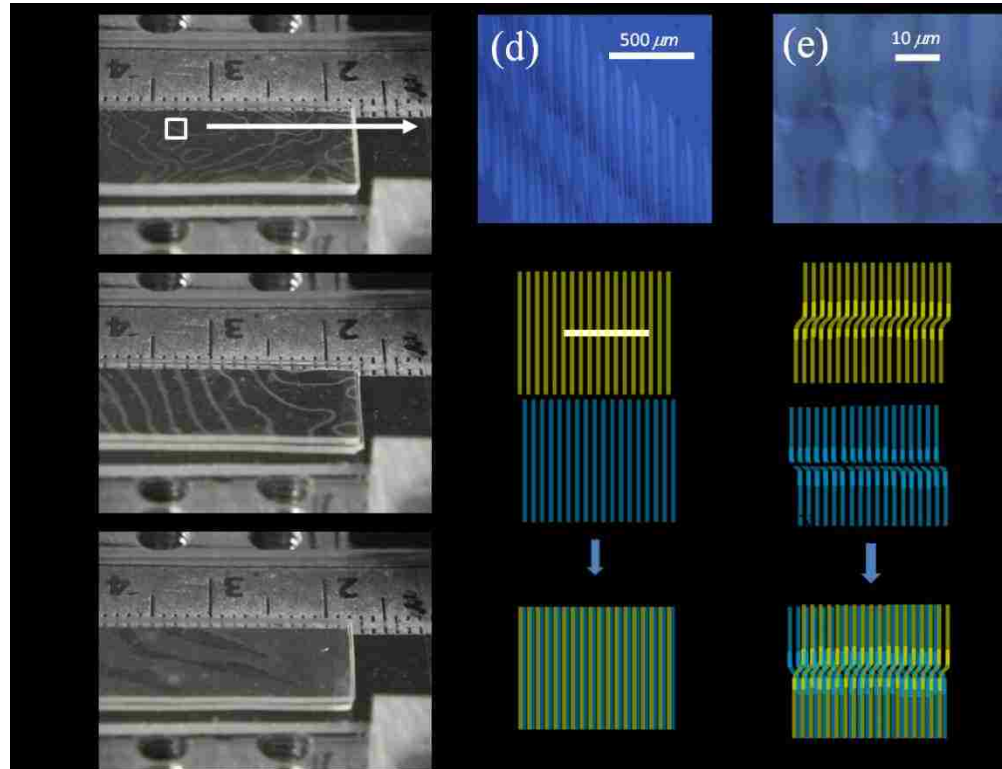


Figure 3.4 Micrographs of defects in micro-channel complementary surfaces. All three samples shown above have the same channel depth and width, $d = w_p = 10 \mu\text{m}$. Channel spacings c are (a) $20 \mu\text{m}$. (b) $35 \mu\text{m}$. (c) $110 \mu\text{m}$. In each case, the low-magnification micrographs on the left column (a-c) provide a macroscopic view of the sample. Clear, featureless regions are those where pillars have been inserted fully into channels. Note the appearance of white-ish, light-scattering, striations. (d) These striations are regions where pillars fail to fully insert into channels. The striations have an inner core region (e), where a pillar switches from one channel to another, and an outer region where the pillars are debonded and partially removed from the channel. (f) Two defect-free pillar-channel pairs (colored strips represent pillars) insert into each other. (g) Striations are screw dislocations with Burgers vector of magnitude c with orientation normal to the channel direction.

3.3.2 Adhesion measurements of complementary interfaces ^g

Figure 3.3 showed how a crack advances between two sheets due to the wedging action of a wire inserted between the two. Figure 3.5 shows the crack front as it runs in a well-adhered region. Figure 3.5a shows a sequence of three micrographs from a flat control sample. Figure 3.5b shows a complementary pillar/channel interface. We observe from Figure 3.5b that

a) There are two distinct fronts, one where the pillars have debonded or partially extracted from their complementary channels, and a second one behind it where the pillars are fully extracted from their channels. Typically, as in these micrographs, there are 2-3 channels between first and the second front.

b) The debonded front advances by nucleating small debonded segments along the overall direction of crack growth (horizontal in Figure 3.5). These segments then grow orthogonal to the crack growth direction (vertically in Figure 3.5). The crack front grows in a similar manner, following the debonding front.

^g The adhesion measurements of *complementary* micro-channel surfaces were mostly done by Dr. Arun K. Singh, when he worked at Lehigh University as a postdoctoral research associate.

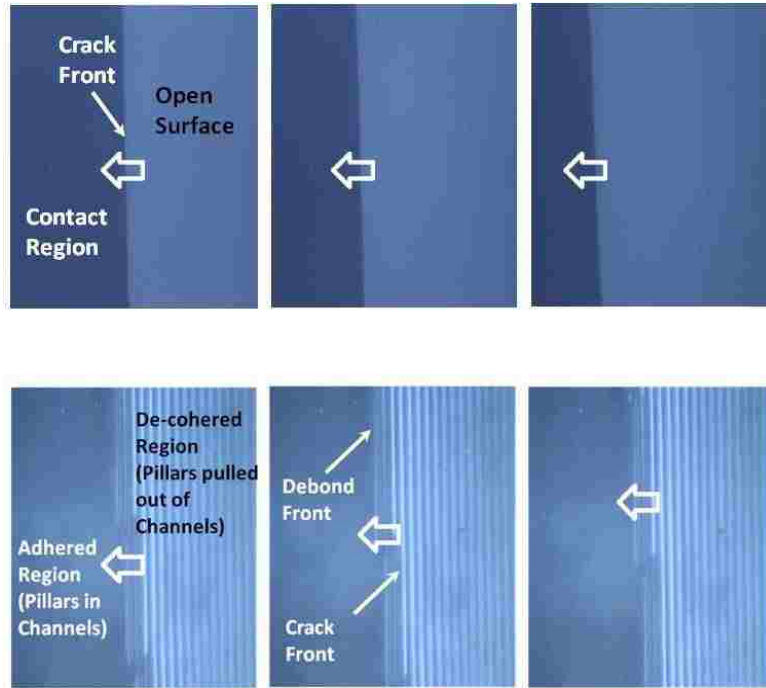


Figure 3.5 Optical micrographs of the region behind and ahead of the crack front. (a) the growth of a crack at the interface between two flat surfaces. (b) A complementary micro-channel sample ($d = c = 20 \mu\text{m}$) showing a crack advancing through a well-adhered region of the interface.

As explained in the experimental section, we measure the equilibrium crack length and then convert this measurement into effective interfacial adhesion energy using either Eq. (3.1) or our finite element calculation, depending on the crack length. Figure 3.6 plots the energy release rate required for interfacial opening normalized by its value for a flat control. For each set of samples, we made 10 measurements (error bars represent standard deviation). Half of these measurements were performed with one of the complementary sheets on the glass slide and the rest were performed with the other complementary sheet on the glass slide. We found no significant dependence on whether

the pillar or channel side was wedged open. The first striking observation is that one can achieve a sizable enhancement of adhesion, up to a factor of forty, over the flat control (represented by the horizontal line in the figure) in these complementary structures. Secondly, we note that, except for one sample ($d = 30\mu\text{m}$), the effective adhesion decreases monotonically as inter-channel spacing increases. Eventually, the effective work of adhesion decreases with increasing inter-channel spacing to a value lower than that of the flat control.

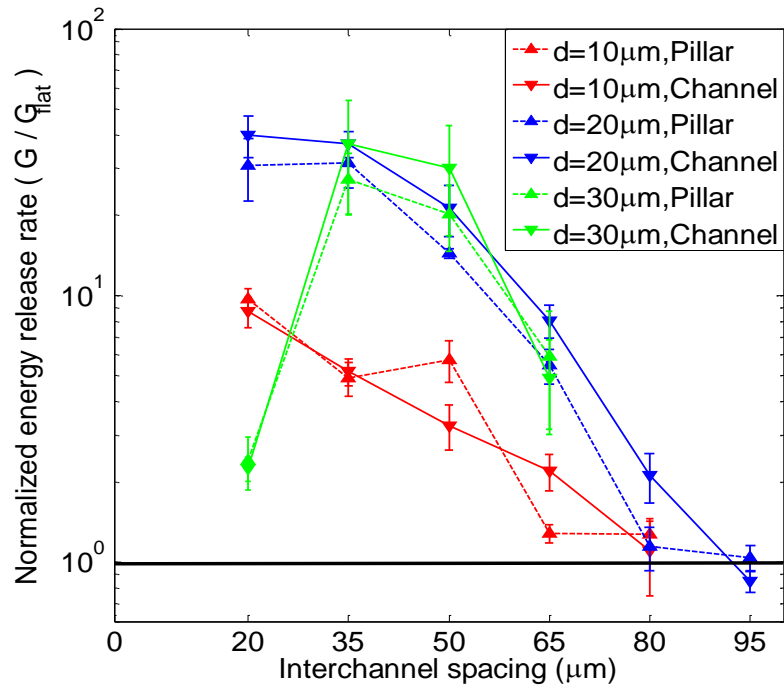


Figure 3.6 Normalized energy release rate required to open the interface for different interchannel spacing, and three different channel depths (10, 20 and 30 μm).

The exceptional case of 30 μm deep channels is interesting. Figure 3.6 shows that the adhesion energies of these samples with 20 μm spacing are much lower than those of samples with spacing of 35 μm . Figure 3.7 shows low magnification images of these two samples. We find that in the case of 20 μm spacing nearly the entire sample scatters light, which appears to be because channels are tall enough to adhere to their neighbors. The sample with 20 μm spacing shows the more normal regions of good contact with striations that accommodate relative misorientation.

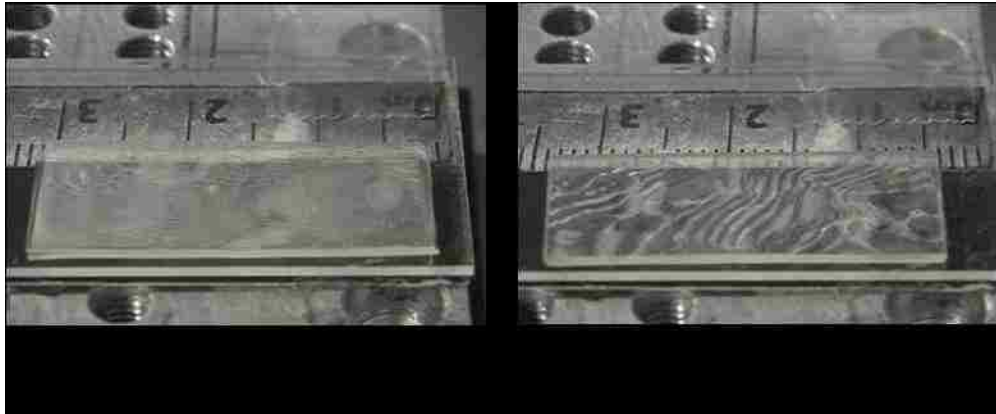


Figure 3.7 Low magnification pictures of complementary samples with channel depth $d = 30 \mu\text{m}$. (A: inter-channel spacing $c = 20 \mu\text{m}$, B: $c = 35 \mu\text{m}$)

3.3.3 Adhesion measurements of non-complementary interfaces

The results of the previous section have established the fact that, with properly chosen dimensions, complementary pillar/channel samples can strongly enhance adhesion between two surfaces compared to a flat control. We now ask whether and how strongly adhesion can be modulated by making the structures non-complementary. We studied two sets of samples. In both sets, the width of the channels and pillars on one

side of the sample was the same (10 μm , top sheet in Figures 3.8b, c). In one set, the other side of the sample was a pillar side where the pillar width was fixed at 10 μm (bottom sheet, Figure 3.8b). In the second set, the other side of the sample was a channel side where the channel width was fixed at 10 μm (bottom sheet, Figure 3.8c). We can see that if c_p is a multiple of $c_c=20 \mu\text{m}$, then the pillar side is expected to ‘recognize’ the channel side. However, if this is not the case, then only occasionally will the pillar side ‘find’ the channel side. We can see that this is indeed the case in Figure 3.8a, the ‘blue’ set of samples. On the other hand, if we fix the periodic spacing of the pillar side to be 20 μm and vary the periodic spacing of the channel side, then except for the case where the two periods are identical, the surfaces do not adhere well to each other at all. This is shown in Figure 3.8a by the ‘red’ set of samples. Together these two results demonstrate strongly selective, shape-recognition based, adhesion between these samples.

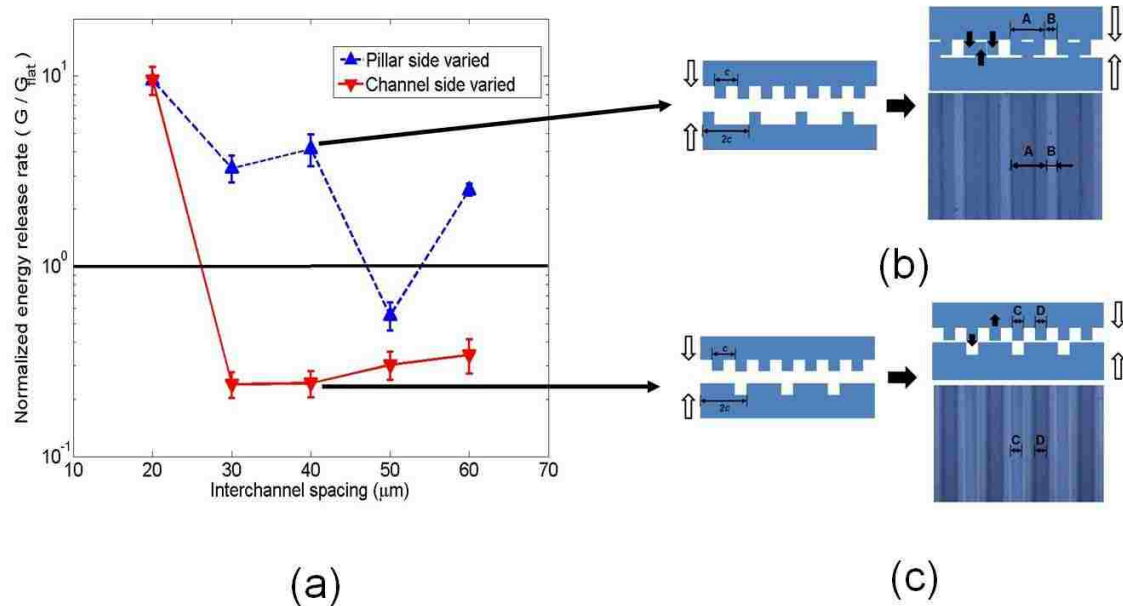


Figure 3.8 (a) Normalized energy release rate versus periodic spacing of the bottom sheet for non-complementary interfaces. The channel depth of both sheets is $10\ \mu\text{m}$. The top sheet has identical pillar and channel width ($10\ \mu\text{m}$). The pillar width in the bottom sheet of the first set (blue) is fixed at $10\ \mu\text{m}$ and the interchannel spacing is varied (pillar side). In the second set (red), the channel width in the bottom sheet is fixed at $10\ \mu\text{m}$ with varying spacing (channel side). (b) shows an optical micrograph for channel width of $30\ \mu\text{m}$. In region A, the pillars in the bottom sheet are fully inserted into the channel of the top sheet. In region B, there is a $10\ \mu\text{m}$ gap where there is no contact. For this case adhesion is somewhat attenuated compared to a perfectly complementary case with interchannel spacing of $40\ \mu\text{m}$ (see Figure 3.6). (c) shows an optical micrograph with pillar width of $30\ \mu\text{m}$. In Region C, the pillars are in line with the channels but cannot insert into them because of region D, where the $10\ \mu\text{m}$ pillars are in contact with the $30\ \mu\text{m}$ pillars in the bottom sheet. For this case, it is clear that there is no insertion and only 25 percent of the interface is in contact. This fact is consistent with the measurement effective work of adhesion (see (a)), which decreases by 75% compared to the flat control.

3.4 Mechanisms of adhesion modulation for complementary interfaces

We identify three mechanisms that control adhesion of complementary surfaces. Two of these mechanisms (crack trapping and friction pull-out) enhance adhesion, while the third (energy release by misfit dislocations) is detrimental to it.

3.4.1 Crack-trapping

In a previous work on complementary rippled surfaces, we have shown that adhesion enhancement is due to a crack trapping mechanism.³¹ Since the channel/pillar architecture can be considered as a special case of these rippled surfaces, we can use the theory developed in Ref. (31) to estimate the adhesion enhancement associated with this mechanism. The basic idea behind crack trapping is that the energy release rate varies with the spatial position of the crack front, which is a periodic function for our geometry. For a homogeneous interface with a constant work of adhesion, the crack is trapped at the position where the energy release rate is a minimum.³¹ At this position, when the external load increases enough to grow the crack, it extends dynamically and unstably, arresting just before the next energy minimum. This intermittent unstable process results in significant loss of stored elastic energy which accounts for the increase in the effective work of adhesion.

A simple model which captures the essence of crack trapping for our channel/pillar samples is shown schematically in Figure 3.9. The geometry consists of two complementary thin sheets of PDMS (plane stress) with lateral dimensions much larger than the channel depth and width. A long crack occupies half of the interface.

For the time being, we assume that the interface directly ahead of the crack is defect free: that is, all the pillars in this region are fully inserted into their complementary channels. In addition, the interface between the pillars and channels is frictionless. A uniform vertical displacement Δ is applied on the top of the upper sheet and the lower sheet is fixed.

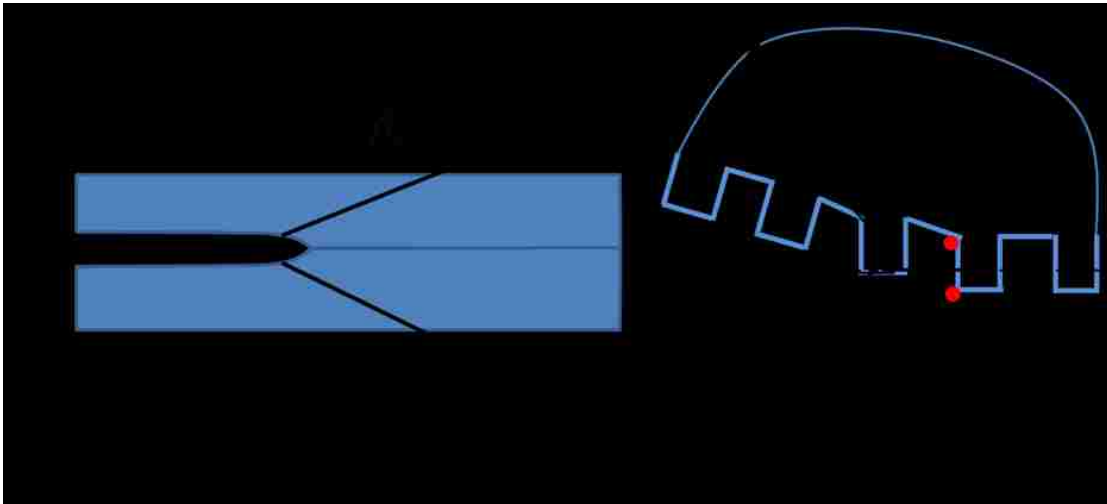


Figure 3.9 Schematic diagram showing directions of crack propagation along both the flat interface and the structured interface.

The essence of the argument is that the when the crack moves in a direction other than horizontal, the available energy release is lower. According to our previous work ³¹ when the crack is forced to move orthogonal to the horizontal direction, the energy release rate is reduced by a factor

$$G_{\min} = \cos^4(\pi/4) \tag{3.2a}$$

The enhancement factor for the effective work of adhesion is the inverse of G_{min} , which is

$$\omega_{CT} = \frac{1}{\cos^4\left(\frac{\pi}{4}\right)} = 4 \quad (3.2b)$$

It should be noted that Eq. (3.2a) assumes that the slope of the interface is nearly flat, a condition which is clearly violated since the channel walls are vertical. Indeed, due to this discontinuity, the position of minimum energy release cannot be precisely located using our previous theory – it can occur anywhere between a and b in Figure 3.9. To check the accuracy of Eq. (3.2a), we determine the energy release rate using a plane stress finite element method (FEM) (Figure 3.10) in ABAQUS®. ³² The interface geometry is shown in Figure 3.10 where the debonded region consists of four pillar/channel pairs. This assumption is consistent with our experimental observation that there are 2-3 channels between the debond and the crack front. In our FEM, the two sides of the channel/pillar interface are defined as frictionless contact pairs. A “tie” constraint is imposed on the nodes along this interface. We extend the crack along the structured interface by releasing selected nodes at this interface from the “tie” constraints. The energy release rate is determined by evaluating the *J-integral* ³¹ around the crack tip in ABAQUS® and also by direct evaluation of the change in total strain energy of the system due to incremental crack advance; Figure 3.10 shows the results based on change in total strain energy. Calculations are performed for two different models. In model (a), the channel depth is the same as the channel width. In model (b), the channel depth is double the channel width.

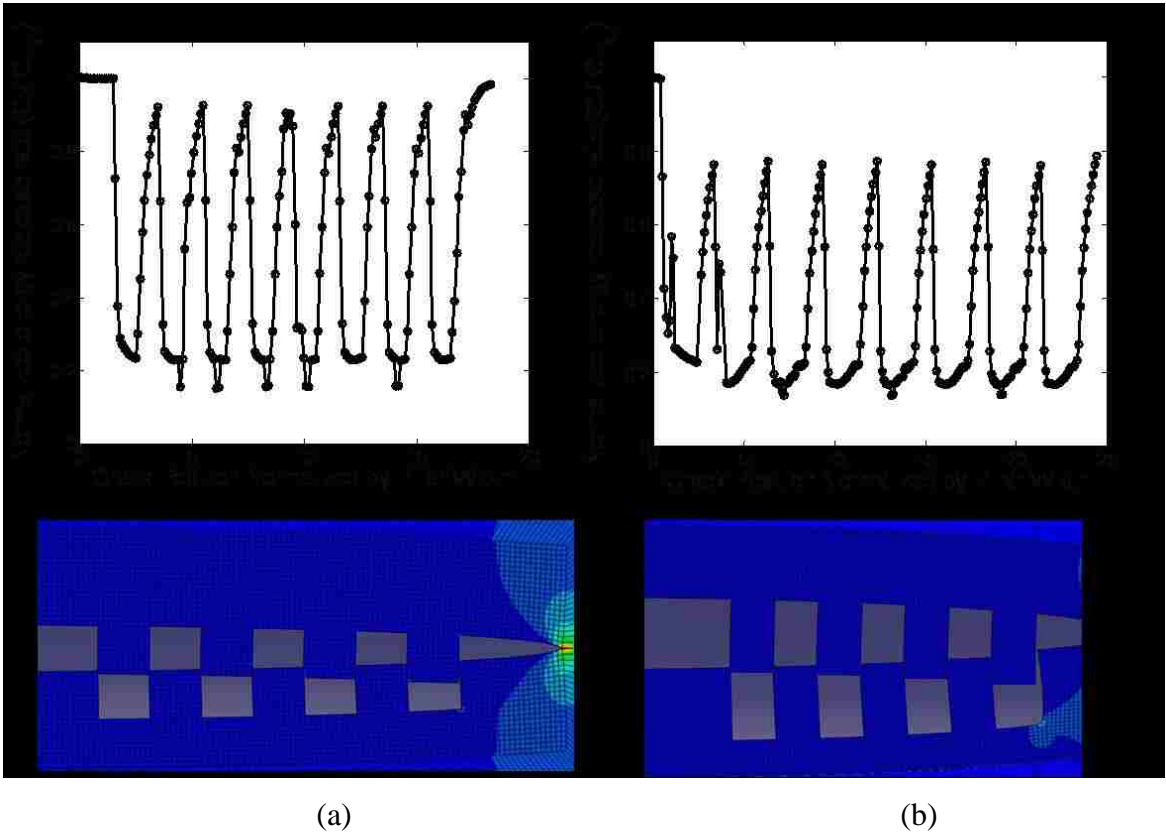


Figure 3.10 Finite element model of crack-trapping mechanism for two different channel depths, (a) channel depth = channel width. (b) channel depth = $2 \times$ channel width.

Figure 3.10 shows that the energy release rate varies periodically along the micro-channel/pillar structured interface. The adhesion is enhanced by about five times for two different channel depths and the structure with larger channel depth (Figure 3.10b) has a slightly greater enhancement. (The actual enhancement will be somewhat larger because of mode-mixity.³¹) Thus, the approximate expression Eq. (3.2), which indicates that the energy release rate is independent of channel depth and width, agrees reasonably well with our finite element results. However, the experimental results in Figure 3.6 show that the enhancement in the effective work of adhesion is about forty times for complementary samples with 20 μm depth and 20 μm spacing. Moreover, the predicted energy enhancement due to crack trapping is about the same for the two different depths in Figure 3.10 while the experiments indicate otherwise – the 20 μm deep sample (Figure 3.10b) is found to be 4 times tougher than the 10 μm deep sample (Figure 3.10a). This comparison between experimental results and finite element analysis reveals that the crack-trapping mechanism could not solely be responsible for adhesion enhancement. This brings up the second mechanism for adhesion enhancement: friction between the pillars and the channels.

3.4.2 Effect of friction

To estimate the energy release rate due to friction between a pillar and its complementary channel groove, we assume a constant friction stress τ along both sides-of the pillar/channel interface. This assumption is consistent with experimental results by Chaudhury *et al*^{33,34} and Chateauminois *et al*³⁵, who demonstrated that the sliding

friction stress between two PDMS surfaces is a material constant for a reasonably wide range of sliding rates. To estimate the energy release rate contribution due to friction, it is sufficient to compute the energy required to completely pull the pillars off a unit area of a complementary surface.

Let u denote the amount of pull-off and F be the force acting on one end of the pillar (see Figure 3.9). To simplify the analysis, we ignore the elastic energy due to stretching of the pillar. For this case, simple force balance shows that F is related to u by

$$F = \tau(d - u)b \quad (3.3)$$

where b is the out-of-plane thickness of the pillar. The energy required to fully extract a pillar from its complementary channel is

$$W = 2 \int_0^d F du = \tau d^2 b \quad (3.4)$$

Since the number of channel per unit area is $1/bc$, the energy release rate due to friction pull-out is

$$G_f = \frac{W}{cb} = \frac{\tau d^2}{c} \quad (3.5)$$

Note that the contribution to the energy release rate due to friction is inversely proportional to the interchannel spacing and increases as the square of the channel depth. Also, since we neglected the elastic energy due to stretching of the pillars, the energy release rate given by Eq. (3.5) is a lower estimate since not all of the stretching energy can be recovered during the pull-off process. Using results of Chateauminois³⁵ for an approximate value of $\tau = 0.15 \text{ MPa}$ and $d = c = 20 \mu\text{m}$, $G_f \approx 3 \text{ J/m}^2$. This estimate of frictional energy release rate should be compared to the typical work of separation for flat

PDMS samples, about $200 \text{ mJ/sq. m}^{36}$. That is, friction between pillar and channel can enhance energy release rate by a factor of fifteen, which is significantly greater than the factor of five due to crack-trapping (as shown in the previous section). Furthermore, for fixed inter-channel spacing $c = 20 \mu\text{m}$, we can see that the energy release rate for $d = 20 \mu\text{m}$ is about four times that for smaller depth, $d = 10 \mu\text{m}$, consistent with the quadratic dependence of energy release rate on d predicted by Eq. (3.5). We therefore conclude that the friction makes a major contribution to the work of separating the interface, albeit the crack trapping mechanism also plays a significant role. More detailed analysis combining both these mechanisms will be needed to better model the separation process.

3.4.3 Energy release by misfit dislocations

The micrographs in Figure 3.4 strongly suggest that defects due to misfit can dramatically reduce the effective work of adhesion. Figure 3.11 shows that the fraction of interface area covered by defects in a sample with $10 \mu\text{m}$ channel depth is approximately proportional to the interchannel spacing. This result is consistent with Figure 3.6 which shows that the effective work of adhesion decreases with increasing interchannel spacing. To quantify the detrimental effect of these defects, it is necessary to understand the deformation and energy associated with these defects.

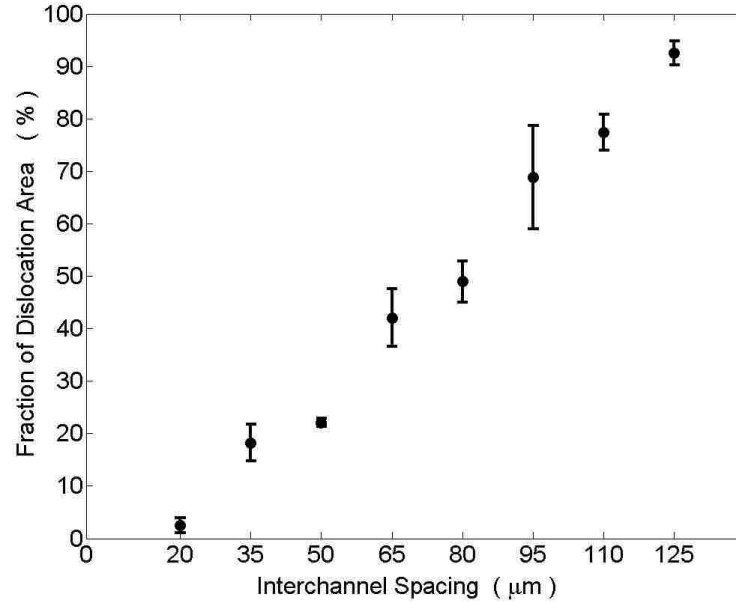


Figure 3.11 Fraction of dislocation area in a series of complementary samples with depth $d = 10 \mu\text{m}$ and variable interchannel spacing, c .

Many features of classical continuum dislocation theory can be used to describe the mismatch defects observed in our experiments. To define a dislocation, imagine two complementary surfaces that fit perfectly and let D denote a simply connected planar region on this interface. Without loss in generality, we assume that the interface is part of the x-y plane ($z = 0$) and that the channels are parallel to the y axis. Let C denote the boundary curve of D . Ascribe a positive sense of direction to C by requiring it to encircle the outward normal vector \vec{k} of D consistent with the right-hand rule. A dislocation is created by the following process: make a cut on the surface D , and denote the upper (lower) surface resulting from the cut by D^+ (D^-). The normal vector to D^+ is in the

same direction as \vec{k} whereas the opposite holds for D^- . Next, translate D^- relative to D^+ by the vector $\vec{b} = n\vec{i} + b_2\vec{j} + b_3\vec{k}$, where n is an integer, b_2 and b_3 can be any small real numbers. In our experiments, $n = \pm 1$. The vector \vec{b} is defined as the *Burgers vector*. The curve C is called the dislocation line. If C is a closed curve, it is called a dislocation loop. When \vec{b} is in the same direction as the curve C or the dislocation line, the dislocation is called a screw dislocation. When \vec{b} is perpendicular to C , the dislocation is called an edge dislocation. Since C is a curve, in general \vec{b} is neither parallel nor perpendicular to C , and the dislocation is called a mixed dislocation.

A simple example of a screw dislocation is illustrated in Figures 3.4 (f,g). Here D is the half plane defined by $|x| < \infty, y > 0, z = 0$. The dislocation in Figure 3.4 is obtained by translating D^- to the right and D^+ to the left by $c/2$, respectively. The dislocation line is along the x axis and its direction is \vec{i} . The Burgers vector in Figure 3.4 is $\vec{b} = c\vec{i}$ and is parallel to the dislocation line. (Since there are two equivalent sheets, the Burgers vector is equal and opposite in the other sheet.) Note that far away from the dislocation line the channels fit perfectly. Near the dislocation line, the sheets do not fit perfectly. In Figure 3.4g, this region of misfit is an infinite long cylinder with radius R_c in the x direction. This region is called the dislocation core. The deformation in this region was described earlier (see also Figure 3.4). From our description, it is clear that the core is dilated. The core consists of a center region where the pillars are completely pulled-out and sheared sideways by a distance c ; away from the core's center the pillars are partially extracted from the channels. The complex deformation inside the

dislocation core will be addressed in a future work. Here we will present a simple analysis of the stress and strain fields outside the core region for samples with thick backing layers, where $t \gg c$.

If the backing layers are very thick in comparison to c , they can be modeled as infinite elastic blocks. The stress and strain fields far away from the core region are independent of x can be readily obtained using continuum theory³⁷. With respect to a polar cylindrical coordinate system (r, θ, x) , i.e.,

$$r = \sqrt{y^2 + z^2}, 0 \leq \theta \leq 2\pi, \quad (3.6)$$

the displacement fields are:

$$u_1 = \frac{c}{2} - \frac{c\theta}{2\pi}, u_2 = u_3 = 0 \quad 0 \leq \theta \leq 2\pi \quad (3.7)$$

The non-trivial stresses induced at distances $r \gg R_c$ are given by:

$$\sigma_{13} = -\frac{Gc}{2\pi r} \cos \theta, \quad \sigma_{12} = \frac{Gc}{2\pi r} \sin \theta \quad (3.8a)$$

The associated strains are:

$$\varepsilon_{13} = -\frac{c}{2\pi r} \cos \theta, \quad \varepsilon_{12} = \frac{c}{2\pi r} \sin \theta \quad (3.8b)$$

This solution is, of course, not valid near the core region, as evident by the fact that the stresses become infinite as $r \rightarrow 0$. As one approaches the core, higher order correction terms must be included in the stress field. These terms depend on the internal structure of the core and are beyond the scope of this chapter. The divergence of the stresses implies that the strain energy is unbounded. Indeed, a straightforward

calculation shows the strain energy stored per unit length Γ of the dislocation line in a region bounded by cylinders of radius $R_c < R_o$ is

$$\Gamma = \frac{Gc^2}{4\pi} \ln \frac{R_o}{R_c} \quad (3.9)$$

where G is the shear modulus of PDMS. Note that the strain energy per unit length Γ is proportional to the square of interchannel spacing and diverges as $R_o \rightarrow \infty$. This divergence is due to the two dimensional artifact of our problem; the misfit energy depends on the size of the specimen. To obtain a realistic energy for the dislocation, it is necessary to include the misfit energy of the pillars inside the core and to obtain an estimate of the width of the dislocation or the core size, problems are discussed in Ref. (38).

Our analysis above indicates that a lower bound for the elastic energy of a misfit dislocation is given by Eq. (3.9). Since we do not observe formation of new dislocations in our adhesion experiments, these dislocations cannot dissipate energy; rather, the elastic energy associated with them can be released to assist instead of retarding crack growth. Estimate R_o to be the sample width, 1.27 mm, and R_c to be characteristic core size, $\sim c$, in the range 20-100 μm . Then Eq. (3.9) is approximately,

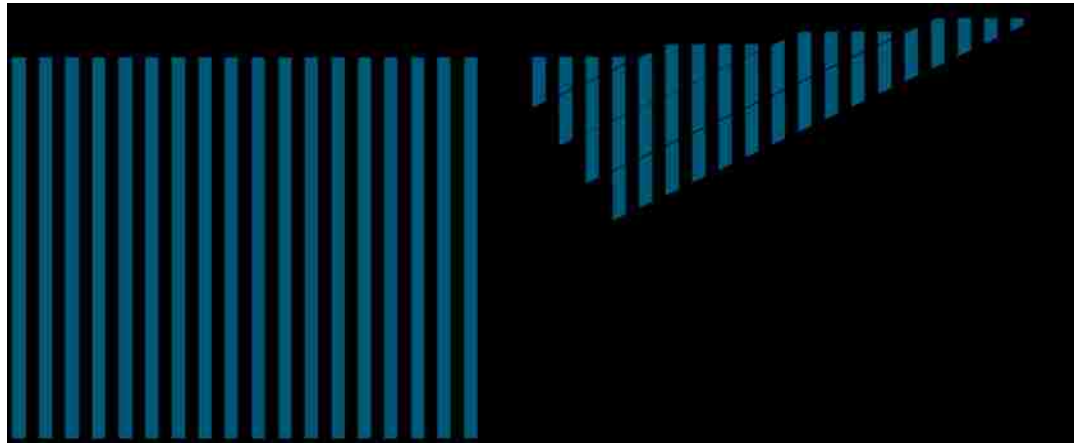
$$\Gamma \approx Gc^2 / 2 \quad (3.10)$$

If we assume that all the elastic energy associated with these dislocations are released to assist crack growth, then a rough estimate of the negative contribution to the energy release rate is

$$G_d \approx \rho\Gamma = \rho Gc^2 / 2 \quad (3.11)$$

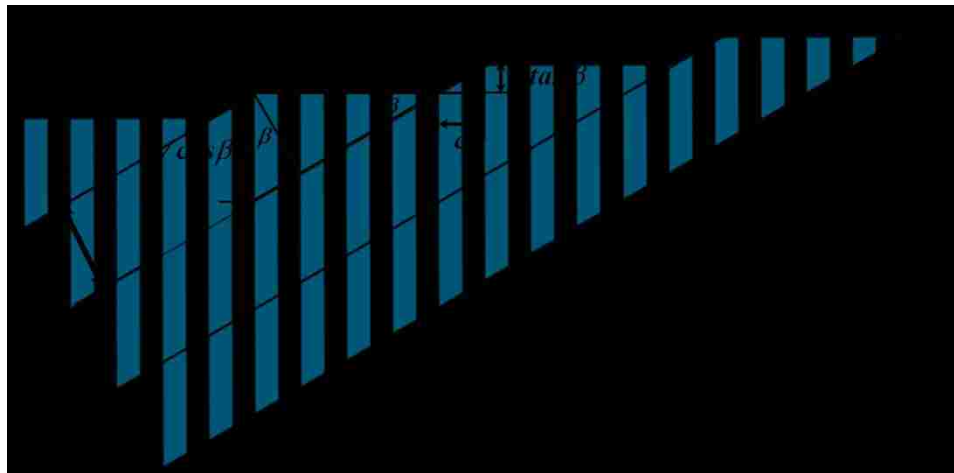
where ρ is the number of dislocation lines per unit length. The fact that Γ is proportional to the square of the inter-channel spacing supports our observation that the effective work of adhesion decreases with c .

Just as in polycrystalline metals, where the areas swept by dislocation lines create plastic strains, mismatch dislocations in complementary surfaces can accommodate elastic deformation. (In metals at room temperature dislocations glide on slip planes. A poly-crystal has many slip planes oriented in different directions. For our system there is only one slip plane which is the interface formed by the complementary surfaces.) A simple example is shown in Figure 3.12a which shows one undeformed sheet with vertical pillars and channels. Figure 3.12b shows part of the sheet drawn in Figure 3.12a but additionally with a set of parallel dislocations; this figure has been annotated with angles and distances in Figure 3.12c. (Note that the dislocation lines drawn in Figures 3.12c and 3.12d do not cut through the sample. Rather, they represent the core at the interface.)



(a)

(b)



(c)

Figure 3.12 Schematic diagram showing how dislocations accommodate shear and rotation.

The Burgers vector for each inclined dislocation drawn in Figure 3.12c is

$$b = c\vec{i} + c \tan \beta \vec{j} \quad (3.12)$$

where \vec{i} , \vec{j} are unit vectors in the 'x', and 'y' directions. Note that this is the combined Burgers vector for the two sheets. The idea is that these dislocations accommodate some

relative shear and rotation between the two sheets by permitting the regions between dislocations to find their complement with the dislocation region itself carrying the shear.

To relate the shear to the characteristics of the dislocation, note that averaged over many dislocations the mean displacement field corresponding to Figure 3.12c is

$$u_x = \frac{c \sin \beta}{\alpha} x + \frac{c \cos \beta}{\alpha} y \quad (3.13a)$$

$$u_y = \frac{c \sin^2 \beta}{\alpha \cos \beta} x - \frac{c \sin \beta}{\alpha} y \quad (3.13b)$$

The corresponding average strain field and rotation are

$$\varepsilon_{xx} = \frac{c \sin \beta}{\alpha}; \varepsilon_{yy} = -\frac{c \sin \beta}{\alpha}; \varepsilon_{xy} = \frac{c}{2\alpha \cos \beta}; \omega_{xy} = \frac{c \cos(2\beta)}{2\alpha \cos \beta}. \quad (3.14)$$

Since the strain field has to conserve area, there are only two independent quantities, ε_{xx} and ε_{xy} . Given some mismatch strain and assuming that the dislocation configurations are given by the simple array shown in Figure 3.12b, Eq. (3.14) determines the angle and average distance between dislocations that is needed to accommodate the relative shear and misorientation. Note the inverse relationship between spacing between dislocations and the strain. Eq. (3.14) can be solved to give

$$\beta = \frac{1}{2} \sin^{-1} \left(\frac{\varepsilon_{xx}}{\varepsilon_{xy}} \right) \quad (3.15)$$

3.5 Summary and discussion

The observations and data reported in Figures 3.4 ~ 3.7 show that flexible strips with channels can insert into complementary channels, yielding strongly enhanced adhesion. Optimal properties appear to require aspect ratios in the range 1-3 and spacing 2-4 times the pillar width. Outside these ranges, adhesion is attenuated by defects such as those due to the need to accommodate misorientation, or because the pillars are too slender and close to each other. We carried out adhesion tests on both complementary and mismatched micro-channel/micro-pillar surfaces. Adhesion, as measured by energy release rate of an interface crack, can be enhanced by up to forty times for complementary interfaces and still be significantly enhanced for some special non-complementary samples, despite the nearly negligible adhesion for other mismatched pairs. The increase in adhesion for short and moderately long pillars can be attributed to a combination of friction pull-out of pillars and a crack trapping mechanism. Indeed, our experiments shows that, up to a certain channel depth (about 20 μm in our case) increase of channel depth is beneficial since the amount of energy dissipated by friction during extraction is directly proportional to d^2 . For a complementary surface where $d = c = 20 \mu\text{m}$, a rough estimate of the contribution to the effective work of adhesion due to the friction pull-out mechanism is about 3 J/m^2 , which is about 15 times the work of adhesion of a flat control sample, significantly larger than the enhancement factor of ~ 5 due to the crack trapping mechanism. However, since these energy dissipation mechanisms can operate only when the pillars are in good contact with the grooves of the channels, it becomes ineffective as channel depth increases as long pillars are much more flexible and

even a very small misalignment can cause them to buckle, preventing insertion of pillars into channels. As a result, long pillars and wide channels will increase the number of misfit dislocations. Since the strain energy associated with these dislocations varies as the square of the inter-channel spacing, the presence of misfit dislocations can easily negate the friction and crack trapping enhancement mechanisms (e.g. compare Eq. (3.5) and Eq. (3.11)).

The analysis in this work can be improved significantly. Our model decouples the crack trapping mechanism from friction pull-out. Our expression for the energy associated with a dislocation assumes that the dislocation is a pure screw dislocation, and more importantly, the strain energy stored in the core, which can be a significant fraction of the stored energy, has been neglected in our calculation. Estimating the energy stored in the dislocation core is a non-trivial contact mechanics problem, since deformations of the pillars and channels in the core region are coupled to mechanical response of the backing layer and interfacial friction.

Our work shows that adhesion between flexible sheets can be enhanced significantly and made highly selective by simple complementary pillar-channel surface profiles. Such surface structuring suggests a new way by which functional surfaces can be designed for applications such as adhesives, fasteners, moving small objects, or bandages/adhesives in biomedical applications.

3.6 References

- [1] Scherge, M.; Gorb, S. N. *Biological Micro- and Nano-Tribology, Nature's Solutions*; Springer Verlag: Berlin, 2001.

- [2] Autumn, K.; Liang, Y. A.; Hsieh, S. T.; Zesch, W.; Wai, P. C.; Kenny, T. W.; Fearing, R. S.; Full, R. J. *Nature* **2000**, *405*, 681-685.
- [3] Jagota, A.; Hui, C-Y. *Materials Science and Engineering R* **2011**, *72*, 253-292.
- [4] Russell, A. P. *Integr. Comp. Biol.* **2002**, *42*, 1154-1163.
- [5] Stork, N. E. *J. Exp. Biol.* **1980**, *88*, 91-107.
- [6] Autumn, K.; Peattie, A. M. *Integr. Comp. Biol.* **2002**, *42*, 1081-1090.
- [7] Autumn, K.; Sitti, M.; Liang, Y. A.; Peattie, A. M.; Hansen, W. R.; Sponberg, S.; Kenny, T. W.; Fearing, R. S.; Israelachvili J. N.; Full, R. J. *Proc. Natl Acad. Sci.* **2002**, *99*, 12252-12256.
- [8] Persson, B. N. *J. Chem. Phys.* **2003**, *118*, 7614-7621.
- [9] Jagota, A.; Hui, C-Y.; Glassmaker, N. J.; Tang, T. *MRS Bull.* **2007**, *32*, 492.
- [10] Hui, C-Y.; Jagota, A.; Shen, L.; Rajan, A.; Glassmaker, N.; Tang, T. *J. Adh. Sci. & Tech.* **2007**, *21*, 1259-1280.
- [11] del Campo, A.; Greiner, C.; Arzt, E. *Langmuir* **2007**, *23*, 10235-10243.
- [12] Majumder, A.; Sharma, A.; Ghatak, A. *Bio-Inspired Adhesion and Adhesives: Controlling Adhesion by Micro-nano Structuring of Soft Surfaces in Microfluids and Microfabrication*, Springer: USA, 2010.
- [13] Gorb, S.; Varenberg, M.; Peressadko, A.; Tuma, J. *J. R. Soc. Interface* **2007**, *4*, 271-275.
- [14] Kim, S.; Sitti, M. *Appl. Phys. Lett.* **2006**, *89*, 261911-261913.
- [15] Ko, H.; Lee, J.; Schubert, B. E.; Chuah, Y-L.; Leu, P. W.; Fearing, R. S.; Javey, A. *Nano lett.* **2009**, *9*, 2054-2058.
- [16] Lamblet, M.; Verneuil, E. ; Vilmin, T.; Buguin, A.; Silberzan, P.; Leger L. *Langmuir* **2007**, *23*, 6966-6974.
- [17] Shamsavan, H.; Zhao, B. *Langmuir* **2011**, *27*, 7732-7742.
- [18] Jeong, H. E.; Lee, J-K.; Kim, H. N.; Moon, S. H.; Suh, K. Y. *Proc Natl. Acad. Sci.* **2009**, *106*, 5639-5644.
- [19] Chan, E. P.; Smith, E. J.; Hayward, R. C.; Crosby, A.J. *Adv. Mater.* **2008**, *20*, 711-716.

- [20] Parness, A.; Soto, D.; Esparza, N.; Gravish, N.; Wilkinson, M.; Autumn, K.; Cutkosky, M. *J. R. Soc. Interface* **2009**, *6*, 1223-1232.
- [21] Dai, Z.; Gorb S. N.; Schwarz, U. *J. Exp. Biol.* **2002**, *205*, 2479-2488.
- [22] Gorb, S. N. *Proc. R. Soc. Lond. B: Biol. Sci.* **1999**, *266*, 525-535.
- [23] Alberts, B.; Johnson, A.; Lewis, J.; Raff, M.; Roberts, K.; Walter, P.; *Molecular Biology of the Cell. 5th ed.* Garland Science, New York, 2008.
- [24] Branden, C.; Tooze, J.; *Introduction to Protein Structure 2nd ed.*, Garland Publishing , New York, 1999.
- [25] Anastasiadis, S. H.; Retsos, H.; Pispas, S.; Hadjichristidis, N.; Neophytides, S. *Macromolecules* **2003**, *36*, 1994-1999.
- [26] Koberstein, J. T. *J. Poly. Sci. B* **2004**, *42*, 2942-2956.
- [27] Koberstein, J. T.; Duch, D. E.; Hu, W.; Lenk, T. J.; Bhatia, R.; Brown, H. R.; Lingelser, J. P.; Gallot, Y. *J. Adh.* **1998**, *66*, 229-249.
- [28] Zhou, F.; Huck, W. T. S. *Phys. Chem. Chem. Phys.* **2006**, *8*, 3815-3823.
- [29] Kokkoli, E. ; Zukoski, C.F. *Langmuir* **2001**, *17*, 369-376.
- [30] de Mestral, G. *U.S. patent 2717437*, 1955.
- [31] Vajpayee, S.; Khare, K.; Yang, S.; Hui, C-Y.; Jagota, A. *Adv. Func. Mater.* **2011**, *21*, 547-555.
- [32] Vajpayee, S. *PhD thesis: Contact Mechanics and Adhesion of Structured Surfaces*, Lehigh University, 2010.
- [33] Ghatak, A.; Vorvolakos, K.; She, H.; Malotky, D. L.; Chaudhury, M. K. *J. Phys. Chem. B* **2000**, *104*, 4018-4030.
- [34] Vorvolakos, K.; Chaudhury, M. K. *Langmuir* **2003**, *19*, 6778-6787.
- [35] Chateauinois A., Fretigny C., *Eur. Phys. J. E* **2008**, *27*, 221-227.
- [36] Vajpayee, S.; Hui, C-Y.; A. Jagota, *Langmuir* **2008**, *24*, 9401-9409.
- [37] Hirth, J. P.; Lothe, J., *Theory of Dislocations*, McGraw-Hill, New York, 1983.
- [38] Jin, C.; Jagota, A.; Hui, C.-Y., *Adv. Funct. Mater.* **2013**, *23*, 3453-3462.

Chapter 4 Frictional Auto- Roughening of a Surface with Spatially Varying Stiffness

We show that significant reduction of sliding friction can be achieved between a rigid surface and a flat elastic surface by spatial variation in stiffness of the latter. This reduction in friction during sliding occurs due to an “auto-roughening” phenomenon in which a fully connected contact region breaks into partial contact. An elastomer, poly(dimethylsiloxane) (PDMS), was used to fabricate nominally flat surfaces with regions of two different stiffness, achieved by using two different concentrations of cross-linker. Both experiments and finite element simulation show that, for sufficiently high friction and low normal load, the real contact area between a rigid indenter and a surface with spatially varying stiffness is reduced significantly due to auto-roughening. The finite element model also shows how the auto-roughening depends on the contact openings of interfacial structures, resulting in reduced overall friction.

4.1 Introduction

Friction arises whenever two materials in contact move relative to each other.¹ Deliberate control of friction, say, an elastomer sliding against a rigid substrate, is of great practical importance in many applications, e.g., tires,²⁻⁴ windshield wipers^{5,6} and in seals. Depending on the situation, one desires high or low friction, and this depends on the physical properties of the materials^{1,7} and near-surface texture.⁸ At the molecular scale, friction arises due to molecular stick-slip,^{9,10} a rate-dependent process,¹¹ and adhesion.^{7,11-13} For stiff materials, friction is intimately related to limited asperity contact and deformation; for compliant materials such as elastomers, intimate contact between the surfaces is more easily attained.⁷

Several recent studies have shown that contact mechanical properties, including both friction and adhesion, can be significantly modified by surface microstructure. Several designs of near-surface architectures have been inspired by the biological attachment systems,¹⁴⁻¹⁶ for example, the fibrillar structure observed on contact pads of lizards. Several bio-mimicked and bio-inspired structures have been developed in recent years.^{8,17-25} Glassmaker *et al*²⁶ and Noderer *et al*²⁷ found that the adhesion and surface compliance can be strongly enhanced by a film-terminated fibrillar architecture. Several fibrillar structures terminated by “mushroom”-like ends^{20,28,29} have been developed that achieve enhanced adhesion. Ghatak and co-workers^{30,31} have reported strong enhancement of adhesion with sub-surface micro-structures. Guduru and co-workers showed how crack-trapping by a wavy interface can enhance adhesion.³² Control of

adhesion by spatial variation in properties was also investigated by Kendall³³ using a composite material with periodic variation in stiffness.

Surface structuring can also be used to modulate friction. Gorb and Varenberg²⁹ showed that fibrillar surfaces can exhibit smooth and stable sliding with much lower friction force, in contrast to the stick-slip motion of a control flat surface.³⁴ On the other hand, Kim *et al*³⁵ reported enhanced static friction for micro-pillar patterned elastomer surfaces. Similarly, Shen *et al*³⁶ and Vajpayee *et al*³⁷ have also shown that the static friction can be increased significantly on a film-terminated fibrillar interface. Rand *et al*³⁸ showed that the sliding friction can be reduced by surface wrinkles.

In this work we investigated the effect on friction of an elastomeric surface with periodic spatial variation in properties. We measured sliding friction between a smooth, stiff, indenter and a nominally flat surface of an elastomer with spatial variation in elastic moduli. The principal new finding of this work is that the surface undergoes a frictional “auto-roughening” phenomenon, which results in a transition from full to partial contact during the sliding phase, and decreases the friction force considerably. Through finite element simulation we demonstrate that auto-roughening requires both spatial variation in modulus and sufficient frictional stress.

4.2 Experimental methods

4.2.1 Sample fabrication

Figure 4.1 illustrates the fabrication process. We started with a series of silicon molds patterned by photolithography, which were basically of two types. The first one

had 1-D parallel channels³⁹ with two different channel depths ($d = 10$ & $25 \mu\text{m}$) and three different spacings (center to center distance, $c = 20, 35$ & $50 \mu\text{m}$). Using previously described techniques,³⁸ we molded an elastomer, poly-dimethylsiloxane (PDMS, Sylgard® 184 Dow Corning) onto the silicon mold, resulting in replicas of the sort shown schematically in Figure 4.1a. The second surface profile design comprises a 2-D arrangement of holes that, on molding PDMS, yielded fibrillar structures⁴⁰ shown in Fig. 1b. All of the molds for this second design have the same fibril height ($h = 17.8 \mu\text{m}$), and the spacing between two nearest fibrils was varied as $s = 20, 35$ & $50 \mu\text{m}$. The spaces between the channels/fibrils are subsequently filled with a lower modulus PDMS, as described below.

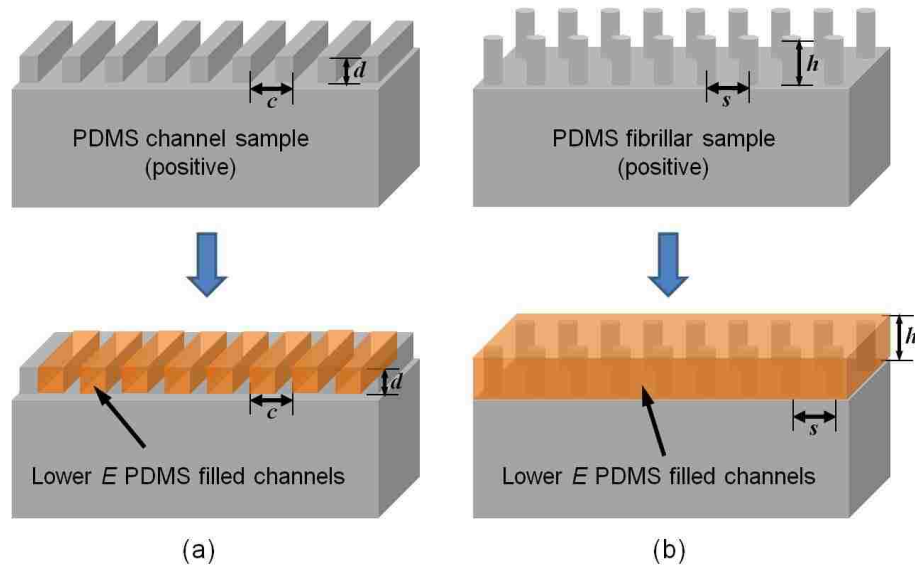


Figure 4.1 Schematic diagram of the process that creates surfaces with (a) 1-D and (b) 2-D periodic variation in stiffness.

Liquid PDMS precursor was made by a mixture of silicone elastomer base with curing agent. PDMS stiffness was adjusted by varying the curing agent (cross-linker) concentration. In order to distinguish optically the different regions on the surface, we added a small amount of carbon black to serve as a pigment (approximately 0.2 wt%, dissolved in toluene and prepared by bath-sonication for at least two hours) into the stiffer PDMS precursor. Typically, this first molding used the stiffer PDMS which was generated by mixing silicone elastomer base and curing agent at a weight ratio of 10:1, along with additional carbon black pigment. The mixture was degassed for 30 minutes under vacuum, then applied to the silicon masters, and cured at 80°C temperature for two hours after the molding step. The structured sample obtained after the first step was, in the second step, backfilled with lower modulus (and transparent) PDMS liquid. This second phase was mixed with a weight ratio of 20:1 of silicone base:cross-linker, dissolved in additional toluene (6.0 wt%) to increase the flowability, which further decreased its elastic modulus. Using indentation tests based on Johnson-Roberts-Kendall (JKR) theory (tests were carried out at loading rate = 1.0 $\mu\text{m}/\text{sec}$),⁴² the Young's moduli for the 10:1 (with carbon black) and 20:1 PDMS were found to be 3.84 (± 0.08) MPa and 1.64 (± 0.06) MPa, respectively.^h

^h The measurement of elastic moduli for both stiff and compliant PDMS was implemented with assistance of Dr. Dadhichi Paretkar.

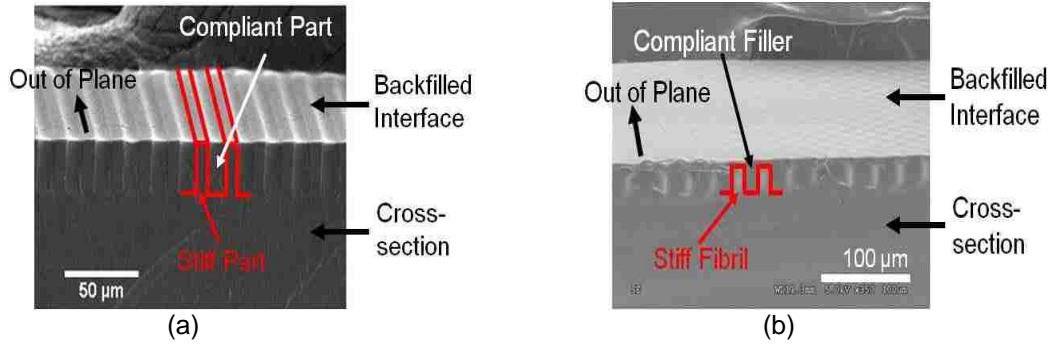


Figure 4.2 SEM images of different structured composite samples: (a) surfaces with 1D variation in stiffness, channel depth $d = 25 \mu\text{m}$ and interchannel spacing $c = 20 \mu\text{m}$; (b) surfaces with 2D variation in stiffness, fibril length $h = 17.8 \mu\text{m}$ and spacing $s = 20 \mu\text{m}$.

Two different approaches were used to create the composite 1-D ridge/channel and 2-D fibrillar surface structures. The 1-D ridge/channel micro-channel structures were filled by the compliant second phase by liquid flow into the grooves driven by capillarity. We pressed the structured side of the PDMS sample obtained after the first molding against a glass slide with a spin-coated thin polystyrene film. Then, the liquid mixture of toluene and PDMS (with lower cross-linker concentration) was poured on one side of the structured sample. The entire assembly was placed at room temperature with a dead weight on top. The liquid was pulled into the channels by capillarity and cured in place. Figure 4.2a shows a scanning electron microscope (SEM) image of a backfilled micro-channel sample with spacing, c , of $20 \mu\text{m}$.

The capillary force method did not work well for the 2-D fibrillar structures, as the fibrils tended to bend and buckle under the dead load required to maintain uniform contact. For these samples, after the stiff PDMS sample with a fibrillar surface structure was generated, the second precursor with lower cross-linker concentration was spun into a thin film of the same thickness as the height of fibrils using a Modular Spin Processor

(Laurell Technologies Corporation). Then, we placed the structured PDMS sheet onto the thin film with the structured side face down, so that the fibrils were fully inserted into the liquid precursor, and cured the sample at 80°C for 2 hours. An SEM micrograph of a backfilled fibrillar sample is shown in Figure 4.2b.

Although the backfilling process was carried out against flat glass or silicon, the surface had some undulation (with amplitude of less than 1 μm) in both cases (Figure 4.2). A typical surface profile for a backfilled ridge/channel sample (Figure B.1 in Appendix B) measured using an interferometric optical profilometer (ZeGage. Zometrics, Inc), shows surface undulations with amplitude of about 300 nm. Also, as shown later, the initial contact region upon indentation by a smooth sphere is bounded by a somewhat undulating line. The contact on the stiffer regions is larger than the compliant parts by the edge, since the stiff segments are relatively higher. However, we consider the influence of this surface undulation to be minimal, since the amplitude is small compared to the other dimensions. This is discussed further in the Section 4.3 and Appendix B.

4.2.2 Friction measurement

Our experimental set-up for studying the frictional behavior of the backfilled samples is shown schematically in Figure 4.3. A spherical glass indenter with a diameter of about 4.0 mm was precoated by vapor-depositing a self-assembled monolayer of n-hexadecyltrichlorosilane ($\text{C}_{16}\text{H}_{33}\text{Cl}_3\text{Si}$) on the surface, in order to reduce adhesion. Details of this coating process can be found in the work of Glassmaker *et al* ²⁶. The glass indenter was placed on the sample under controlled normal load. The sample was

attached to a glass slide above an inverted optical microscope. The glass slide was moved by a variable speed motor (Newport ESP MFA-CC) at a fixed speed ($u = 10 \mu\text{m}/\text{second}$), via a Newport ESP300 motion controller. The resisting shear force was measured by a load cell (Honeywell Precision Miniature Load Cell).

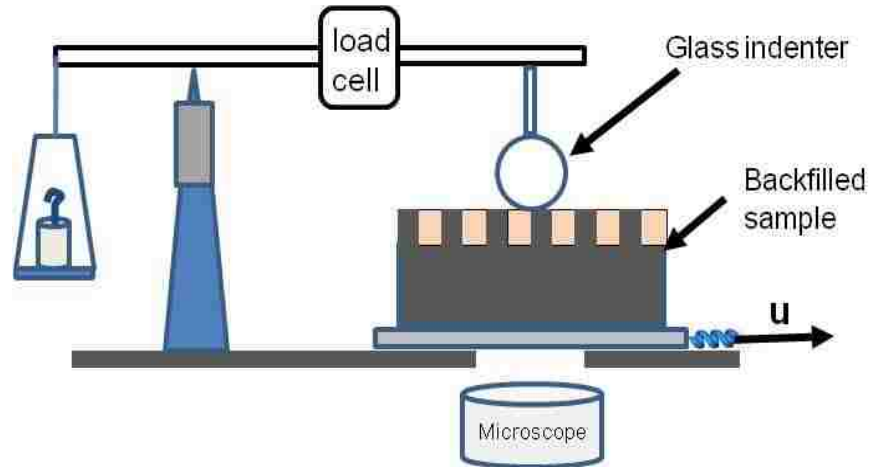


Figure 4.3 Experimental set-up for the friction tests. A spherical indenter was lowered onto the sample with a normal load in the range of 3-20 mN. The horizontal movement of the indenter was driven by a D.C. motor, the shear force was measured by the load cell, and images of the contact between the indenter and sample were recorded through the inverted optical microscope. The sample on the glass substrate was connected to the motor by adhesive tape, drawn as a blue spring in this figure.

4.3 Results and discussion

4.3.1 Friction test on homogeneous control samples

Control friction tests were carried out on nominally flat surfaces of homogeneous stiff and compliant samples. We observed that the contact was maintained throughout over a single region for both the controls. Figure 4.4a and 4.4b show two optical micrographs of the contact region (darker area) between the stiff flat control sample and indenter. Figure 4.4a shows the initial contact before the sample is sheared relative to the

indenter – the area is nearly circular. Figure 4.4b shows the contact area during sliding. We observe that the contact area decreases in size and changes to an oval shape, and the indenter slides smoothly on the material. Figures 4.4c, 4.4d & 4.4e show three micrographs of the contact region between the same rigid indenter and the compliant flat control sample. During the friction experiment, we observed Schallamach wave propagation.⁴¹ Notice, for instance, that the contact areas in Figure 4.4d and 4.4e (darker regions) are quite different although both pictures were taken during sliding. This occurs because in Figure 4.4d a Schallamach wave has just exited the trailing edge (TE) of the contact region. Consistent with this observation, force traces vary periodically as discussed in the next section.

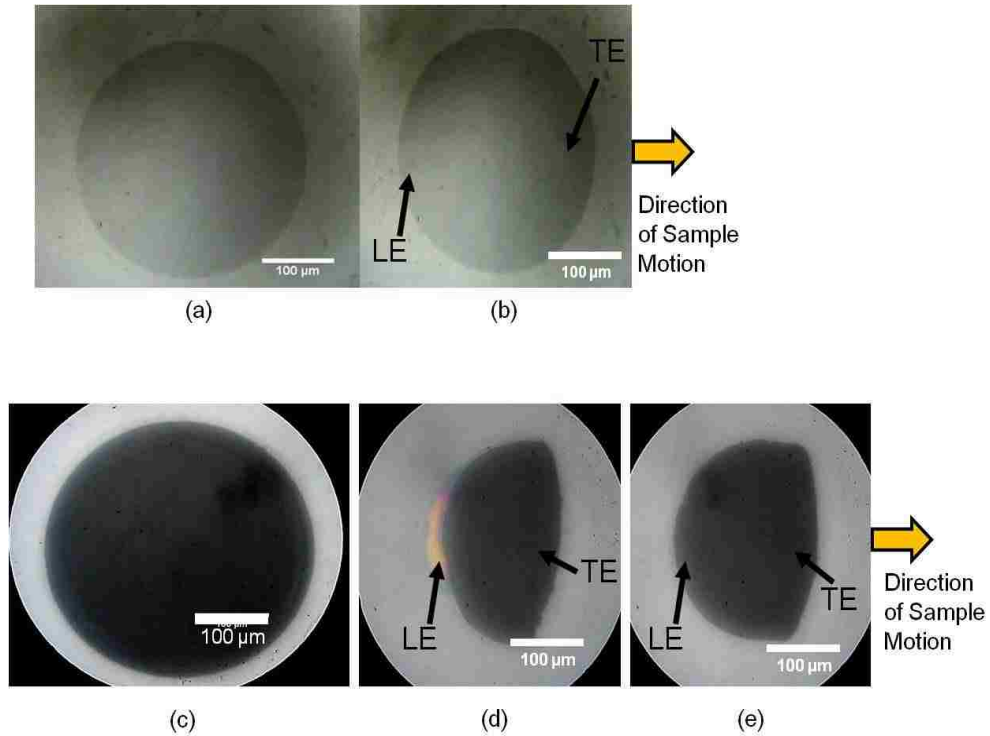


Figure 4.4 Optical micrographs of spherical glass indenter sliding on a flat homogenous control sample. The glass indenter was held fixed and the sample was moved to the right. The letters ‘TE’ and ‘LE’ denote the trailing and leading edge of the contact, respectively. (a,b): contact area before sliding (a) and during sliding (b) on the stiff PDMS; (c,d,e): (c) contact area before sliding and (d,e) during sliding on the compliant PDMS.

4.3.2 Friction test on samples with 1-D and 2-D periodic variation in properties

4.3.2.1 Surface patterned by stripes with different, alternating stiffness

Figure 4.5a shows typical measurements of shear force for 1-D samples with the same channel depth ($d = 10 \mu\text{m}$) but different spacing, compared to the two control samples for a relatively light normal load, $F_N = 3.5 \text{ mN}$. For the stiff control, the shear force builds up quickly and goes into steady sliding. For the compliant control, the shear force response shows an initial “static friction” peak, which corresponds to adhesive

failure of the contact and initiation of sliding. The following periodically-varying shear force is indicative of Schallamach wave propagation.

One might expect that the frictional resistance against shear of a composite surface will lie between the two limiting cases in which the material is homogeneous. However, all three composite samples have significantly smaller friction force than either the stiff or the compliant homogeneous controls. The sample with smallest spacing ($c = 20 \mu\text{m}$) has the lowest friction, which increases systematically with increase in spacing, corresponding to increasing surface area fraction of the more compliant material.

Figure 4.5b shows optical images of the contact region in a composite surface before and during sliding. The initial contact is roughly circular, with undulations corresponding to stiff and compliant regions (the dark region in Figure 4.5b, picture labeled ‘Initial Contact’). As the interface is loaded in shear, the friction force builds up to a “static friction” peak, and then drops as sliding commences. During sliding, the contact region is smaller in overall diameter and, more significantly, shows clearly a transition from full to partial contact between the indenter and the material surface. We call this transition from full to partial contact “auto-roughening”. This significant reduction in contact area evidently reduces the friction force. As shown in Figure 4.5b, the contact region separates into ~10 striped regions with each strip partially on the stiff material and partially on the compliant one (see insert in Figure 4.5b ‘Sliding Phase’). Each strip of contact has about the same width in its middle, and the width tapers towards the ends. The envelope of the contact regions represents an overall apparent contact area. The previously observed asymmetry in contact shape (Figure 4.4b) is not so evident; it

manifests as a systematic difference in the width of contact strips at the leading and trailing edges. If one follows a particular strip over time, we observe that it nucleates at the leading edge and grows in width and length as it enters the contact. After reaching its maximum length, the contact strip decreases in size, eventually vanishing at the trailing edge. We observe in Figure 4.5a that the shear force varies periodically for the composite samples during sliding. In this case, unlike the homogeneous control, the period corresponds to the periodic variation in modulus of the surface, that is, the length of each period is identical to its corresponding inter-channel spacing (see insert in Figure 4.5a).

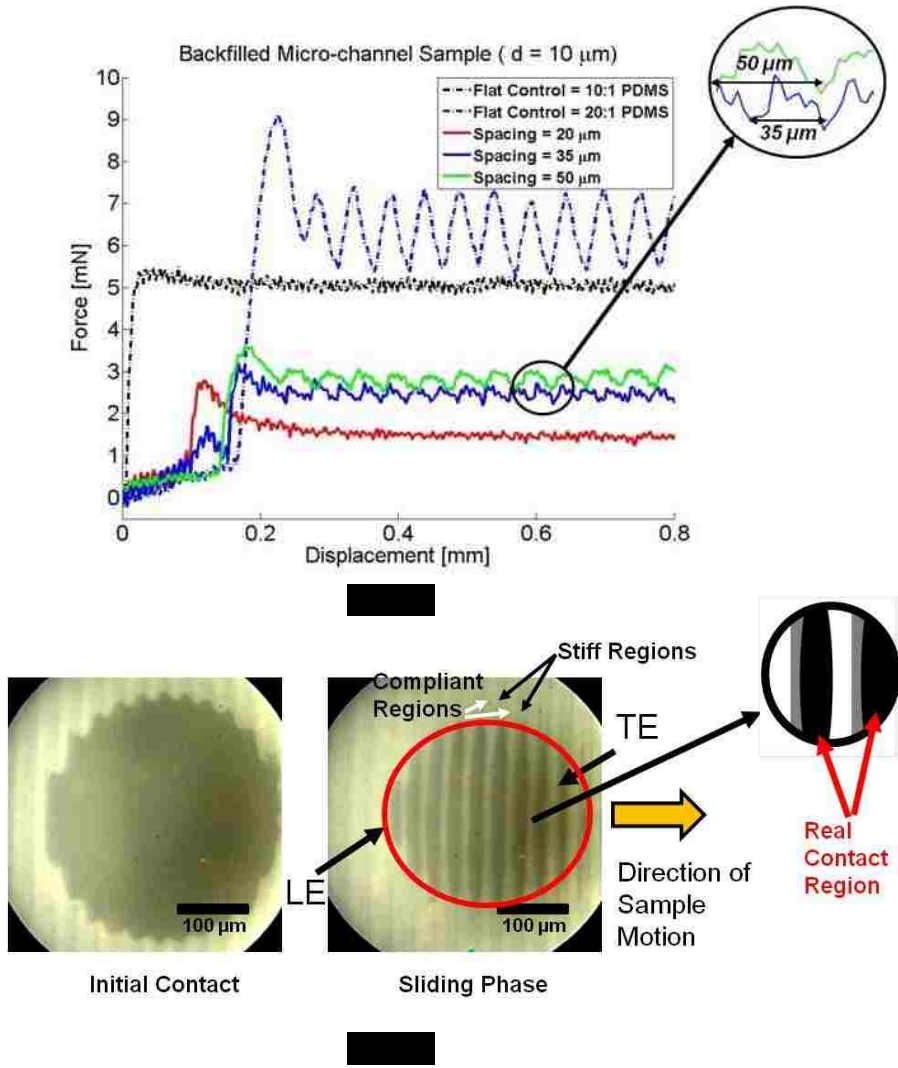


Figure 4.5 (a) Shear force as a function of shear displacement for samples with 1-D periodic variation of stiffness and both homogeneous controls; (b) optical micrographs taken during a friction test on a sample with spatially varying stiffness (depth $d = 10 \mu\text{m}$, spacing $c = 35 \mu\text{m}$) shows a transition from initially full contact (before sliding) to partial contact during sliding. The red circle marks the apparent contact area measured by encircling all the dark stripes together (regions in contact) during sliding. The black region marks a small segment of contact, which is enlarged and drawn schematically on the right hand side, to illustrate that the real striped contacts are partially on the stiff material (grey strips) and partially on the compliant material (white regions).

As noted in Section 4.2.1 and Appendix B, the surface profile of the composite samples often had some waviness. In cases where the compliant component was in excess of that required to fill the channels, it appeared as a thin layer covering the entire surface (also in the Appendix B, Figure B.2). Data from such samples was discarded, because the indenter made contact only with the compliant material, not with alternating stiff and compliant regions. Waviness of the sample surface raises a natural question about the extent to which the auto-roughening reported in this work is due to surface roughness instead of spatial variation in stiffness. We found that even the samples that were coated completely by the compliant elastomer and had a flat surface always showed clear auto-roughening. Based on this observation we surmise that spatial variation in stiffness plays the dominant role in auto-roughening.

4.3.2.2 *Stiff regions in a 2-D array surrounded by compliant regions*

A similar auto-roughening transition occurs in the samples with 2-D periodic variation in modulus; Figure 4.6a shows a typical example of friction-displacement curves. Again, the sliding friction force for the composite samples is lower than that of both the flat control samples under the same normal load ($F_N = 3.5 \text{ mN}$). Larger spacings ($c = 35 \text{ \& } 50 \text{ }\mu\text{m}$), with correspondingly larger area of the compliant material on the surface, still exhibit little enhancement of friction.

Figure 4.6b shows micrographs of the contact region. The dark region on the left hand side of Figure 4.6b ('Initial Contact') shows the contact under normal load before shear force is applied. On the right hand side, the grid-like dark regions represent the real

contact area during sliding. The transition from full to partial contact is evident. At the leading edge, the fraction of area in contact is larger than at the trailing edge.

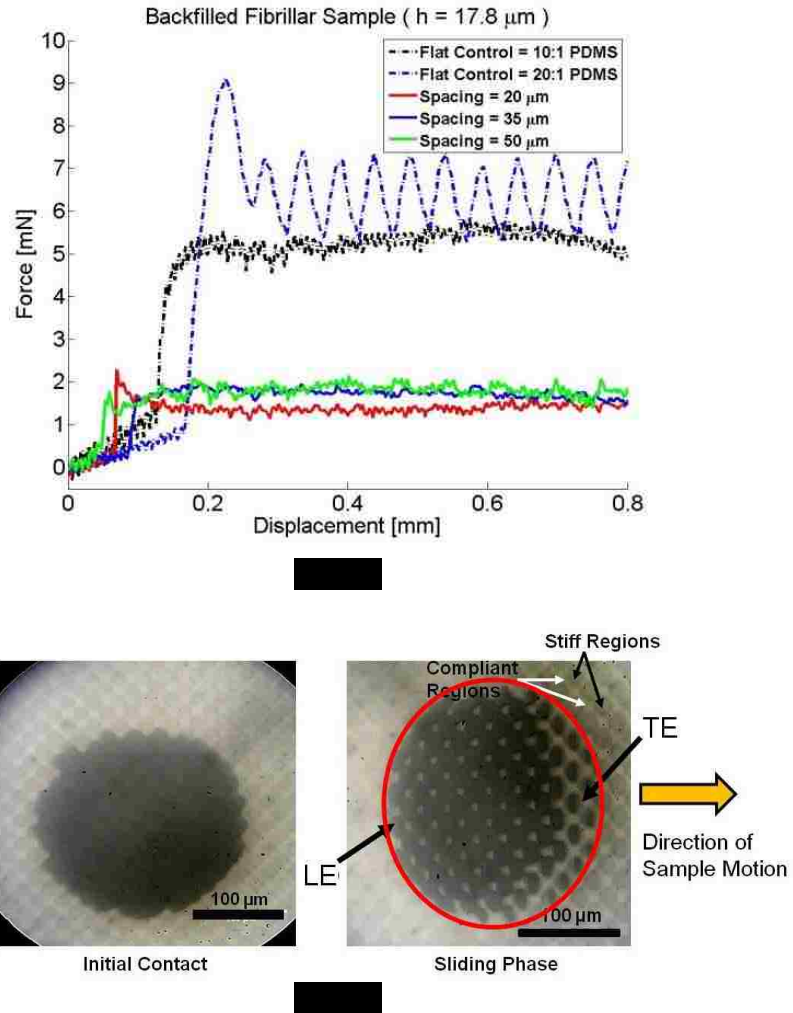


Figure 4.6 (a) Shear force as a function of shear displacement for samples with 2-D variation in stiffness and both homogeneous controls; (b) optical micrographs taken during a friction test on composite fibrillar samples (depth $d = 10 \mu\text{m}$, spacing $c = 20 \mu\text{m}$) showing a transition from initially full contact (before sliding) to partial contact during sliding. The red circle marks the apparent contact area that encircles the entire grid-like dark regions during sliding.

4.3.3 Friction test under different normal loads

Because the reduction in sliding friction due to auto-roughening is due to reduction in real contact area, one would expect that with increasing normal load the auto-roughening phenomenon might be prevented, possibly resulting in recovery of frictional resistance. We conducted experiments using significantly larger normal forces and examined both 1-D micro-channel and 2-D fibrillar structured composite samples.

Figure 4.7a shows micrographs of the contact region before sliding ('Initial Contact') and during sliding ('Sliding Phase') for a backfilled microchannel sample under a normal force $F_N = 12.0 \text{ mN}$. Other than being larger in size, the contact is very similar in character to that shown in Figure 4.5b. However, during the sliding phase, unlike in Figure 4.5b in which the contact broke into a number of smaller regions, in Figure 4.7a we observe partial contact at the periphery and full contact in the middle contact region (which bears the highest compressive normal traction). As a result, the corresponding frictional shear forces on composite samples are higher, although they are still lower than either of the flat control samples, as shown in Figure 4.7b.

A similar effect was observed for larger normal load in the case of the samples with 2-D variation in modulus. Again, in the center region contact is complete whereas at its periphery contact is partial, especially at the trailing edge (Figure C.1 in Appendix C). Similarly, the sliding friction remains lower than both controls (Figure C.2 in Appendix C).

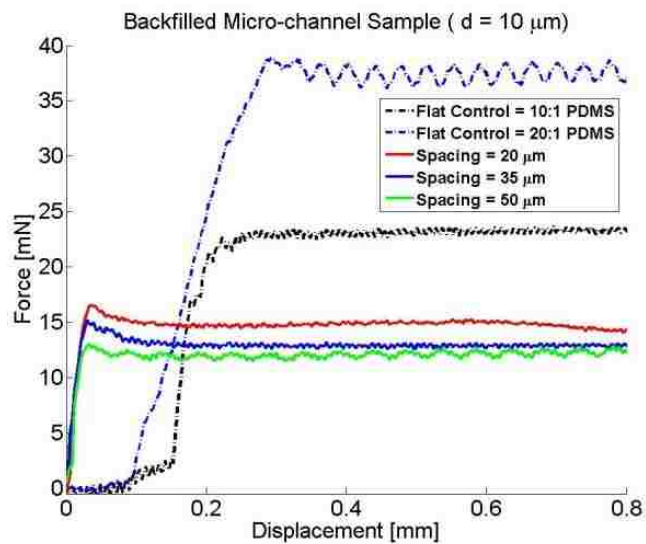
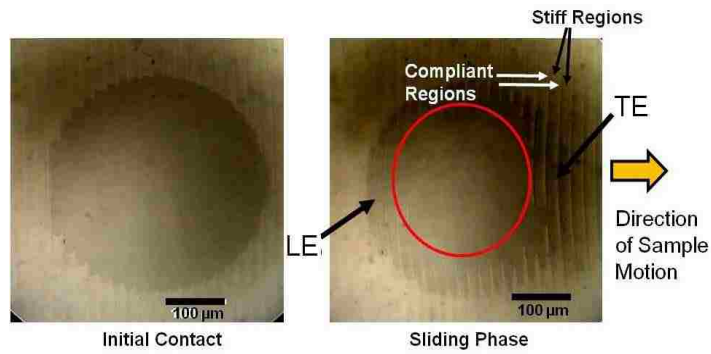


Figure 4.7 (a) Optical micrographs taken during a friction test on backfilled micro-channel samples ($d = 10 \mu\text{m}$, $c = 20 \mu\text{m}$) show a transition from (a) initially full contact (before sliding) to (b) partial contact during sliding. The red circle marks out an inner region of full contact; (b) Shear force as a function of shear displacement.

4.3.4 Apparent shear stress

For more quantitative interpretation of experimental results, it is useful to normalize the measured friction force by the area of contact. For a fixed normal load the contact area changes because (a) the effective compliance of the samples varies with spacing and the amount of shear, and (b) the actual area of contact depends on the severity of the auto-roughening phenomenon. Here, we define the “apparent” contact area as the area enclosed by the perimeter of all the combined regions of actual contact, for example, as marked by the red closed curves in Figures 4.5b and 4.6b.

The apparent shear stress during sliding motion is calculated by dividing the sliding force by the apparent contact area. For each experiment, we randomly chose five images during the sliding phase, and measured the apparent contact area. The mean apparent shear stress and its variance were calculated as the ratio of average sliding friction and the average apparent contact area, corrected using the approximation given in Appendix D. The error bars shown in Figure 4.8 represent the standard deviation of the apparent shear stress. The calculation of apparent shear stress for the compliant control sample needs to account for the periodic variation in contact area and shear force due to the Schallamach waves. In this case, the frictional force was averaged over five different randomly picked “peak” values on the force trace and their corresponding “valley” values in the same periods, and the apparent contact area was calculated by averaging both the largest and smallest contact areas in five such periods during the sliding phase.

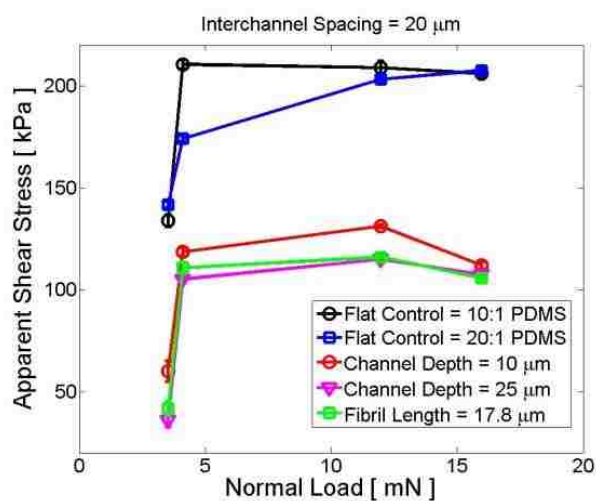
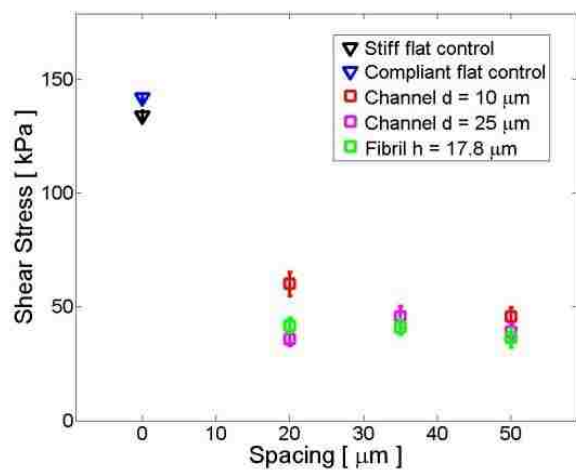


Figure 4.8 (a) Apparent shear stress of composite samples compared to both stiff and compliant flat controls, under the same normal load ($F_N = 3.5 \text{ mN}$). The spherical glass indenter was tested against 1-D micro-channel samples with two different depths ($10 \mu\text{m}$ & $25 \mu\text{m}$), and also 2-D micro-fibrillar arrays. (b) Apparent shear frictional stress for four different normal loads and fixed spacing of $20 \mu\text{m}$.

Figure 4.8a shows the apparent frictional stresses of a spherical glass indenter against several samples, under a normal load $F_N = 3.5 \text{ mN}$. Observe that the apparent shear frictional stress for all samples with periodic variation in modulus is significantly lower than for the controls ($\sim 36 \text{ kPa}$ vs $\sim 140 \text{ kPa}$). Note also that there is little variation between the various samples, from which we have established that the apparent shear stress is approximately independent of surface geometry.

Figure 4.8b shows how apparent friction stresses depend on normal load at a fixed spacing of $20 \text{ }\mu\text{m}$. In all three composite samples, friction increases initially with increasing normal load, but quickly attains a plateau value significantly lower than the stiff control. That is, even when the contact is apparently complete, a sample with periodic variation of properties always has friction lower than both stiff and compliant flat controls. Note that the apparent shear stress increases dramatically in the range of small normal load ($F_N = 3.5 \sim 4.1 \text{ mN}$). We surmise that the dark regions (in Figures 4.5b and 4.6b) do not always indicate the actual area of contact, i.e., that there are small gaps (compared to the wavelengths of white light) at a small normal load (in this case, when $F_N = 3.5 \text{ mN}$) which are not observed through the optical microscope. A small increase in normal force ($F_N = 4.1 \text{ mN}$) is needed to eliminate such contact gaps and to make full contact. This suggests that whereas apparent contact area can be measured reasonably accurately from our micrographs, measurement of real contact area in the case where it consists of separated islands is inaccurate.

4.4 Mechanism of auto-roughening effect

To better understand the mechanism of the “auto-roughening” transition observed experimentally, we analyzed the deformation of a surface layer with periodic variation in modulus using the finite element method. We built and analyzed a 2-D finite element model (FEM - ABAQUS[®], version 6.9). To simplify the analysis, all calculations were performed in plane strain. The spherical punch was replaced by a flat rigid punch having a width six times the periodic distance between two stiff regions. As shown in Figure 4.9a, the FEM model has two parts. The first is a flat surface layer consisting of periodically alternating stiff and compliant filled channels. The second part is the homogeneous bulk material under the surface layer, the backing. The backing is assigned properties of the stiff material, as in experiments. Both materials were assumed to be linearly elastic and isotropic. We assumed that contact is adhesionless, and contact pair definition in our FEM was applied to prevent interpenetration between contacting surfaces. Shear interaction between the rigid indenter and substrate surface was modeled by Coulomb friction limited by a maximum shear traction, τ_{max} , which we call the interfacial sliding stress. This sliding stress τ_{max} is assumed to be a material property and is the same for both the compliant and stiff materials. The Coulomb friction coefficient was chosen to be sufficiently large (a value of 5) so that in nearly the entire sliding region the shear traction equaled a constant value of τ_{max} . The assumption and value of the constant frictional shear traction is consistent with measurements on model elastomers.⁴³

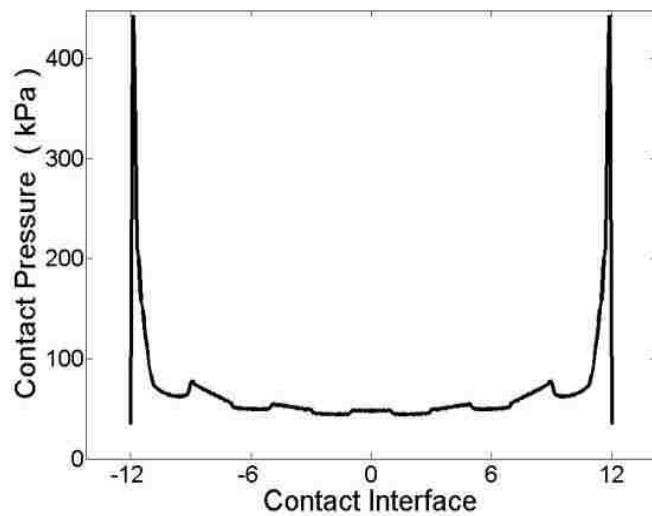
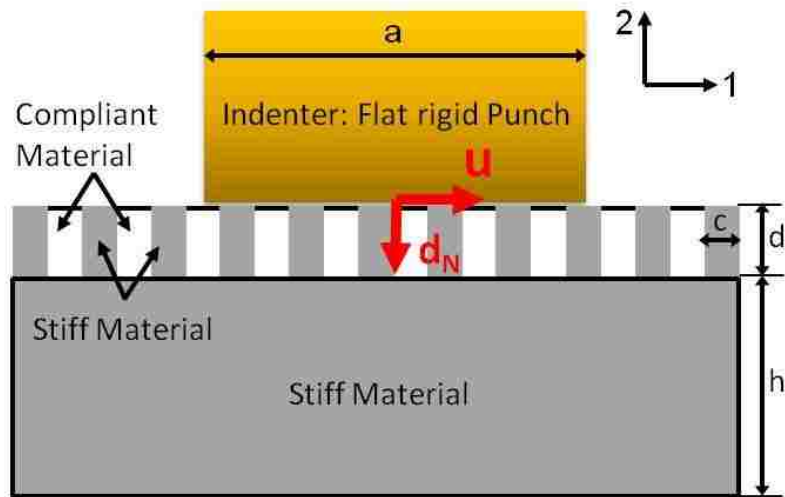


Figure 4.9 (a) Schematic of the cross-section of an elastic sample that is infinite in the out-of-plane direction. The sample has alternating stiff and compliant regions but an overall flat surface. A thick backing of the stiff material is attached underneath the surface. A rectangular rigid flat punch is moved from left to right (movement represented by 'u'). Normal force is applied by imposing a uniformly distributed vertical displacement to the indenter, and denoted by 'd_N' in this figure; (b) contact pressure along the interface during normal indentation without shear (end of step one), showing slight undulation due to the varying surface properties and pressure concentration at both edges.

The simulation is conducted in two steps. In the first step, the indenter is brought into contact with the material surface and a vertical downward displacement is applied. In the second step, the indenter is sheared relative to the sample, keeping the vertical displacement fixed. Although we use fixed vertical displacement in all our finite element calculations, we found that the vertical load remains approximately constant during shear, so fixing the vertical displacement is equivalent to fixing the vertical load.

For structures with periodic variation of modulus, the materials are assigned the following Young's moduli: for the stiffer material $E_1 = 2.5 \text{ MPa}$, and for the compliant material $E_2 = 1.0 \text{ MPa}$. (Poisson's ratio was fixed for both materials at $\nu = 0.49$.) The interfacial sliding stress τ_{max} was fixed at 100 kPa in our simulations⁴⁴. At the end of step one (Figure 4.9b), the contact pressure is characteristic of that expected for a rigid punch indenting a composite surface, i.e., with stress concentrations at the punch edges. (We tested our model by simulating a flat punch in contact with homogeneous material, see Appendix E, Figure E.1) In this step, the indenter is in full contact and the shear stress at the interface is very small compared with the contact pressure.

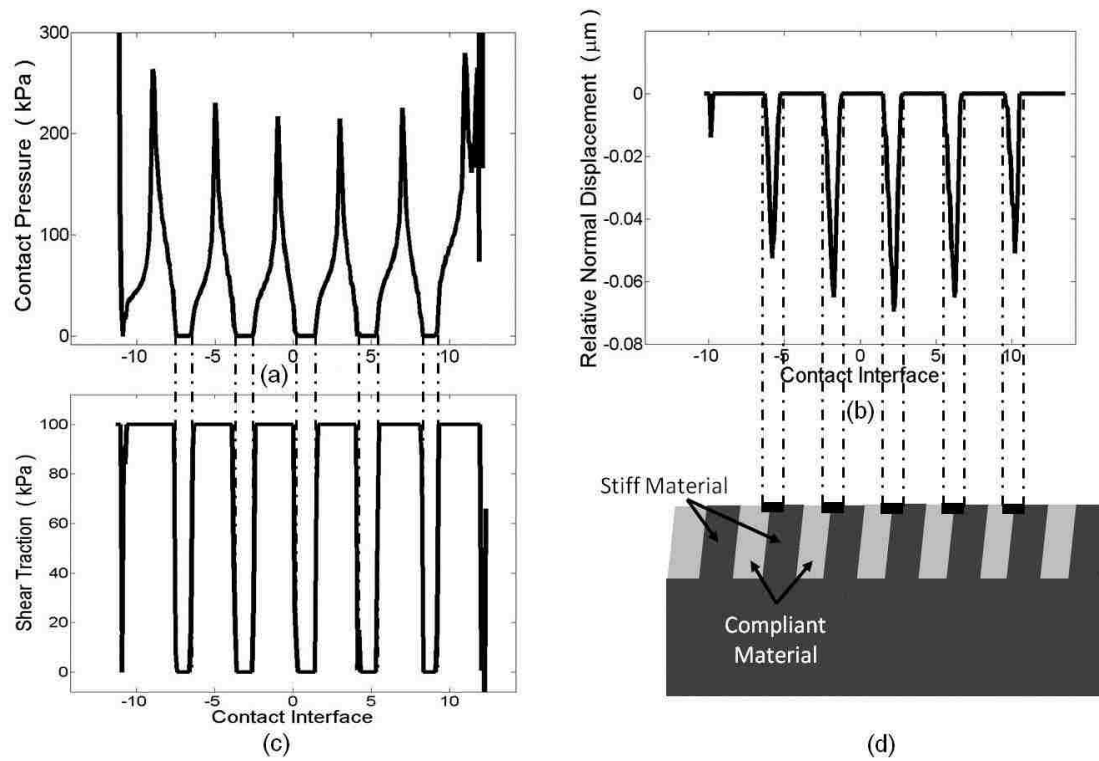


Figure 4.10 (a) Contact pressure along the interface under combined normal and shear displacement showing the development of periodic regions with zero contact pressure, (b) relative displacement of the surface profile with respect to the indenter showing periodic loss of contact, (c) Shear traction distribution along the interface showing periodic variation between zero stress (open contact) and 100 kPa (prescribed friction stress), (d) schematic illustration of the deformed structure during sliding phase. Black regions indicate contact opening between the punch and elastomer. Dark and light grey regions indicate stiff and compliant regions, respectively.

Figure 4.10 shows the corresponding results during the second step in which the indenter slides on the substrate. Figure 4.10a shows that there are periodic regions on the interface where the contact pressure is zero, i.e., contact is lost (Figure 4.10b). The contact pressure distribution is radically different from step one (as shown in Figure 4.9b). Figure 4.10c shows that the shear stress in these non-contact regions also vanishes, as expected. Figure 4.10b plots the relative vertical displacement on two sides of the contact pair surfaces, showing the development of periodic gaps up to $0.08\ \mu\text{m}$ (displacement normal to the sliding interface). Note that the predicted openings can be small compared to the wavelength of white light, reinforcing our hypothesis that in some cases openings may not be visible optically. In the contact regions (Figure 4.10c), the shear traction is $100\ \text{kPa}$, which is the given interfacial yield stress, τ_{max} . In Figure 4.10d, the black lines/segments show the non-contact regions where there is neither shear nor normal pressure. The contact regions straddle the stiff and compliant regions, consistent with the experimental observation in Figure 4.5b.

Our finite element simulation demonstrates that auto-roughening occurs due to the mechanics of friction against a surface with periodically varying properties. We now use the simulation to study how auto-roughening is controlled by the following three parameters:

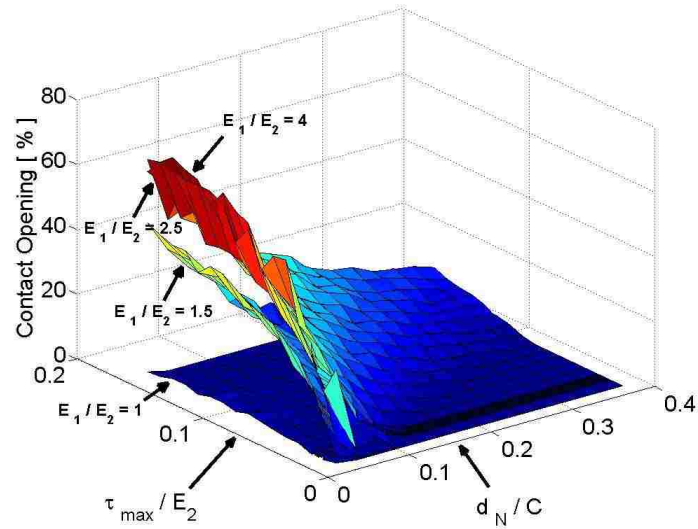
- **Normal Load:** Recall that experiments show that auto-roughening can be prevented at least partially if normal load is sufficiently high. In our simulation normal load is simulated by applying normal displacement on the indenter.


- **Ratio of Elastic Moduli:** Experiments and simulation show that there is no auto-roughening if the properties of the two materials are identical. It is therefore important to establish how auto-roughening varies as we change the ratio of elastic moduli.
- **Friction Stress:** Simulation also shows that auto-roughening vanishes in the absence of friction. We study how this effect depends on friction by varying τ_{max} .

In the following, auto-roughening is measured by the fraction of contact area that is open. Figure 4.11a shows 3-D plots of contact opening fraction as a function of the normalized interfacial sliding stress (friction stress divided by Young's modulus of the stiff material, τ_{max} / E_1) and normalized normal indenter displacement (vertical displacement applied to the indenter divided by length of one period, $\overline{d_N} = d_N/c$). First we notice that when the moduli of both materials are the same ($E_1 = E_2$), the indenter always maintains full contact regardless of τ_{max} or applied normal indenter displacement. However, for all the remaining cases where the two moduli differ from each other, $E_1 \neq E_2$ (here in Figure 4.11a, we show four different combinations of stiff and compliant materials and the modulus ratio $E_1 / E_2 = 1, 1.5, 2.5$ and 4), we find that the opening fraction depends strongly on both normal displacement and shear stress. The largest opening fractions are for high friction and low normal load. For larger values of the ratio of elastic moduli, E_1 / E_2 is larger than about 2, fractional opening becomes quite insensitive to it (Figure 4.11b). This suggests that relatively mild variation in material moduli can trigger the auto-roughening transition as long as adhesion can be neglected.

(In our experiments, the modulus ratio of stiff and compliant material is about 2.4.) From Figure 4.11, we notice that the fraction of contact opening for this case could reach up to about 70% under a small normal load, which is consistent with the 60 - 70% decrease in experimentally measured apparent shear stress (Figure 4.8).

We also conducted several simulations with a long cylindrical indenter. Here, we present only the results using a flat “punch” indenter because its apparent contact region is fixed, facilitating comparison between different cases. Results obtained using cylindrical indenters were qualitatively very similar to those presented above.




 $\tau_{max}/E_2 = 0.1$

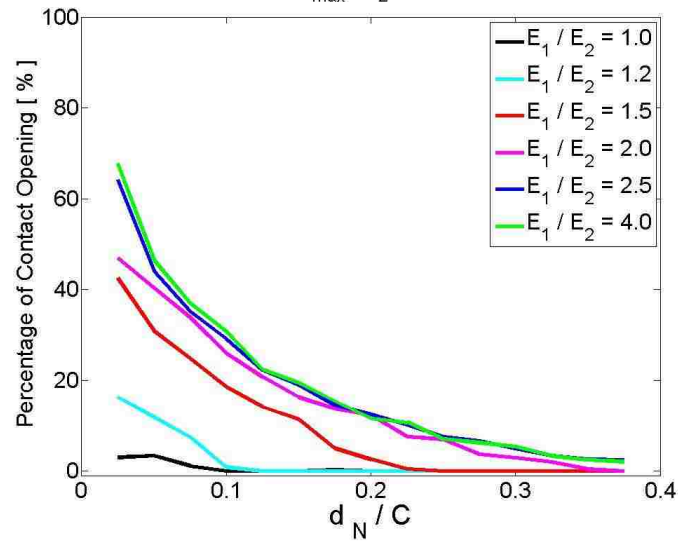




Figure 4.11 (a) 3-D surface plots of contact opening percentage as a function of the normalized friction stress (τ_{max}) and normalized indenter displacement for four modulus ratios ($E_2/E_1 = 1.0, 1.5, 2.5$ & 4.0). Evidently, when $E_1 = E_2$, there is only a little contact opening due to tension at the contact edge. For larger modulus ratio ($> \sim 2.0$), the fraction of contact area lost is independent of modulus ratio. It increases with increasing shear stress, and decreasing with increasing normal displacement. (b) Fraction of lost contact area as a function of normalized displacement, for $\tau_{max}/E = 0.1$.

4.5 Summary and conclusion

Our principal experimental finding is that a flat surface patterned with spatial variation in stiffness undergoes an auto-roughening phenomenon during frictional sliding against a rigid indenter. As the indenter begins to slide against the material surface, the initially full and simply connected contact area breaks into partial contact. For sufficiently small normal loads, the contact regions can be separated into many fragments resulting in a significant decrease of the real contact area. This contact area reduction results in lower sliding friction, compared to either stiff or compliant controls. The “auto-roughening” phenomenon happens spontaneously and robustly to either 1-D (micro-channel) or 2-D (micro-fibrillar) patterns with spatial variation in stiffness. Even though this effect of contact reduction can be alleviated by increasing the normal load, the overall sliding friction still remains below both flat controls.

A similar “contact opening” effect is captured by finite element simulations, which show that periodic contact gaps are generated automatically during shearing of a flat rigid punch on a flat elastomer with alternating stiff and compliant surface materials. The extent of contact opening depends on frictional stress, elastic modulus mismatch, and normal load. High frictional stress and low normal load favor it. A relatively small mismatch in moduli is sufficient to trigger auto-roughening, as measured by the fraction of area that loses contact. The auto-roughening transition could serve as a useful mechanism for deliberate control and reduction of friction.

4.6 References

- [1] Persson, B. N. J. *Sliding Friction: Physical Principles and Applications* Vol. 1, Springer, Berlin, 2000.
- [2] Moore, D. F. *The Friction and Lubrication of Elastomer* Pergamon: Oxford, 1972.
- [3] Aggarwal, S. L.; Fabris, H. J.; Hargis, I. G.; Livigni, R. A. *Polym. Prepr. (Am. Chem. Soc., Div. Polym. Chem.)* **1985**, 26, 3.
- [4] Heinrich, G.; Klüppel, M. *Wear* **2008**, 265, 1052-1060.
- [5] Roberts, A. D. *Rubber Chem. Technol.* **1992**, 65, 673.
- [6] Theodore, A. N.; Samus M. A.; Killgoar, P. C. *Ind. Eng. Chem. Res.* **1992**, 31, 2759.
- [7] Bowden F. P.; Tabor, D. *The friction and lubrication of solids* Vol. 1, Oxford university press: Oxford, 2001.
- [8] Jagota A.; Hui, C-Y. *Materials Science and Engineering R* **2011**, 72, 253-292.
- [9] Sills, S.; Vorvolakos, K.; Chaudhury, M. K.; Overney, R. M. *Nanotribology: Friction and Wear on the Atomic Scale* **2007**, in E. Gnecco and E. Meyer (eds), Springer-Verlag: Heidelberg, Germany, 659-676.
- [10] Schallamach, A. *Wear* **1963**, 6, 375-382.
- [11] Ghatak, A.; Vorvolakos, K.; She, H.; Malotky D. L.; Chaudhury, M. K. *J. Phys. Chem. B* **2000**, 104, 4018-4030.
- [12] Homola, A. M.; Israelachvili, J. N.; McGuiggan, P. M.; Hellgeth, J. W. *Wear* **1990**, 136, 65-84.
- [13] Johnson, K. L. *Proceedings of the Royal Society of London. Series A: Mathematical, Physical and Engineering Sciences* **1997**, 453, 163-179.
- [14] Bhushan, B. *Phil.Trans. Roy. Soc. A* **2009**, 367, 1445-1486.
- [15] Creton, C.; Gorb, S. *MRS Bull.* **2007**, 32, 466-472.
- [16] Kamperman, M.; Kroner, E.; del Campo, A.; McMeeking, R. M.; Arzt, E. *Adv. Eng. Mater.* **2010**, 12, 335-348.
- [17] Jagota, A.; Hui, C-Y.; Glassmaker N. J.; Tang, T. *MRS Bull.* **2007**, 32, 492.
- [18] del Campo, A.; Greiner, C.; Arzt, E. *Langmuir* **2007**, 23, 10235-10243.

- [19] Majumder, A.; Sharma, A.; Ghatak, A. *Bio-Inspired Adhesion and Adhesives: Controlling Adhesion by Micro-nano Structuring of Soft Surfaces in Microfluids and Microfabrication* Springer: USA, 2010.
- [20] Kim, S.; Sitti, M. *Appl. Phys. Lett.* **2006**, *89*, 261911-261913.
- [21] Ko, H.; Lee, J.; Schubert, B. E.; Chuah, Y-L.; Leu, P. W.; Fearing, R. S.; Javey, A. *Nano lett.* **2009**, *9*, 2054-2058.
- [22] Lamblet, M.; Verneuil, E.; Vilmin, T.; Buguin, A.; Silberzan, P.; Leger, L. *Langmuir* **2007**, *23*, 6966-6974.
- [23] Shahsavan H.; Zhao, B. *Langmuir* **2011**, *27*, 7732-7742.
- [24] Chan, E. P.; Smith, E. J.; Hayward, R. C.; Crosby, A. J. *Adv. Mater.* **2008**, *20*, 711-716.
- [25] Parness, A.; Soto, D.; Esparza, N.; Gravish, N.; Wilkinson, M.; Autumn, K.; Cutkosky, M. *J. R. Soc. Interface* **2009**, *6*, 1223-1232.
- [26] Glassmaker, N. J.; Jagota, A.; Hui, C-Y.; Noderer, W. L.; Chaudhury, M. K. *Proc Natl. Acad. Sci.* **2007**, *104*, 10786-10791.
- [27] Noderer, W. L.; Shen, L.; Vajpayee, S.; Glassmaker, N. J.; Jagota, A.; Hui, C.-Y. *Proceedings: Mathematical, Physical and Engineering Sciences* **2007**, *463*, 2631-2654.
- [28] Murphy, M. P.; Kim, S.; Sitti, M. *ACS Appl. Mater. Interfaces* **2009**, *1*, 849-855.
- [29] Gorb, S.; Varenberg, M.; Peressadko A.; Tuma, J. *J. R. Soc. Interface* **2007**, *4*, 271-275.
- [30] Majumder, A.; Ghatak, A.; Sharma, A. *Science* **2007**, *318*, 258-261.
- [31] Ghatak, A. *Phys. Rev. E* **2010**, *81*, 021603.
- [32] Guduru P. R.; Bull, C. *J. Mech. Phys. Solid.* **2007**, *55*, 473-488.
- [33] Kendall, K. *Proceedings of the Royal Society of London. A. Mathematical and Physical Sciences* **1975**, *341*, 409-428.
- [34] Varenberg, M.; Gorb, S. N. *Adv. Mater.* **2009**, *21*, 483-486.
- [35] Kim, S.; Aksak, B.; Sitti, M. *Appl. Phys. Lett.* **2007**, *91*, 221913.
- [36] Shen, L.; Jagota, A.; Hui, C-Y. *Langmuir* **2009**, *25*, 2772-2780.

- [37] Vajpayee, S.; Long, R.; Shen, L.; Jagota, A.; Hui, C-Y. *Langmuir* **2009**, *25*, 2765-2771.
- [38] Rand C.; Crosby, A. *J. Appl. Phys.* **2009**, *106*, 064913.
- [39] Singh, A. K.; Bai, Y.; Nadermann, N.; Jagota, A.; Hui, C-Y. *Langmuir* **2012**, *28*, 4213-4222.
- [40] Glassmaker, N. J.; Jagota, A.; Hui, C-Y.; Kim, J. *J. R. Soc. Interface* **2004**, *1*, 23-33.
- [41] Johnson, K. L.; Kendall, K.; Roberts, A. D. *P. Roy. Soc. Lond. A Mat.* **1971**, *324*, 301-313.
- [42] Savkoor, A. R.; Briggs, G. A. D. *Proc. R. Soc. Lond. A* **1977**, *356*, 103-114.
- [43] Nguyen, D. T.; Paolino, P.; Audry, M-C.; Chateauminois, A.; Frétigny, C.; Le Chenadec, Y.; Portigliatti, M.; Barthel, E. *J. Adh.* **2011**, *87*, 235-250.
- [44] Vorvolakos, K.; Chaudhury, M. K. *Langmuir* **2003**, *19*, 6778.

Chapter 5 Enhancement of Friction against a Rough Surface by a Ridge- Channel Surface Microstructure

We report on a study of the sliding friction of elastomeric surfaces patterned with ridges and channels (and unstructured flat controls), against both smooth and roughened spherical indenters. Against the smooth spherical indenter, all of the structured surfaces have highly reduced sliding friction due to the reduction in actual area of contact. Against roughened spherical indenters, however, the sliding force for structured samples can be up to 50% greater than that of an unstructured flat control. The mechanism of enhanced friction against a rough surface is due to a combination of increased actual area of contact, interlocking between roughness and the surface structure, and attendant dynamic instabilities that dissipate energy.

5.1 Introduction

Within the last decade, significant efforts have been made to manipulate surface mechanical properties via design of surface structures¹⁻⁷. Much of this work has been inspired by biological attachment devices of various animals⁸⁻¹¹. Significant advances have been made in demonstrating bio-mimicked structures for controlling adhesion¹²⁻¹⁶ and friction¹⁷⁻¹⁹.

In most reported examples involving elastomeric surfaces, surface structuring reduces sliding friction. For example, highly reduced sliding friction was observed by a structured surfaces consisting of micro-fibrils²⁰, primarily due to decrease in actual contact area. Similarly, a reduction of sliding force was also reported using elastomeric wrinkled surfaces²¹. Recently, we reported an “auto-roughening” transition in which the surface of a nominally flat surface with spatially varying stiffness roughens when shear tractions are applied to its surface. The reduction in contact area due to auto-roughening lead to sliding friction much lower compared to the homogeneous flat control samples²².

The studies cited above all report sliding friction of structured surfaces against a smooth stiff surface. However, surfaces, such as roads, walls, and glass commonly are rough at all length scales. It is thus of considerable interest to study friction between elastomeric materials and rough stiff surfaces, for example to understand friction in tires²³⁻²⁵. Previously, theories of contact mechanics related to surface roughness have been studied broadly, by Persson²⁶⁻²⁹, Johnson³⁰, Hui³¹⁻³³ and Robbins³⁴. From an experimental perspective, Fuller and Tabor³⁵ found that even a small surface roughness with a few microns in amplitude can remove the adhesion completely between a smooth

elastic surface and rigid roughness. However, other experimental work has shown that the work of adhesion initially increases with roughness before decreasing³⁶⁻³⁸. In particular, Guduru has demonstrated the significant adhesion enhancement in pull-off force between a stiff wavy punch and a soft gelatin block³⁹, which is driven by crack-trapping⁴⁰.

Persson first considered the mechanical interaction between the fibrillar structures on surface roughness with application to biological systems^{41,42}. He modeled the surface roughness as a self-affine fractal⁴¹, and analyzed how hierarchical interfacial structures attach and detach a rough substrate. The interaction between roughness and fibrillar interfaces has also been studied by Bhushan⁴³ and Hui³¹. However, there are only a few experimental studies on the mechanical properties of structured surfaces against surface roughness. Vajpayee *et al*⁴⁴ showed that film-terminated fibrillar samples can maintain considerable adhesion against rough surfaces, even when flat surfaces had almost none.

In this work we report on a study of friction of elastomeric surfaces patterned with rows of ridges and channels (and nominally flat, unstructured controls) against smooth and rough indenters. Consistent with previous reports¹⁸⁻²¹, we find that sliding friction of structured surfaces against a smooth indenter is reduced compared to that of an unstructured control due to reduction in actual area of contact. However, in contrast to the smooth stiff indenter, sliding friction of structured surfaces against a rough indenter can be significantly higher compared to an unstructured control, which has not been predicted by any previous theories.

5.2 Experimental methods

5.2.1 Sample preparation

The elastomeric surfaces used in our experiments are fabricated by a replica molding process, following previously described techniques⁴⁵. An elastomer, polydimethylsiloxane (PDMS, Sylgard® 184, Dow Corning) was molded into a series of silicon masters, patterned with parallel micro-channel structures by photolithography. The width of each channel, w , was fixed at 10 μm for the silicon masters, minimum center-to-center spacing, c , was varied as 20, 35, 50 and 65 μm . The channel depth, d , measured by interferometric optical profilometer (ZeGage. Zometrics, Inc), was varied as 13.0, 26.5 and 36.0 μm , Liquid PDMS mixture was made by adding a small amount of curing agent into the silicone elastomer base in a weight ratio of 1:10. The mixture was degassed under vacuum for 30 minutes and then applied onto the silicon masters and cured at 80°C for 2 hours. A standard PDMS sample is 30 mm x 10 mm x 0.61 mm (length, width, and thickness, respectively), with ridged micro-structures that are complementary to the silicon master mold, as shown in Figure 5.1.

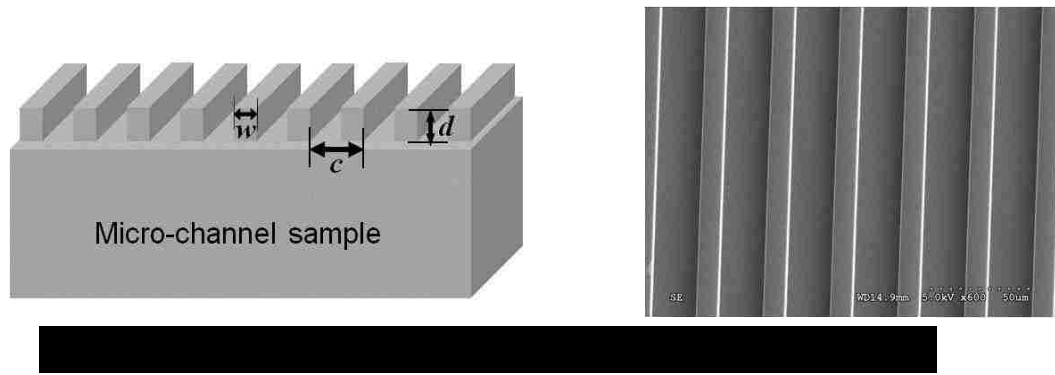


Figure 5.1 (a) Schematic illustration of structured elastomeric samples. All the ridges have the same width $w = 10 \mu\text{m}$, and the channel depth and inter-channel spacing are varied. (b) Scanning electron micrograph of a typical structured surface.

Friction experiments were conducted with two types of indenters. The smooth spherical glass indenter (with a diameter of 6.0 mm) is made by melting one end of a glass rod (2.14 mm in diameter), while slowly rotate the rod at a constant speed using simple lampworking technique. To study the frictional behavior due to random roughness, a roughened spherical glass indenter was used as the testing probe in the friction experiments. A roughened spherical indenter is fabricated by placing a smooth indenter in a commercial rock tumbler (NSI Rock Tumbler Classic kits), and tumbled continuously within a mixture of coarse 60/90 grit silicon carbideⁱ (26 grams) and water for about 24h. This procedure generates an indenter which was nominally spherical with random surface roughness. The final diameter of this roughened indenter is also about 6.0 mm. Characterization of the surface roughness of the roughened indenter was measured by interferometric optical profilometer. Figures. 5.2a and 5.2b present the averaged

ⁱ Coarse grit is a sand-size material and is the most abrasive in a typical rock tumbler kit. It is used in the first step of the tumbling process to round the sharp edges off of the rough. The numbers, such as 60, 90, refer to a particle size (for 60/90 coarse grit, the particles are about 0.25 mm in diameter). They are the opening size, or "mesh" or a standard screen (small numbers refer to larger screen openings or larger particle sizes and large numbers refer to tiny screen openings).⁴⁶

surface profiles of four identical profilometry scannings under the same condition, for both smooth and roughened indenter surfaces, respectively. (Linear interpolation was used for filling small gaps among the scattered points in Figure 5.2a & b.) Figure 5.2c shows the power spectrum of the surface morphology on both smooth and rough indenters, the dimension of the roughness is calculated by the measured height information of each pixel using finite Fourier transform. Note that when the wave length is varied in the range of $\sim 0.16 \mu\text{m}$ to $\sim 100 \mu\text{m}$, the magnitude of surface roughness on the rough indenter is always larger than the smooth indenter, which reveals that the originally smooth indenter is effectively roughened by coarse SiC grit in the tumbler.

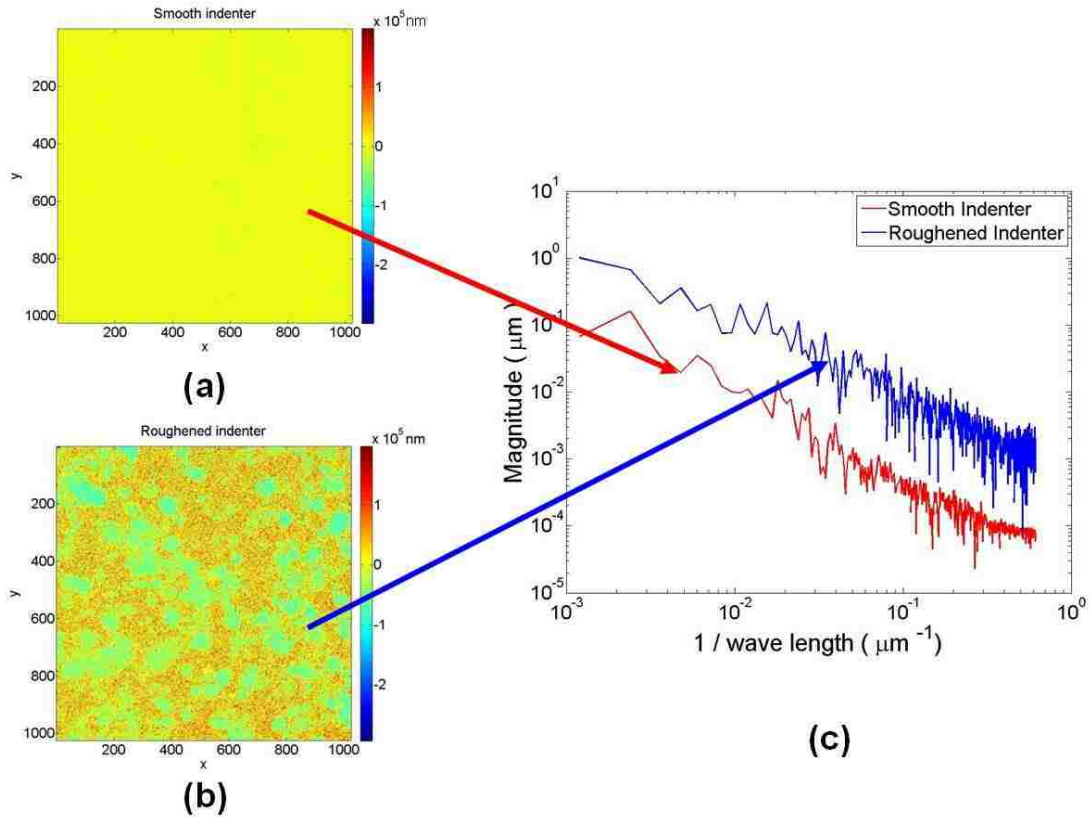


Figure 5.2 Surface morphology of glass surface on roughened spherical indenter, examined by optical profilometer. (a) Image of optical profilometry on the smooth spherical indenter; (b) image of optical profilometry on the surface of glass indenter, roughened by rock tumbler; (c) comparison of the power-spectrum of the roughness on both smooth and rough indenters.

5.2.2 Friction measurement

The experimental apparatus for measuring the frictional force between the spherical glass indenter and the structured samples is shown schematically in Figure 5.3. In the friction experiment, a sample was placed above an inverted optical microscope, and was brought into contact with a glass indenter under a fixed normal load (more detailed descriptions of the friction measurement apparatus are included in previous work^{47,48}). The elastomeric sample was attached to a glass slide, which was driven by a

variable speed motor (Newport ESP MFA-CC) via a motion controller (Newport ESP300) at a fixed velocity ($u = 10 \mu\text{m/s}$). The frictional force was measured by a load cell (Honeywell Precision Miniature Load Cell) attached on the balance arm parallel to the direction of sample motion.

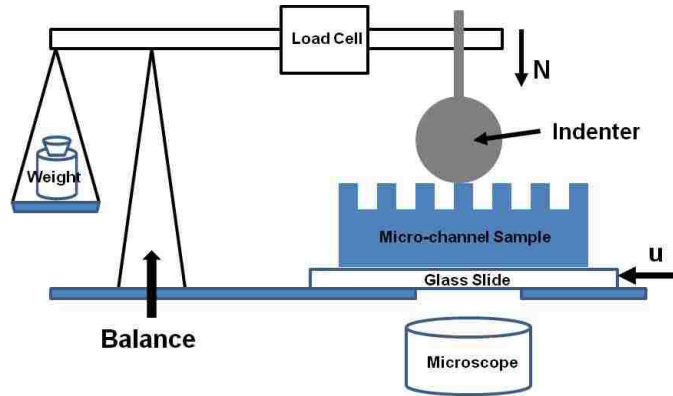


Figure 5.3 Schematic illustration of the apparatus used for friction tests (side view). A glass indenter was attached to a mechanical balance (Ohaus 310D), and rested on the sample with a fixed normal load (N). The sample was attached to a transparent glass slide, which was moved in the horizontal direction by a motor with fixed velocity, $u = 10 \mu\text{m/s}$. Frictional force was measured by a strain-gauge-based load cell fixed on the balance.

5.3 Results

5.3.1 Smooth indenter

Friction tests were carried out with smooth spherical indenter sliding against both micro-channel based PDMS surfaces and the flat control. Figures 5.4 a ~ e show five optical micrographs of the contact area (darker region) between the smooth indenter and two samples: unstructured flat control (Figures 5.4 a,b) and structured samples (Figures 5.4 c,d,e) with channel depth $d = 36.0 \mu\text{m}$ and center-to-center inter-channel spacing $c =$

35 μm). Figure 5.4f shows plots of typical force-displacement data under a fixed normal load $N = 48 \text{ mN}$.

In the unstructured control samples, a circular contact is established (Figure 5.4a) when the smooth indenter initially contacts the PDMS surface and before the application of shear displacement. As the sample is sheared relative to the indenter, the contact area shrinks and become oval during the sliding phase, as shown in Figure 5.4b. The corresponding frictional force is shown by the black line in Figure 5.4f. Figure 5.4f also shows the measured force-displacement response for four structured samples with varying spacing, c . All four structured samples exhibit much lower sliding friction than the flat control. For the samples with relatively small inter-channel spacing ($c = 20, 35$ & $50 \mu\text{m}$), the shear force initially decreases with shear displacement, reaches a minimum value and then increases until the sliding phase is reached (see insert in Figure 5.4f for $c = 35 \mu\text{m}$), similar results are observed previously for a smooth indenter sliding against arrays of micro-scale fibrils²⁰.

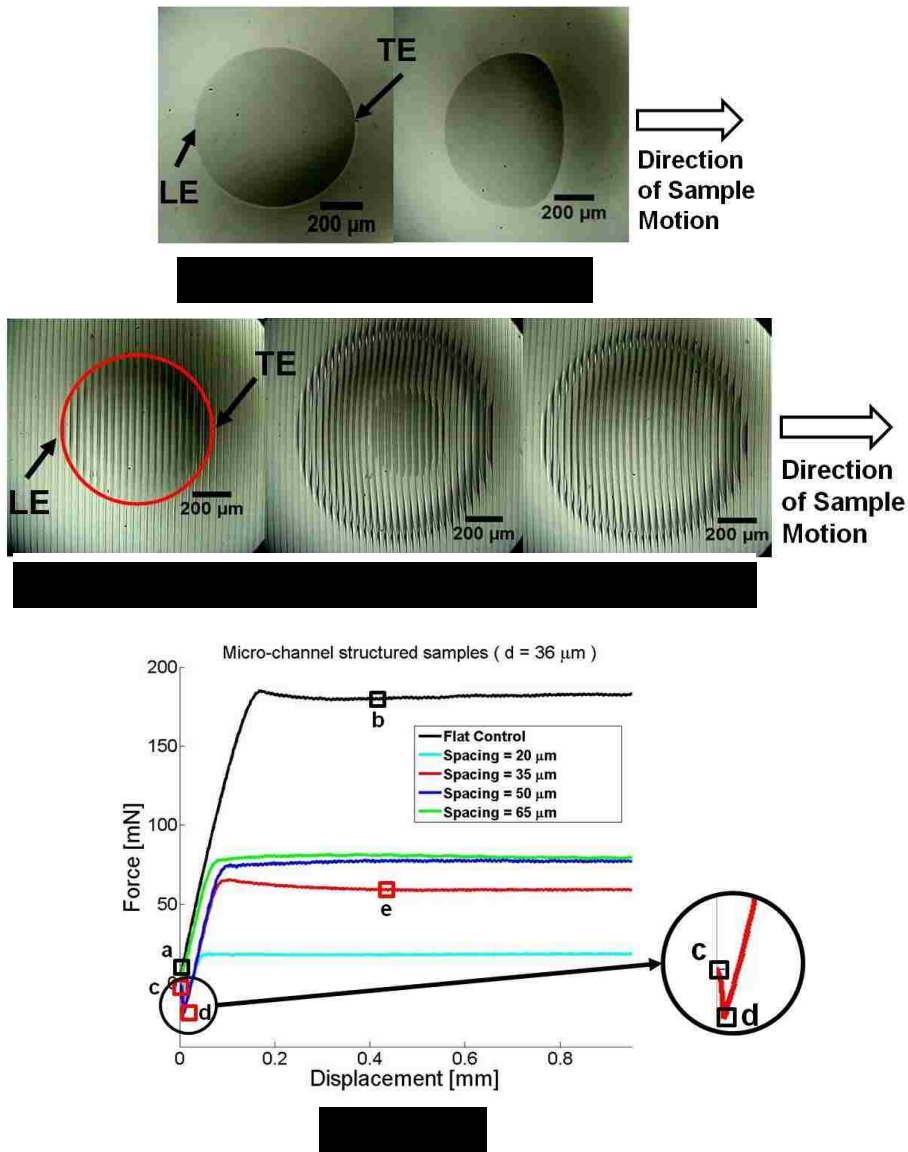


Figure 5.4 (a) ~ (e): Optical micrographs of flat control and micro-channel structured samples under shear by a smooth spherical indenter. The letters ‘LE’ and ‘TE’ denote the leading and trailing edge of the contact, respectively. Flat control sample: (a) initial contact area before shear, (b) contact area during sliding; micro-channel based sample, with channel depth $d = 36 \mu\text{m}$ and inter-channel spacing, $c = 35 \mu\text{m}$: (c) initial contact area before shear, (d) contact region with collapsed region in the center, and (e) contact region during sliding. Labels a-e correspond to points labeled in Figure 5.4f. (f) Typical force-displacement response of a smooth spherical indenter (normal load, $N = 48 \text{ mN}$). The insert is showing that the shear force initially decreases to a minimum value and then increases for micro-channel sample with spacing, $c = 35 \mu\text{m}$.

A sequence of images of one sample ($d = 36.0 \mu\text{m}$, $c = 35 \mu\text{m}$) is shown in Figure 5.4c ~ e. The labels (a ~ e) correspond to the points on the force-displacement curves in Figure 5.4f. Figure 5.4c is the optical micrograph showing initial contact area on the structured sample before application of shear. The contact perimeter is nearly circular and the red line encircles the initial contact region. As shear is applied, the normal compliance of the fibrils decreases and the ridges begin to buckle⁴⁹, shedding load to neighboring ridges, which leads to an expansion of the contact region. This results in the initial decrease of shear force from c to d on the red curve in Figure 5.4f. In a central region, the ridges collapse and touch the backing material, represented by the darker region in Figure 5.4d. Like the initial buckling of the fibrils shown in Ref. (20), these ridges try to recover from buckling state by releasing elastic energy, which performs work on the loading machine. Figure 5.4e shows that the collapsed center region in Figure 5.4d recovers during sliding. For this case, buckling nucleates at the leading edge and the ridges recover fully at the trailing edge, resulting in a constant sliding friction. It should be noted that this phenomenon varies somewhat from sample to sample, and depends on how much normal load is applied. For example, we observe no initial decrease of shear force for spacing, $c = 65 \mu\text{m}$, because the ridges were already buckled and collapsed during initial contact without shear.

5.3.2 Roughened indenter

Figures 5.5a ~ d show optical micrographs of contact area (darker region) between the roughened indenter and test samples (Figure 5.5a,b: flat control; Figure

5.5c,d: micro-channel structured sample with channel depth $d = 36.0 \mu\text{m}$ and center-to-center inter-channel spacing $c = 35 \mu\text{m}$). Figure 5.5e shows corresponding force-displacement curves under the same normal load ($N = 48 \text{ mN}$) as in Figure 5.4. Unlike the smooth indenter, the contact area (Figure 5.5a) is highly irregular. Figure 5.5b shows that, for the unstructured flat control sample, the contact region during sliding remains largely unchanged compared to the initial contact. The sliding friction on the unstructured flat control sample is about 40 mN (black line in Figure 5.5e) and is significantly less than its value against the smooth spherical indenter with identical diameter (about 180 mN, as shown in Figure 5.4f) for the same normal load. This is primarily because the actual contact area is greatly reduced by the surface roughness.

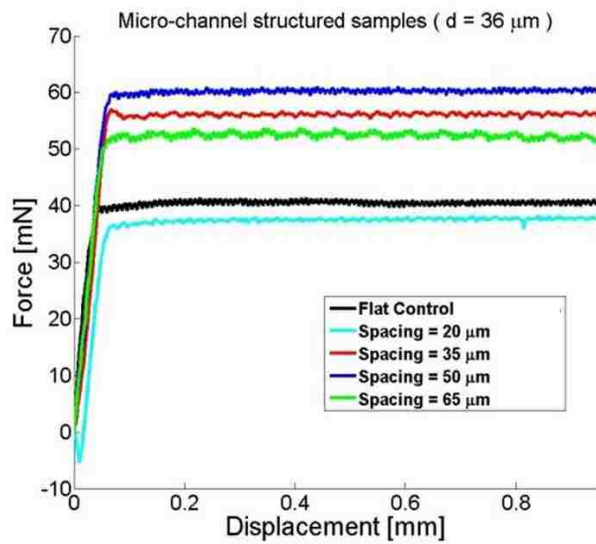
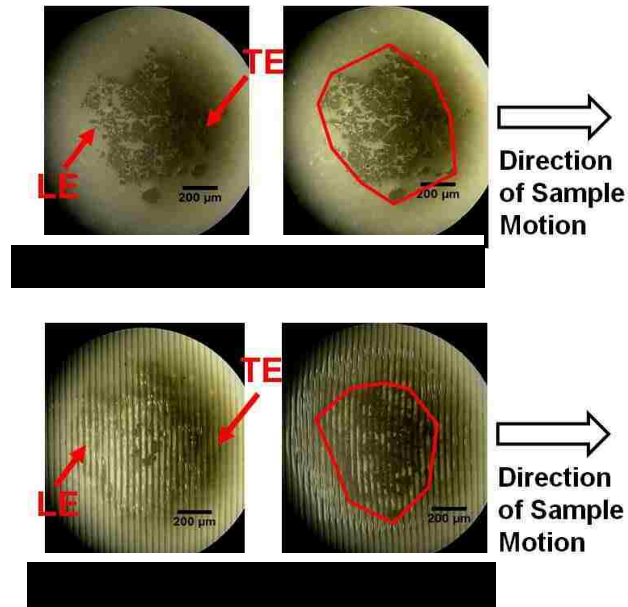


Figure 5.5 (a) ~ (d): Optical micrographs of flat control and micro-channel structured samples under shear by the roughened spherical indenter, the letters ‘LE’ and ‘TE’ denote the leading and trailing edge of the contact, respectively. Flat control sample: (a) initial contact area before shear, (b) contact area during sliding; micro-channel based sample, with channel depth, $d = 36 \mu\text{m}$ and inter-channel spacing, $c = 35 \mu\text{m}$ (normal load, $N = 48 \text{ mN}$): (c) initial contact area before shear, (d) contact region during sliding. The red polygons in (b) and (d) represent the convex hull of real contact area during sliding, respectively on flat control sample and micro-channel sample. (f) Typical force-displacement curves of roughened spherical indenter sliding against micro-channel structured surfaces (same depth, different spacing), compared to the flat control (normal load = 48 mN).

Interestingly, in Figure 5.5e, structured samples with relatively large spacing ($c = 35, 50$ and $65 \mu\text{m}$) have larger sliding friction than the flat control. Figure 5.5c and 5.5d are images taken at the contacting surfaces between the rough indenter and the structured sample before and during sliding (for this case, the sample has channel depth $d = 36 \mu\text{m}$ and inter-channel spacing $c = 35 \mu\text{m}$, and the experiment was carried out under normal load, $N = 48 \text{ mN}$). When only normal compression is applied on the roughened indenter (Figure 5.5c), several segments of darker regions in the center can be observed. It appears that surface roughness on the indenter can penetrate into the gaps between neighboring ridges and make contact with the flat regions and sides of the ridges. Hence, contact is made not only on top of the structured surface, but also within the channel grooves. Once the roughened indenter starts to shear, the ridges in contact bend and buckle, and quickly expand the contact region. The perimeter of buckled area can be observed easily from Figure 5.5d. The red polygon drawn in Figure 5.5d encircles the convex hull^j of real contact area at the interface. In a larger region outside the contact the ridges are bent by the shear forces transmitted by the thin film. The real area of contact, represented approximately by the darker regions within the closed polygon, increases under shear (compared to Figure 5.5c to Figure 5.5d).

5.3.3 Influence of normal load and geometry

A series of friction tests were carried out on micro-channel samples with variation in both depths and inter-channel spacing, using four different normal loads. In Figure 5.6,

^j The convex hull of a planar set is the minimum-area convex polygon that contains the planar set⁵⁰. In this work, the vertices of a convex hull are determined by the real contact regions at the interface.

sliding friction of micro-channel samples is normalized by that of the flat control for each fixed normal load. The data points connected by dashed lines and solid lines represent the normalized sliding friction $F_{structure} / F_{control}$ using the smooth indenter and roughened indenter, respectively. The error bars represent the standard deviation of four different measurements on the same sample subjected to the same normal force.

Figure 5.6 shows that the sliding friction of all the micro-channel structured samples is much smaller than the flat control ($F_{structure} / F_{control} < 1$), using a smooth indenter. We can also notice that: (1) the sliding friction of micro-channel samples with largest depth (tallest ridges) is apparently larger than the shorter ones with the same inter-channel spacing; (2) when a small normal load is applied (e.g. $N = 16 \text{ mN}$), the sliding friction increases significantly for higher ridges and larger spacing. However, when the normal load is large enough ($N = 32, 48 \text{ and } 64 \text{ mN}$ in Figure 5.6), the friction force does not increase so dramatically with channel depth and spacing. It is also noticed that the channel depth has little effect on sliding friction for samples with inter-channel spacing $c = 20 \mu\text{m}$. Specifically, the normalized sliding friction $F_{structure} / F_{control}$ of all such samples are quite similar, we conjecture that when the ridges are sufficiently close to each other, the bending of ridges are sufficiently restricted, so that the smooth indenter would slide on the edge of each contacting ridge which significantly minimize the real contact area at the interface. As a result, the actual contact areas of these small spacing samples remain approximately the same and much smaller under the same normal load.

In contrast to the smooth indenter, we notice that the sliding friction of structured samples with relatively larger spacing ($c = 35, 50 \text{ and } 65 \mu\text{m}$) is significantly larger than

that of the flat control ($F_{structure}/F_{control} > 1$), using the roughened indenter. (The smallest inter-channel spacing, $c = 20 \mu m$, still has a slightly lower friction than the control.) There appears to be an optimal spacing (35 and 50 μm) for enhanced sliding friction. For a fixed spacing, sliding friction increases with larger ridge depth. The maximum normalized sliding friction ($F_{structure}/F_{control} \approx 1.5$) is achieved by sample with 36.0 μm channel depth and 50 μm spacing, under normal load $N = 48 mN$, showing that the enhancement of sliding friction might be controlled and optimized by micro-channel surface designs and normal load.

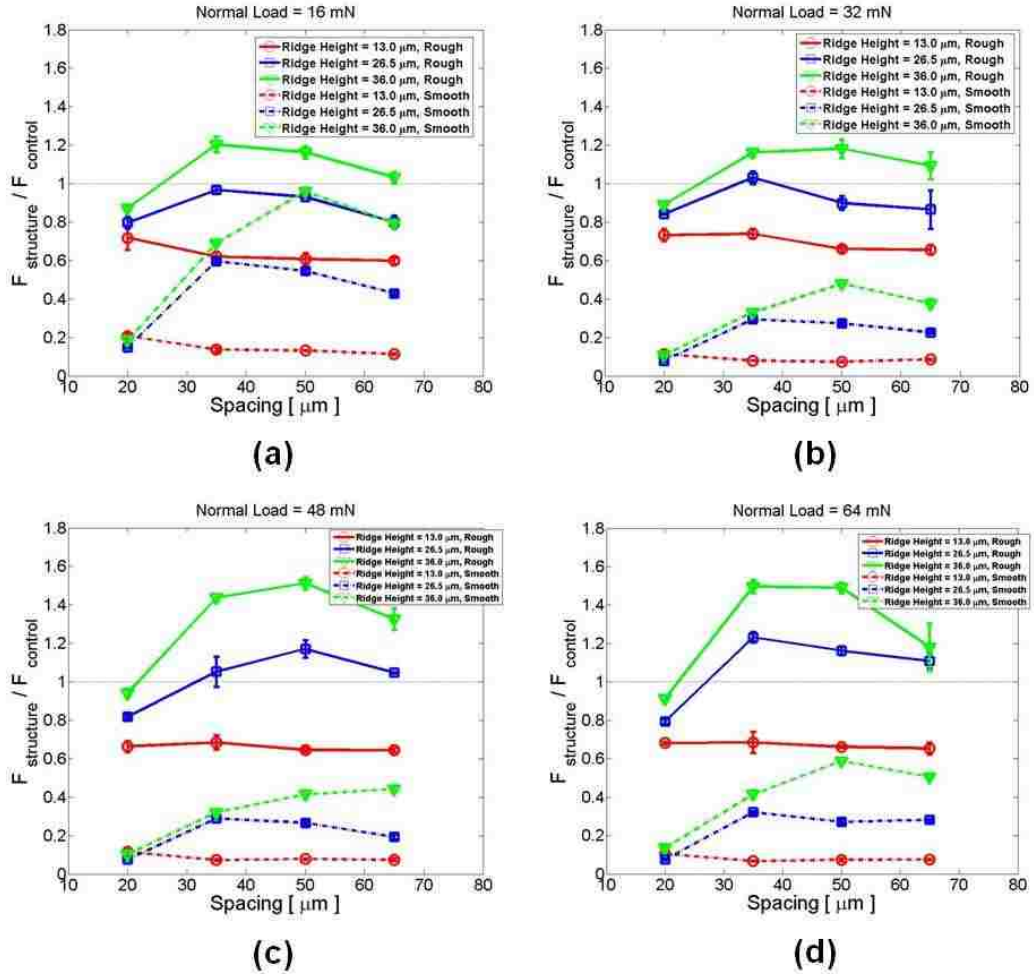


Figure 5.6 Comparison of sliding friction on micro-channel based samples using smooth (dashed lines) and roughened (solid lines) indenters, normalized by the sliding friction of a flat control sample. In each plot, different colors represent different channel depth: red – $d = 13.0 \mu\text{m}$; blue – $d = 26.5 \mu\text{m}$; green – $d = 36.0 \mu\text{m}$. All samples were tested under four different normal loads: (a) $N = 16 \text{ mN}$; (b) $N = 32 \text{ mN}$; (c) $N = 48 \text{ mN}$; (d) $N = 64 \text{ mN}$.

5.3.4 Apparent and real shear stress

To investigate the mechanism for friction enhancement, it is useful to normalize the measured friction force by the area of contact. For a fixed normal load the contact area changes because (a) the effective compliance of the samples varies with channel depth and spacing, as well as the amount of shear, and (b) the actual area of contact

depends on the severity of buckling of the ridges and inter-penetration due to the surface roughness on both sides. We define two contact areas. One, an “apparent” contact area, is defined as the area enclosed by the convex hull of all the combined contact regions. The second is the actual, or “real”, contact area, as determined by the area of the dark regions in the same optical micrographs.

Figure 5.7 shows both apparent shear stress (Figure 5.7a and 5.7c) and real shear stress (Figure 5.7b and 5.7d) using the roughened indenter and three different normal loads ($N = 32, 48 \text{ and } 64 \text{ mN}$). The ratio apparent / real shear stress during sliding motion is calculated by dividing the sliding force by the apparent / real contact area. For each experiment, we randomly chose five images during the sliding phase, and measured the apparent / real contact area. The apparent contact area is measured by the convex hull of all the contact regions at the interface, as marked by the red closed polygon in Figures 5.5b and 5.5d. The real contact area is calculated by the number of pixels within adjusted threshold of intensities for the dark regions, and then converted into actual areas. The mean apparent / real shear stress and its variance were calculated as the ratio of average sliding friction (averaged by the five randomly picked values in the sliding phase) and the average apparent / real contact area, corrected using the approximation given in Appendix D. The error bars shown in Figure 5.7 represent the standard deviation (i.e. square root of corresponding variance) of the apparent / real shear stresses.

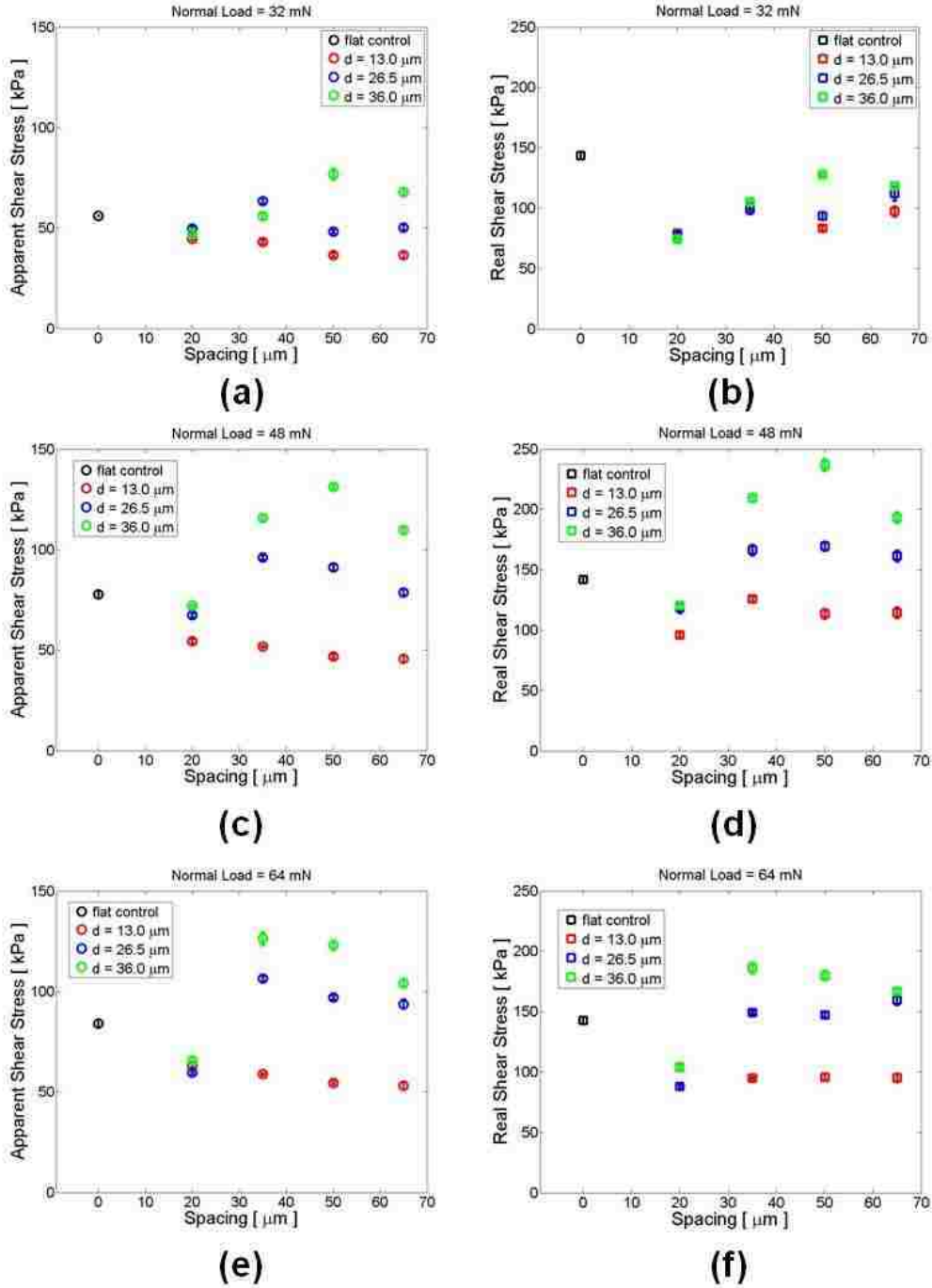


Figure 5.7 Apparent shear stress (a,c,e) and real shear stress (b,d,f) of micro-channel samples sliding against the roughened indenter, compared to a flat control. The colors of data points denote the different channel depth: red – $d = 13.0 \mu\text{m}$; blue – $d = 26.5 \mu\text{m}$; green – $d = 36.0 \mu\text{m}$. The samples are sheared under three different normal loads: (a,b) $N = 16 \text{ mN}$; (c,d) $N = 32 \text{ mN}$; (e,f) $N = 48 \text{ mN}$.

From Figure 5.7, we notice that, for a flat control sample, although the apparent shear stress varies with the normal load, the corresponding real shear stress remains substantially unchanged (~ 140 kPa), and its value is reasonably close the shear stress (~ 200 kPa) on flat PDMS against a rough glass lens, reported by Chateauminois and Fretigny⁵¹. Figures 5.7a and 5.7b show that, when a relatively small normal force is applied ($N = 32$ mN), there is much less enhancement in the apparent shear stress for samples with larger depth and wider spacing (e.g. data point corresponds to $d = 36.0$ μm and $c = 50$ μm) than the larger normal loads, since the real shear stress for all the structured samples is smaller than the flat control. However, for larger normal loads (Figures 5.7c ~ f), we find that both apparent and real shear stresses are increased by such roughened surface shearing against the micro-channel surface with higher ridges and larger spacing, mechanisms other than the increased effective compliance must contribute to such highly enhanced sliding friction.

Two possible dynamic instabilities can explain the enhancement of sliding friction by surface roughness. First, the sliding friction can be increased by elastic energy released for recovering the original shape of the micro-channels (ridges) from bending and buckling under shear. Second, when the normal load is large enough, the ridges might collapse onto their neighboring ones or the horizontal flat regions between two neighboring ridges (when $d < c - w$), the roughness would make contact on side of the ridges and increase in frictional (adhesion) energy, including the extra work of adhesion due to “interlocking”, i.e., the inter-penetration between the rigid roughness and the channel grooves. Due to the variety of different experimental conditions, we tried to

understand the frictional behavior for three typical cases by varying the dimensions of micro-patterns on elastomeric surfaces, according to the apparent and real shear stress results in Figure 5.7 and the experimental observations:

a) Small inter-channel spacing ($c = 20 \mu\text{m}$)

For a micro-channel structured surface with inter-channel spacing, $c = 20 \mu\text{m}$, one might expect that the sliding friction would be reduced by 50% while the smooth indenter only make real contact on top of the ridges. In Figure 5.6, it is obvious that sliding friction remains approximately the same for samples with $20 \mu\text{m}$ inter-channel spacing, when using the *smooth* indenter and same normal load. However, the sliding friction decreases dramatically compared to its corresponding flat featureless control, $F_{structure} / F_{control} = 0.1 \sim 0.2$, even though the channel depths are different. Bending effect on contacting ridges can be observed once start to shear, which leads to an expansion of apparent contact area shown in Figure 5.4. As illustrated in Figure 5.8a and 5.8b, the curved smooth surface only makes contact on the edges of bent ridges, which results in a highly reduced real contact area.

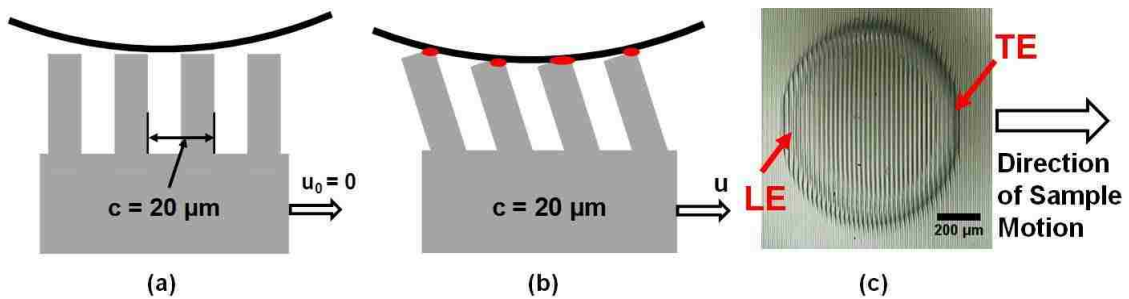


Figure 5.8 Typical contact region between the smooth indenter and micro-channel based surface with spacing, $c = 20 \mu\text{m}$: (a) schematic drawing of initial contact without shear (side view); (b) schematic drawing during sliding phase (side view), the small red ellipses mark the possible real contact regions; (c) optical micrograph of the contacting area under shear (micro-channel sample: $d = 26.5 \mu\text{m}$, $c = 20 \mu\text{m}$; normal load, $N = 48 \text{mN}$).

Significant enhancement of frictional resistance can be achieved by micro-channel surface shearing against the roughened indenter, even though the sliding friction is still slightly smaller than the unstructured flat control. As illustrated in Figure 5.9a and 5.9b, the local bending effect is varied by the introduced random surface roughness from the indenter (which can be observed by the irregular darker regions in Figure 5.9c). During the sliding phase, some of the larger-sized roughness is able to make contact on top of the ridges. At the mean time, many of the small-sized roughness from the indenter side, which can be viewed as small particle on the surface (the radius of each particle, $R_a < 10 \mu m$), can help increase the real contact area by making extra contact on either the edge or side of the ridges, due to bending and buckling of the ridges. The real contact area increases in form of small segments, which results in a larger sliding friction, compared to the smooth indenter. From Figure 5.6, we also notice that the sliding friction on samples with 20 μm spacing increases with the channel depth, since the taller ridges are easier to be bend or buckled, and with more possibility to make contact with the surface roughness.

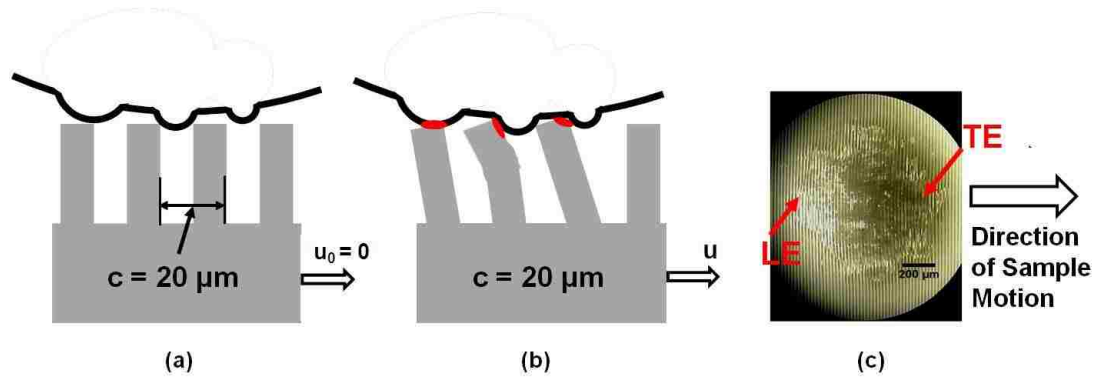


Figure 5.9 Typical contact region between the randomly rough surface and micro-channel based surface with spacing, $c = 20 \mu\text{m}$: (a) schematic drawing of initial contact (side view); (b) schematic drawing during sliding phase (side view), the small red ellipses mark the possible real contact regions; (c) optical micrograph of the contacting area under shear (micro-channel sample: $d = 36.0 \mu\text{m}$, $c = 20 \mu\text{m}$; normal load, $N = 48 \text{ mN}$).

b) Small channel depth ($d = 13.0 \mu\text{m}$)

Figure 5.6 and 5.7 show that the lowest sliding friction and shear stresses are observed with samples having the smallest channel depth ($d = 13.0 \mu\text{m}$). In addition, these sliding frictions are approximately independent of the inter-channel spacing. In Figure 5.6, it is noticed the sliding friction by the smooth indenter reduces significantly ($F_{structure} / F_{control} = 0.05 \sim 0.2$), however, the loss of frictional force is compensated by introducing the surface roughness (roughened indenter, $F_{structure} / F_{control} = 0.6 \sim 0.75$), compared to the corresponding unstructured flat control.

According to Euler buckling theory, it is known that pillars with lower aspect ratio buckle at higher stress, that is why we do not observe severe buckling effect on the contacting ridges (the width of each ridge is fixed, $w = 10 \mu\text{m}$, so the aspect ratio d / w depends only on the channel depth, d). As shown in Figure 5.10c, a small amount of bending is observed in all the samples with the smallest ridge height (channel depth).

Similar to the previous case ($c = 20 \mu\text{m}$), the smooth indenter can only make contact on the edges of the short ridges, which leads to a dramatically reduced sliding friction (as shown in Figure 5.10).

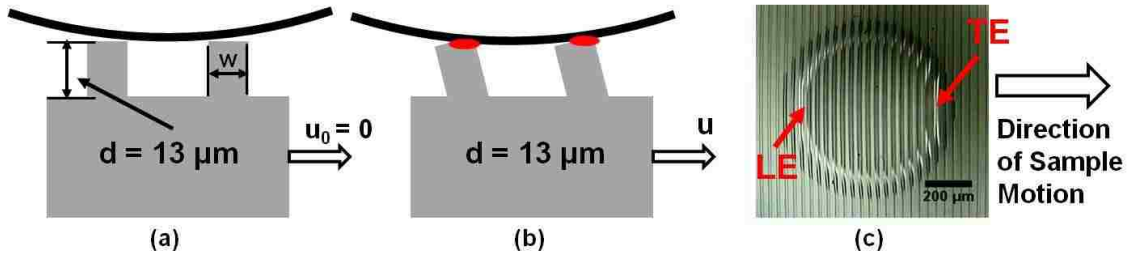


Figure 5.10 Typical contact region between the smooth indenter and micro-channel based surface with channel depth, $d = 13.0 \mu\text{m}$: (a) schematic drawing of initial contact without shear (side view); (b) schematic drawing during sliding phase (side view), the small red ellipses mark the possible real contact regions; (c) optical micrograph of the contacting area under shear (micro-channel sample: $d = 13.0 \mu\text{m}$, $c = 35 \mu\text{m}$; normal load, $N = 48 \text{ mN}$).

The influence of bending and buckling effect is also restricted by the small channel depth when using the roughened indenter, even though the surface roughness can still generate more contact area on side of ridges which helps alleviate the reduction in sliding friction, as illustrated in Figure 5.11b. As shown in the experiments (Figure 5.11c), the rough surface makes more real contact area on the side of bent structures, compared to the smooth indenter (Figure 5.10c). The reason why the frictional force (and stress) does not change much with the interchannel spacing is not clear yet. Since the amplitude (height) of structures is small, and the influence of bending effect is minimized, we conjecture that the normal load, as well as the geometry of the stiff surface plays a major role in sliding frictional behavior.

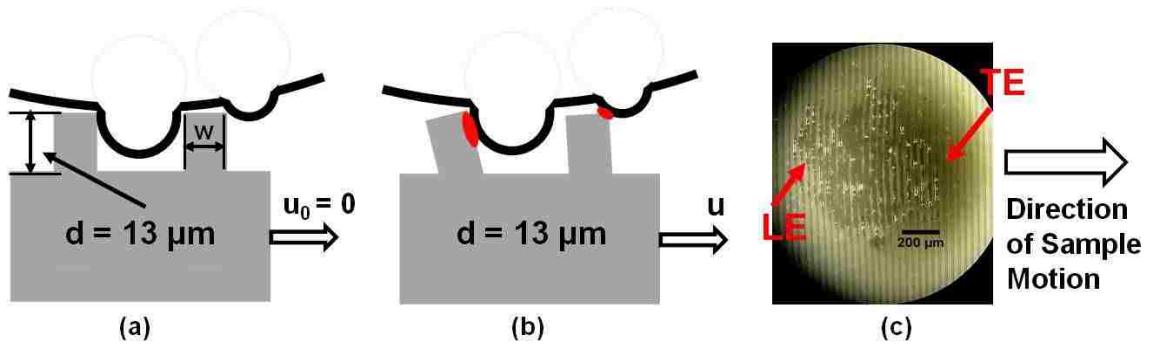


Figure 5.11 Typical contact region between the randomly rough surface and micro-channel based surface with channel depth, $d = 13.0 \mu\text{m}$: (a) schematic drawing of initial contact (side view); (b) schematic drawing during sliding phase (side view), the red ellipses mark the possible real contact regions; (c) optical micrograph of the contacting area under shear (micro-channel sample: $d = 13.0 \mu\text{m}$, $c = 35 \mu\text{m}$; normal load, $N = 48 \text{ mN}$).

c) Samples with large channel depth and inter-channel spacing

Interestingly, when both channel depth and spacing are large enough, both the apparent and real shear stresses increase significantly, especially with increased normal load. From Figure 5.7c ~ f, we notice that for all the samples with channel depth, $d = 26.5, 36.0 \mu\text{m}$ and the inter-channel spacing, $c = 35, 50 \text{ and } 65 \mu\text{m}$, both calculated shear stresses are much larger than the flat control (normal load, $N = 48 \text{ and } 64 \text{ mN}$), the real shear stress can even reach about 250 kPa under certain conditions (see Figure 5.7d). Under such conditions, ridge deflection can be very large, on the order of channel depth (ridge height). As we could observe from the interfacial contact area during sliding phase (Figure 5.5d), the ridges were strongly compressed and collapsed under shear and large normal load, as illustrated in Figure 5.12. The micro-structures could undergo much severe bending and buckling driven by the stiff roughness in large range of sizes (Region ‘A’: illustrated in Figure 5.12b and experimental image Figure 5.12d), or the roughness could penetrate into the grooves of channels and make larger contact (and adhesion) on

the horizontal backing regions between neighboring ridges (Region ‘B’: illustrated in Figure 5.12b and experimental image Figure 5.12d). Compare to the previous two micro-channel designs, taller ridges and wider spacing strengthen the capability of dynamic instabilities, it is possible that not only the bending and buckling help increasing the frictional energy, but also mechanical “interlocking” between the surface roughness and micro-channels could contribute to enhance the effective adhesion at the interface, and spontaneously relates to the increased friction.

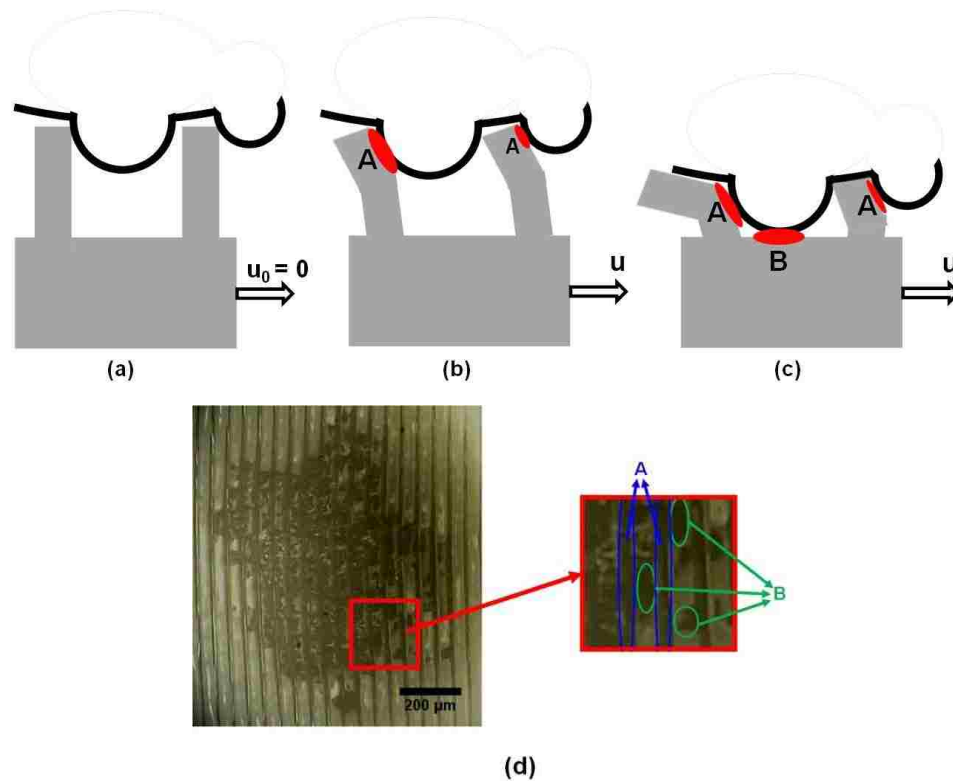


Figure 5.12 (a) ~ (c): Schematic illustration of contact region between the randomly rough surface and micro-channel based surface with large depth and inter-channel spacing (side view), the red ellipses mark the possible real contact regions: (a) initial contact; (b) possible deformation of buckled ridges in contact region during sliding phase; (c) possible deformation of collapsed ridges in contact due to large normal compression. (d) Optical micrograph of the contacting area under shear (micro-channel sample: $d = 36.0 \mu\text{m}$, $c = 50 \mu\text{m}$; normal load, $N = 48 \text{ mN}$). Region marked ‘A’: contact area on side of ridges; Region marked ‘B’: contact area on interval regions between neighboring ridges (“interlocking”).

5.4 Discussion and summary

In this chapter, we have examined the frictional behavior of micro-channel based surfaces against both smooth spherical indenter and manipulated round indenter with random roughness on the surface. The friction tests by smooth indenter show a significantly reduced sliding friction, compared to the flat control. The easily visualized partial contact area plays a dominant role in the reduction in sliding friction, due to the highly decreased in real contact area. However, we also observe a buckling effect of the contacting ridges. Sliding friction of samples increases with channel depth, since the effective frictional energy can be restore a little possibly by elastic energy released from buckling.

However, the friction tests can exhibit an enhanced sliding friction of a micro-channel sample with relatively large depth and spacing, using the indenter with random roughness, compared to a flat control sample, especially under large normal load. Within the interfacial contacting area, the ridges might be severely buckled, or even collapsed, due to the normal force and lateral shear force. This work provides a promising approach to control the frictional behavior against a rough surface via elastic topographic surfaces, which has a great potential in future tire design.

5.5 References

- [1] Jagota, A.; Hui, C-Y. *Materials Science and Engineering R* **2011**, 72, 253-292.
- [2] Kamperman, M.; Kroner, E.; del Campo, A.; McMeeking, R. M.; Arzt, E. *Adv. Eng. Mater.* **2010**, 12, 335-348.

- [3] Boesel, L. F.; Greiner, C.; Arzt, E.; del Campo, A. *Adv. Mater.* **2010**, *22*, 2125-2137.
- [4] Reddy, S.; Arzt, E.; del Campo, A. *Adv. Mater.* **2007**, *19*, 3833-3837.
- [5] Jagota, A.; Hui, C-Y.; Glassmaker, N. J.; Tang, T. *MRS Bull.* **2007**, *32*, 492.
- [6] del Campo, A.; Greiner, C.; Arzt, E. *Langmuir* **2007**, *23*, 10235-10243.
- [7] Majumder, A.; Sharma, A.; Ghatak, A. *Bio-Inspired Adhesion and Adhesives: Controlling Adhesion by Micro-nano Structuring of Soft Surfaces in Microfluids and Microfabrication* Springer: USA, 2010.
- [8] Autumn, K. *Am. Sci.* **2006**, *94*, 124.
- [9] Eisner T.; Aneshansley, D. J. *Proc. Natl. Acad. Sci.* **2000**, *97*, 6568-6573.
- [10] Jon Barnes, W. *MRS Bull.* **2007**, *32*, 479-485.
- [11] Arzt, E.; Gorb, S.; Spolenak, R. *Proc. Natl. Acad. Sci.* **2003**, *100*, 10603-10606.
- [12] Glassmaker, N. J.; Jagota, A.; Hui, C-Y.; Noderer, W. L.; Chaudhury, M. K. *Proc Natl. Acad. Sci.* **2007**, *104*, 10786-10791.
- [13] Noderer, W. L.; Shen, L.; Vajpayee, S.; Glassmaker, N. J.; Jagota, A.; Hui, C-Y. *Proceedings: Mathematical, Physical and Engineering Sciences* **2007**, *463*, 2631-2654.
- [14] Gorb, S.; Varenberg, M.; Peressadko, A.; Tuma, J. *J. R. Soc. Interface* **2007**, *4*, 271-275.
- [15] Majumder, A.; Ghatak, A.; Sharma, A. *Science* **2007**, *318*, 258-261.
- [16] Kim, S.; Sitti, M. *Appl. Phys. Lett.* **2006**, *89*, 121905.
- [17] Majidi, C.; Groff, R. E.; Maeno, Y.; Schubert, B.; Baek, S.; Bush, B.; Maboudian, R.; Gravish, N.; Wilkinson, M.; Autumn, K.; Fearing, R. S. *Phys. Rev. Lett.* **2006**, *97*, 076103-076107.
- [18] Varenberg, M.; Gorb, S. *J. R. Soc. Interface* **2007**, *4*, 721-725.
- [19] Kim, S.; Aksak, B.; Sitti, M. *Appl. Phys. Lett.* **2007**, *91*, 221913.
- [20] Shen, L.; Jagota, A.; Hui, C-Y. *Langmuir* **2009**, *25*, 2772-2780.
- [21] Rand, C.; Crosby, A. *J. Appl. Phys.* **2009**, *106*, 064913.
- [22] Bai, Y.; Jagota, A.; Hui, C-Y. *Submitted to Soft Matter* **2013**.
- [23] Moore, D. F. *The Friction and Lubrication of Elastomer* Pergamon:Oxford,1972.

- [24] Aggarwal, S. L.; Fabris, H. J.; Hargis, I. G.; Livigni, R. A. *Polym. Prepr. (Am. Chem. Soc., Div. Polym. Chem.)* **1985**, *26*, 3.
- [25] Heinrich, G.; Klüppel, M. *Wear* **2008**, *265*, 1052-1060.
- [26] Persson, B. N. J. *Surf. Sci. Rep.* **2006**, *61*, 201.
- [27] Persson, B. N. J.; Albohr, O.; Tartaglino, U.; Volokitin, A. I.; Tosatti, E. *J. Phys.: Condens. Matter* **2005**, *17*, R1-R82.
- [28] Persson, B. N. J. *Phys. Rev. Lett.* **2001**, *87*, 116101.
- [29] Peressadko, A. G.; Hosoda, N.; Persson, B. N. J. *Phys. Rev. Lett.* **2005**, *95*, 124301.
- [30] Johnson, K. L. *Int. J. Solids Struct.* **1995**, *32*, 423-430.
- [31] Hui, C-Y.; Glassmaker, N. J.; Jagota, A. *J. Adh.* **2005**, *81*, 699-721.
- [32] Hui, C-Y.; Lin, Y. Y.; Baney, J. M.; Kramer, E. J. *J. Polym. Sci. B. Polym. Phys.* **2001**, *39*, 1196-1214.
- [33] Hui, C-Y.; Lin, Y. Y.; Creton, C. *J. Polym. Sci. Part B. Polym. Phys.* **2002**, *40*, 545-561.
- [34] Akarapu, S.; Sharp, T.; Robbins, M. O. *Phys. Rev. Lett.* **2011**, *106*, 204301.
- [35] Fuller, K. N. G.; Tabor, D. *Proc. Roy. Soc. London A* **1975**, *345*, 327-342.
- [36] Briggs, G. A. D.; Briscoe, B. J. *J. Phys. D: Appl. Phys.* **1977**, *10*, 2453.
- [37] Fuller, K. N. G.; Roberts, A. D. *J. Phys. D: Appl. Phys.* **1981**, *14*, 221-239.
- [38] Kim, H-C.; Russell, T. P. *J. Polym. Sci. Part B: Polym. Phys.* **2001**, *39*, 1848-1854.
- [39] Guduru, P. R.; Bull, C. *J. Mech. Phys. Solids* **2007**, *55*, 473-488.
- [40] Guduru, P. R. *J. Mech. Phys. Solids* **2007**, *55*, 445-472.
- [41] Persson, B. N. J.; Gorb, S. *J. Chem. Phys.* **2003**, *119*, 11437-11444.
- [42] Persson, B. N. J. *MRS Bull.* **2007**, *32*, 486-490.
- [43] Bhushan, B.; Peressadko, A. G.; Kim, T. W. *J. Adh. Sci. technol.* **2006**, *20*, 1475-1491.
- [44] Vajpayee, S.; Jagota, A.; Hui, C-Y. *J. Adhes* **2010**, *86*, 39-61.
- [45] Singh, A. K.; Bai, Y.; Nadermann, N.; Jagota, A.; Hui, C-Y. *Langmuir* **2012**, *28*, 4213-4222.

- [46] <http://geology.com/rock-tumbler/rock-tumbler-grit.shtml>
- [47] Shen, L.; Glassmaker, N. J.; Jagota, A.; Hui, C-Y. *Soft Matt.* **2008**, *4*, 618-625.
- [48] Vajpayee, S.; Long, R.; Shen, L.; Jagota, A.; Hui, C-Y. *Langmuir* **2009**, *25*, 2765-2771.
- [49] Nadermann, N.; Kumar, A.; Goyal, S.; Hui, C-Y. *J. R. Soc. Interface* **2010**, *7*(52), 1581-1589.
- [50] Graham, R. L. *Inform. Process. Lett.* **1972**, *1*, 132-133.
- [51] Chateauminois, A.; Fretigny, C. *Eur. Phys. J. E* **2008**, *27*, 221-227.

Chapter 6 Summary & Conclusions

6.1 Main results

This research presents studies of how near-surface patterning of shape, charge and elasticity can be used to endow generic materials with properties such as adhesion selectivity and controlled friction. The main results are summarized below:

1. Through our theoretical study of surfaces with patterned charge, we showed that strong selectivity can be achieved between two rigid materials. We also predicted that, by allowing the surfaces to deform, e.g. if charges were patterned on elastomeric materials, the selectivity could be effectively reduced and the overall adhesion enhanced.
2. We showed that highly enhanced selective adhesion can be achieved between two complementary surfaces with micro-channel structures, compared to the interface between flat controls. We found that misorientations between structured surfaces are accommodated by interfacial dislocation structures. Adhesion between complementary surfaces is enhanced by crack trapping and friction losses, but attenuated due to the energy released by interfacial dislocations.
3. Surfaces patterned with periodic variation in stiffness undergo an “auto-roughening” transition during friction and this process can significantly attenuate overall sliding friction. This phenomenon can be interpreted as reduction of real contact area, based on the observation that the contact transforms from initially full

contact to partial contact at the interface. A finite element model demonstrates how the generation of contact opening during sliding depends on the elastic mismatch, frictional stress and normal load.

4. We show that the structured elastomeric surfaces usually exhibit highly reduced sliding friction against a smooth surface. However, structured surfaces can have significantly larger friction against a rough surface.

6.2 Ongoing and future work

1. In Chapter 2, we presented a theoretical model to demonstrate the adhesion selectivity between two flat surfaces with charge patterning. However, this idea has not been successfully implemented into experiments. Polyelectrolyte multilayers (PEMs) and the layer-by-layer deposition ¹ technique provide a potential in fabrication of pattern-charged surfaces. The prepared substrate could be imprinted by surface structures, e.g. the micro-channel or fibrillar structures, before depositing the last layer of poly electrolyte. Assembly of multilayer films of the weak polyelectrolytes, poly(acrylic acid) (PAA) and poly(allylamine hydrochloride) (PAH) ², acquire negative and positive charge in a water solution at neutral pH, which could be utilized for generating charge alternates on either rigid surface (e.g. silicon wafer) or elastic materials (e.g. PDMS surface).
2. In Chapter 3, we showed results of adhesion tests between complementary micro-channel surfaces. We also invariably observe defects in the form of visible striations tens to hundreds of microns in width and separated by distances on the

order of mm's. Further study of these defects showed that these striations can be considered as a combination of screw and edge dislocations. Jin *et al*³ showed that the screw dislocations are formed due to the rotational misorientation at the interface, and effectively reduce the work of adhesion. Further investigation need to be implemented for the formation of edge dislocations as well, both experimentally and theoretically. The mechanism of dislocations within elastomeric structured surfaces is also very interesting to study.

3. Appropriate finite element model need to be built for analyzing the mechanism of enhanced sliding friction between micro-channel structures and surface roughness. This FEM result could also help to determine the critical condition that triggers the dynamic instability, and provide suggestions for new structure design according to the dimensions of surface roughness.

6.3 References

- [1] Ariga, K.; Hill, J. P.; Ji, Q. *Phys. Chem. Chem. Phys.* **2007**, 9, 2319-2340.
- [2] Decher, G.; Schlenoff, J. *Multilayer thin films: sequential assembly of nanocomposite materials*, Wiley WCH **2003**, Weinheim.
- [3] Jin, C.; Jagota, A.; Hui, C-Y. *Adv. Funct. Mater.* **2013**, 23, 3453-3462.

Appendices

Appendix A: ^k Model for electrostatic complementarity

Eq. (2.17) in the main text show that the total electrostatic interaction energy and force (per unit area) between two surfaces patterned with stripes of charge are known once we know α , the fraction of area within a unit cell where like charges face each other. Here we consider the family of surfaces defined by $nb=mc$, where n & m are both odd positive integers and $n>m$, b & c are lengths of unit elements on the two sides, and $b<c$. We demonstrate that (a) the strongest electrostatic interaction occurs when the top and bottom surfaces begin with aligned opposite charged regions, and (b) the fraction of area with oppositely charged surfaces is

$$\alpha = \frac{mn-1}{2mn} \tag{A1}$$

We have already shown that if either m or n is even, $\alpha = 1/2$.

Consider a unit cell of length L in which, without loss of generality, the left end is aligned with the start of a negatively charged region on the lower surface. The lower region has m units of length c each. The upper surface is shifted by δ in the positive 'y' direction compared to a configuration in which it begins with a positively charged unit region. We will show that electrostatic attraction is strongest for $\delta=0$. (We need to consider only $\delta<b$).

^k The derivation in this Appendix is provided by Prof. C-Y. Hui at Field of Theoretical and Applied Mechanics at Cornell University.

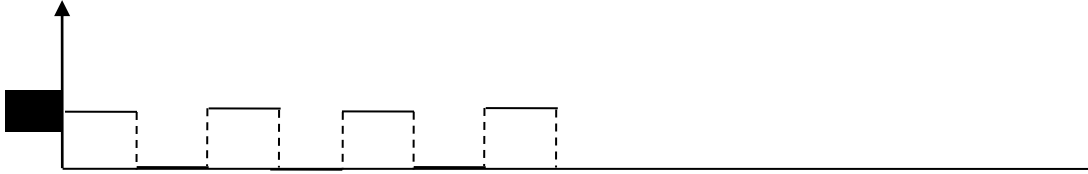
Let a negatively charged region be assigned the number '1' and a positively charged region the number '0'. The charge pattern on the lower surface can be represented by the following function:

$$\begin{aligned}\phi_1(x) &= H(x) - H(x-c) + H(x-2c) - \dots - H(x-(2m-1)c) \\ &= \sum_{k=1}^{2m} (-1)^{k-1} H(x-(k-1)c)\end{aligned}\quad (A2)$$

where

$$H(x) \equiv \begin{cases} 1 & x \geq 0 \\ 0 & x < 0 \end{cases}\quad (A3)$$

This represents a function of the form:



The charge pattern on the upper surface can be represented by the following function:

$$\begin{aligned}\phi_2(x) &= H(x) - H(x-\delta) + H(x-b-\delta) - H(x-2b-\delta) + \dots + H(x-(2n-1)b \\ &\quad - \delta) - H(x-2nb) \\ &= H(x) + [\sum_{j=0}^{2n-1} (-1)^{j-1} H(x-jb-\delta)] - H(x-2nb)\end{aligned}\quad (A4)$$

Note that these functions vanish for $x > 2mc = 2nb = L$ respectively. Also,

$$\phi_1(x) - \phi_2(x) = \begin{cases} 0 & \text{if the charge facing each sides are of the same sign} \\ \pm 1 & \text{if the charge facing each sides are of opposite sign} \end{cases}\quad (A5)$$

The total length for which the two surfaces have opposite charges is

$$L_A = \int_0^L [\phi_1(x) - \phi_2(x)]^2 dx \quad (\text{A6})$$

The total length for which the two surfaces have identical charge is therefore

$$L_R = L - L_A; \quad \alpha = 1 - L_A/L \quad (\text{A7})$$

By choosing $L=1$ we can compute α by calculating L_A . Now,

$$L_A = \int_0^L [\phi_1(x) - \phi_2(x)]^2 dx = \int_0^L [\phi_1^2(x) + \phi_2^2(x) - 2\phi_1(x)\phi_2(x)] dx \quad (\text{A8})$$

However, it is clear from the graph that

$$\int_0^L \phi_i^2(x) dx = \int_0^L \phi_i(x) dx = L/2 \quad i = 1, 2 \quad (\text{A9})$$

Eqs. (A8) and (A9) imply that

$$L_A = L - 2 \int_0^L \phi_1(x)\phi_2(x) dx \quad (\text{A10})$$

Using Eqs. (A2) and (A4), the integrand in Eq. (A10) can be written as

$$\begin{aligned} & \phi_1(x)\phi_2(x) \\ &= [H(x) - H(x - c) + \dots - H(x - (2m - 1)c)][H(x) + H(x - b - \delta) \\ & \quad - H(x - 2b - \delta) + \dots + H(x - (2n - 1)b - \delta) - H(x - 2nb)] \\ &= H(x) \sum_{k=1}^{2m} (-1)^{k-1} H(x - (k - 1)c) + [H(x) \sum_{j=0}^{2n-1} (-1)^{j-1} H(x - jb - \delta) - \\ & H(x - c) \sum_{j=0}^{2n-1} (-1)^{j-1} H(x - jb - \delta) + \dots - H(x - (2m - 1)c) \sum_{j=0}^{2n-1} (-1)^{j-1} H(x - \\ & jb - \delta)] - H(x - 2nb) \sum_{k=1}^{2m} (-1)^{k-1} H(x - (k - 1)c) \end{aligned} \quad (\text{A11})$$

The following integrals in Eq. (A11) are simple:

$$\int_0^L H(x) \sum_{k=1}^{2m} (-1)^{k-1} H(x - (k-1)c) dx = L/2 \quad (\text{A12a})$$

$$\int_0^L H(x - 2nb) \sum_{k=1}^{2m} (-1)^{k-1} H(x - (k-1)c) dx = 0 \quad (\text{A12b})$$

From Eqs. (A10) and (A11), we need to evaluate integrals of the form:

$$I_k \equiv \int_0^L H(x - kc) \sum_{j=0}^{2n-1} (-1)^{j-1} H(x - jb - \delta) dx \quad k = 0, 1, 2, \dots, 2m-1 \quad (\text{A13})$$

Note that

$$\int_0^L H(x - \alpha) H(x - \beta) dx = \int_0^L H(x - \alpha) H(x - \beta) dx = \int_{\beta}^L H(x - \beta) dx = (L - \beta) \quad (\text{A14})$$

where $L \geq \beta \geq \alpha \geq 0$.

We have already assumed that

$$c > b \Leftrightarrow \frac{n}{m} > 1 \quad (\text{A15})$$

This means that

$$kc = (p_k + \alpha_k)b \quad p_k = \lfloor kn/m \rfloor \quad 0 \leq \alpha_k < 1 \quad k = 1, 2, \dots \quad (\text{A16})$$

where $\lfloor \cdot \rfloor$ is the greatest integer function, e.g. $\lfloor 1.8 \rfloor = 1$. Now,

$$\begin{aligned} I_k &= \sum_{j=0}^{2n-1} (-1)^{j-1} \int_0^L H(x - jb - \delta) H(x - (p_k + \alpha_k)b) dx \\ I_k &= \sum_{j=0}^{p_k} (-1)^{j-1} [L - (p_k + \alpha_k)b] \\ &\quad + \sum_{j=p_k+1}^{2n-1} (-1)^{j-1} \int_0^L H(x - jb - \delta) H(x - (p_k + \alpha_k)b) dx \end{aligned}$$

$$= (L - kc) \sum_{j=0}^{p_k} (-1)^{j-1} + \sum_{j=p_k+1}^{2n-1} (-1)^{j-1} (L - jb - \delta)$$

$$\text{when } (\delta \leq \alpha_k b) \quad (\text{A17})$$

$$I_k = \sum_{j=0}^{p_k-1} (-1)^{j-1} [L - (p_k + \alpha_k) b] \\ + \sum_{j=p_k}^{2n-1} (-1)^{j-1} \int_0^L H(x - jb - \delta) H(x - (p_k + \alpha_k) b) dx$$

$$= (L - kc) \sum_{j=0}^{p_k-1} (-1)^{j-1} + \sum_{j=p_k}^{2n-1} (-1)^{j-1} (L - jb - \delta)$$

$$\text{when } (\delta > \alpha_k b) \quad (\text{A18})$$

Now,

$$\sum_{j=0}^{p_k} (-1)^{j-1} = \begin{cases} 0 & p_k = \text{odd} \\ -1 & p_k = \text{even} \end{cases} \quad (\text{A19})$$

$$\sum_{j=0}^{p_k-1} (-1)^{j-1} = \begin{cases} -1 & p_k = \text{odd} \\ 0 & p_k = \text{even} \end{cases} \quad (\text{A20})$$

and

$$\sum_{j=p_k+1}^{2n-1} (-1)^{j-1} (L - jb - \delta) = (L - \delta) \sum_{j=p_k+1}^{2n-1} (-1)^{j-1} + b \sum_{j=p_k+1}^{2n-1} (-1)^j j$$

$$= (L - \delta) \sum_{j=p_k+1}^{2n-1} (-1)^{j-1} + b \left[\sum_{j=1}^{2n-1} (-1)^j j - \sum_{j=1}^{p_k} (-1)^j j \right] \quad (\text{A21})$$

Similarly,

$$\sum_{j=p_k}^{2n-1} (-1)^{j-1} (L - jb - \delta) = (L - \delta) \sum_{j=p_k}^{2n-1} (-1)^{j-1} + b \left[\sum_{j=1}^{2n-1} (-1)^j j - \sum_{j=1}^{p_k-1} (-1)^j j \right] \quad (\text{A22})$$

Now,

$$(L - \delta) \sum_{j=p_k+1}^{2n-1} (-1)^{j-1} = \begin{cases} 0 & p_k \text{ odd} \\ (L - \delta) & p_k \text{ even} \end{cases} \quad (\text{A23})$$

$$(L - \delta) \sum_{j=p_k}^{2n-1} (-1)^{j-1} = \begin{cases} (L - \delta) & p_k \text{ odd} \\ 0 & p_k \text{ even} \end{cases} \quad (\text{A24})$$

Note that

$$\sum_{j=1}^{2n-1} (-1)^j j = -1 + (2 - 3) + (4 - 5) + \cdots + (2n - 2 - 2n + 1) = -n \quad (\text{A25})$$

$$\sum_{j=1}^{p_k} (-1)^j j = (p_k - 1)/2 - p_k = -(p_k + 1)/2 \quad \text{if } p_k \text{ is odd} \quad (\text{A26})$$

$$\sum_{j=1}^{p_k-1} (-1)^j j = (p_k - 1)/2 \quad \text{if } p_k \text{ is odd} \quad (\text{A27})$$

$$\sum_{j=1}^{p_k} (-1)^j j = p_k / 2 \quad \text{if } p_k \text{ is even} \quad (\text{A28})$$

$$\sum_{j=1}^{p_k-1} (-1)^j j = -p_k/2 \quad \text{if } p_k \text{ is even} \quad (\text{A29})$$

So

$$\sum_{j=1}^{2n-1} (-1)^j j - \sum_{j=1}^{p_k} (-1)^j j = -n + (p_k + 1)/2 \quad \text{if } p_k \text{ is odd} \quad (\text{A30})$$

$$\sum_{j=1}^{2n-1} (-1)^j j - \sum_{j=1}^{p_k} (-1)^j j = -n - p_k/2 \quad \text{if } p_k \text{ is even} \quad (\text{A31})$$

$$\sum_{j=1}^{2n-1} (-1)^j j - \sum_{j=1}^{p_k-1} (-1)^j j = -n - (p_k - 1)/2 \quad \text{if } p_k \text{ is odd} \quad (\text{A32})$$

$$\sum_{j=1}^{2n-1} (-1)^j j - \sum_{j=1}^{p_k-1} (-1)^j j = -n + p_k/2 \quad \text{if } p_k \text{ is even} \quad (\text{A33})$$

Thus,

when $(\delta \leq \alpha_k b)$

$$I_k = -\frac{L}{2} + b \cdot \frac{p_k+1}{2} \quad \text{if } p_k \text{ is odd} \quad (\text{A34})$$

$$I_k = -\frac{L}{2} + kc - b \cdot \frac{p_k}{2} - \delta \quad \text{if } p_k \text{ is even} \quad (\text{A35})$$

when $(\delta > \alpha_k b)$

$$I_k = -\frac{L}{2} + kc - b \cdot \frac{p_k-1}{2} - \delta \quad \text{if } p_k \text{ is odd} \quad (\text{A36})$$

$$I_k = -\frac{L}{2} + b \cdot \frac{p_k}{2} \quad \text{if } p_k \text{ is even} \quad (\text{A37})$$

Combining Eqs. (A10), (A11), and (A13) leads to the formula

$$L_A = 2 \sum_{k=0}^{2m-1} (-1)^{k+1} I_k \quad (\text{A38})$$

Figure A.1 compares the value of α computed by this method (with $\delta = 0$) with the relation $\alpha = \frac{mn-1}{2mn}$, showing the latter to be correct.

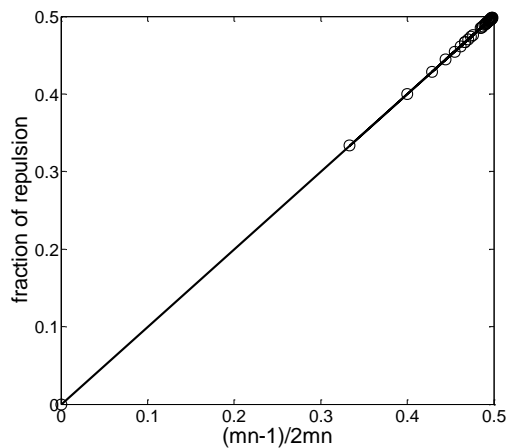


Figure A.1 $\frac{mn-1}{2mn}$ versus fraction of repulsive part for different m & n combinations.

Figures A.2 and A.3 show how α varies with shift δ . When $m=1$, the area fraction α is minimized when $\delta=0$; this corresponds to strongest attraction. Figure A.3 shows that there are several minima with varying δ when m is larger than one, e.g. $m=3,5,7\dots$. The fraction of α becomes a periodic function of the shift δ , and the minimum value of α is achieved when $\delta = \frac{2k}{m}b$ ($k=0,1,\dots,(m-1)/2$). In Chapter 2, we have picked $k=0$.

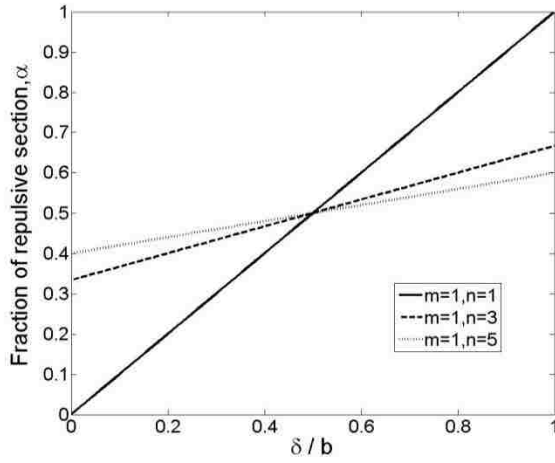


Figure A.2 The fraction α depends on the shift δ . For $m = 1$ and $n = 1, 3, 5, \dots$, it is minimized when $\delta = 0$.

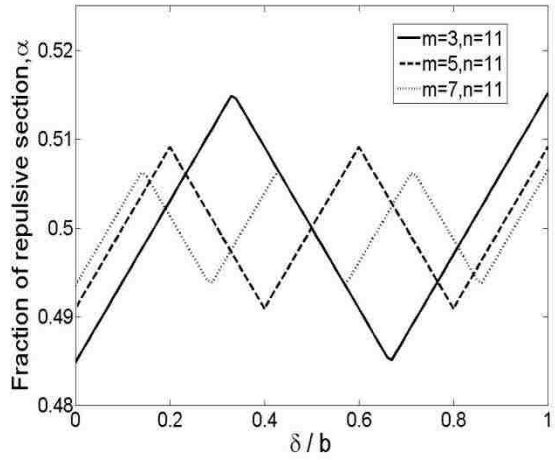


Figure A.3 The fraction α depends on the shift δ . For $m > 1$ and $n = 1, 3, 5, \dots$, it is a periodic function of, δ , with a minimum at $\delta = 0$.

Appendix B: Surface profilometry of the composite samples

The surface profile of the composite samples was measured using an interferometric optical profilometer (ZeGage, Zometrics, Inc). Figure B.1 shows that the surface undulates with small amplitude, of about $0.3 \mu\text{m}$ in this case, with the stiff regions being are slightly higher than the compliant ones.

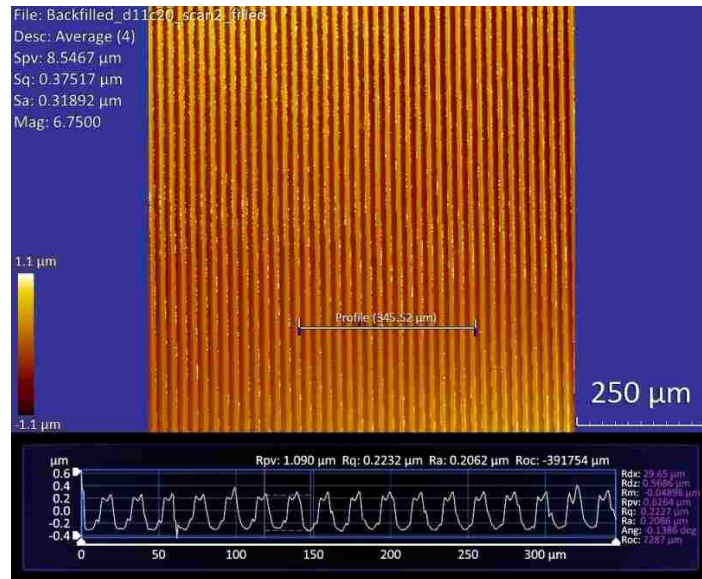


Figure B.4 Typical surface morphology of composite ridge/channel samples, showing that each stiff region is about $0.6 \mu\text{m}$ higher than its neighboring compliant region. The dimensions of the microstructures before backfilling are: channel depth $d = 10 \mu\text{m}$, interchannel spacing $c = 20 \mu\text{m}$.

Even though the top surface of each composite sample is not ideally flat and with alternating stiff and compliant materials, the surface roughness does affect the “auto-roughening” transition from the initial full contact to partial contact during sliding. Even when the top surface of the structured sample was over-backfilled, and finally results in a flat surface with a thin layer of compliant PDMS on top (Figure B.2), we can still see the separated contact regions (dark stripes in Figure B.2b ‘Sliding Phase’). Such strictly flat

surface cannot prevent the development of “auto-roughening” during sliding, which reveals that the contribution of minor roughness on the tested elastic surface of composite samples is very small compared to its internal structures and the variation of stiffness.

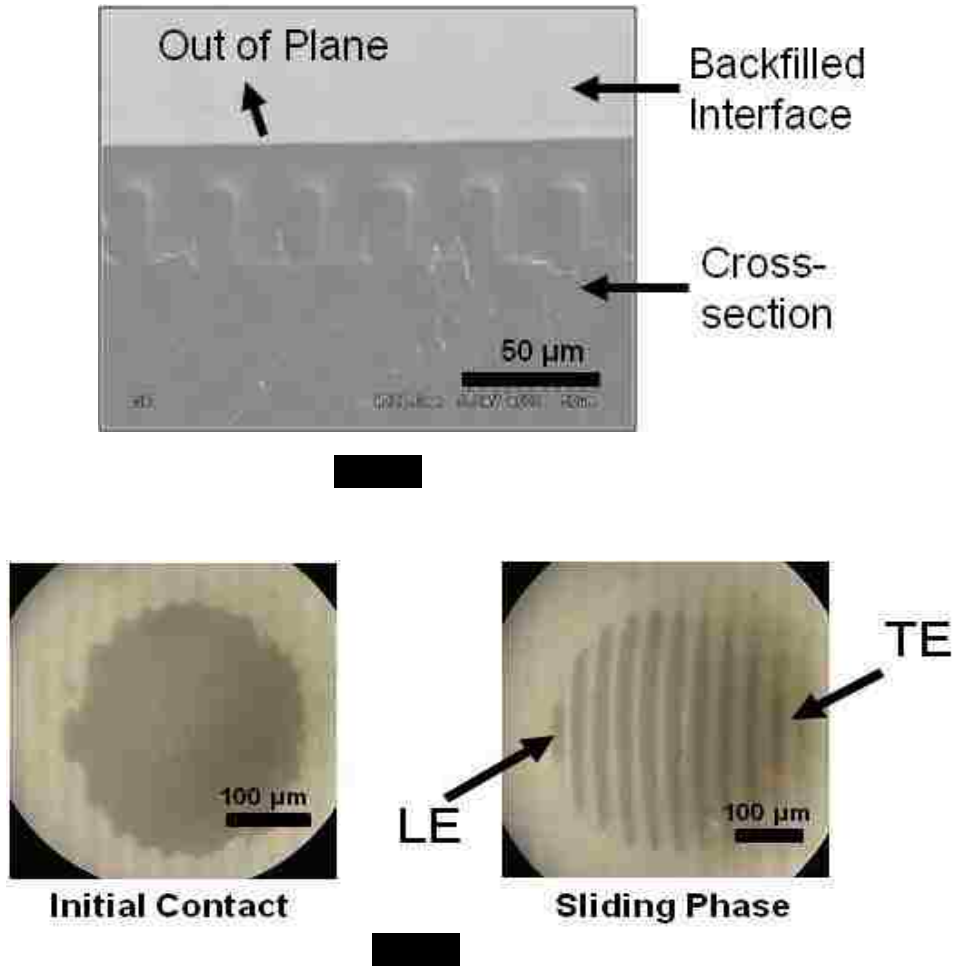


Figure B.5 Friction measurement on a over-backfilled 1-D micro-channel sample. (a) SEM image of an over-backfilled sample with a thin layer of flat compliant material on top of the 1D micro-structure (depth = 10 μm, spacing = 35 μm); (b) optical micrographs taken during a friction test on sample (a) still shows a transition from initially full contact (before sliding) to partial contact during sliding.

Appendix C: Friction test on backfilled fibrillar samples under large normal load

Figures C.1 and C.2 show the effect of increasing normal load on auto-roughening in the 2-D periodic samples. In the center region, contact is complete, whereas at its periphery contact is partial, especially at the trailing edge (Figure C.1b). Similarly, Figure C.2 shows that friction remains lower than both controls.

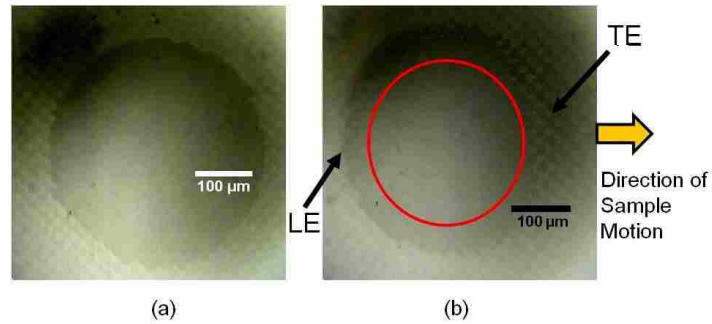


Figure C.6 Optical micrographs taken during a friction test on backfilled fibrillar samples ($h = 17.8 \mu\text{m}$, $s = 20 \mu\text{m}$). Observe the transition from (a) initially full contact (before sliding) to (b) partial contact during sliding; the red circle marks out that the region in which contact area is unbroken.

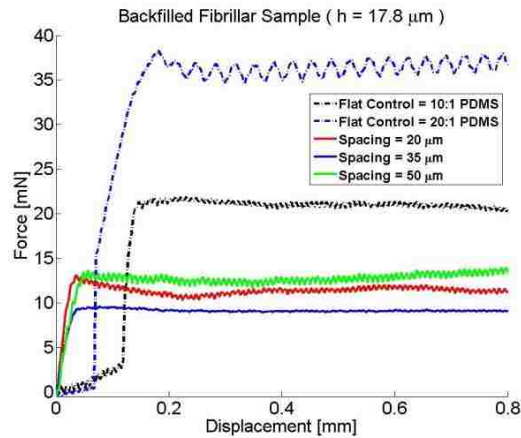


Figure C.7 Shear force as a function of shear displacement for 2-D periodic samples with spacing of 20, 35 and 50 μm and fixed fibril length $h = 17.8 \mu\text{m}$, and both flat control samples.

Appendix D: Estimating the mean and variance of the apparent shear stress

The frictional force F and the apparent contact area A are two independent random variables. The ratio of (F/A) is the shear stress. We wish to find approximations for expected value mean of the ratio $E(F/A)$ and variance $Var(F/A)$.

Using Taylor series expansions, the approximation of the mean of a quantity f which depends on F and A is ^{1,2}

$$E(f(F, A)) = f(EF, EA) + \frac{1}{2}\{f''_{FF}(EF, EA)Var(F) + 2f''_{FA}(EF, EA)Cov(F, A) + f''_{AA}(EF, EA)Var(A)\} + remainder \quad (D1)$$

where EF, EA denote the mean of F and A , $Var(F), Var(A)$ denote the variance of F and A , respectively, and $Cov(F, A)$ denotes the covariance of F and A .

For $f(F, A) = F/A$, $f''_{FF} = 0$, $f''_{FA} = -A^{-2}$, $f''_{AA} = \frac{2F}{A^3}$. Since F and A can be considered to be independent, $Cov(F, A) = 0$. Eq. (D1) implies that the mean of (F/A) is approximately

$$E\left(\frac{F}{A}\right) \approx \frac{EF}{EA} + \frac{Var(A)EF}{E^3A} \quad (D2)$$

Using the first order Taylor expansion, the variance is

$$Var(f(F, A)) = f'^2_F(EF, EA)Var(F) + 2f'_F(EF, EA)f'_A(EF, EA)Cov(F, A) + f'^2_A(EF, EA)Var(A) \quad (D3)$$

Since $f'_F = A^{-1}$, $f'_A = -\frac{F}{A^2}$, the variance of (F/A) is approximately

$$Var\left(\frac{F}{A}\right) \approx \frac{1}{(EA)^2}Var(F) + \frac{(EF)^2}{(EA)^4}Var(A) \quad (D4)$$

The results of Eqs. (D2) and (D4) can be used as an estimation for the mean and variance of apparent shear stress, and the standard deviation of the average shear stress is calculated as the square root of variance $Var(F/A)$.

Appendix E: Contact pressure on flat homogenous elastomer

First, we checked by simulating a homogeneous material that our model matches the expected results in that case (at the end of step one, no slip). When a rigid flat and frictionless punch is pressed into an elastic half-space, the contact pressure distribution is given by the following equation,³

$$p(x) = \frac{P}{\pi(a^2 - x^2)^{1/2}} \quad (\text{E1})$$

where P denotes the uniform normal pressure applied on the punch which has a rectangular shape of width $2a$ and sharp corners.

Figure E.1 shows the normalized contact pressure distribution for a flat rigid punch indenting a half-space homogenous elastomer (non-slip). The contact pressure that obtained by finite element simulation is in agreement with the theoretical prediction of Eq. (E1), except at the edge where the normal stress becomes unbounded.

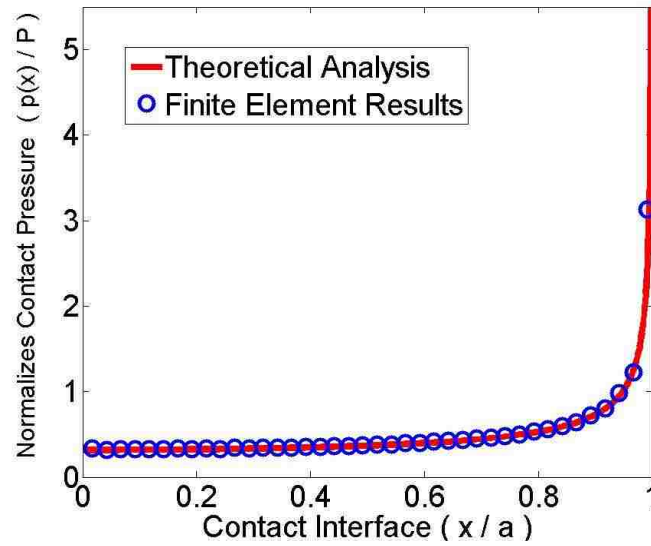


Figure E.8 Half-space contact pressure distribution along the interface due to indentation by a flat rigid punch. The interfacial position is normalized by half of the indenter width (a), and the contact pressure is normalized by the uniform normal load.

Appendix F: Simple beam model for auto-roughening

To gain insight into the mechanism of auto-roughening, we developed a simple model for the surface layer. The model explores the following idea. We conjecture that in the composite samples, the stiff pillars deform like beams whereas the compliant material acts as a shear layer connecting the beams and resisting their deformation.

Figure F.1 shows a free body diagram of a section of an elastic beam with moment M , distributed pressure P , distributed body moment m , transverse shear, V , and deflection w .

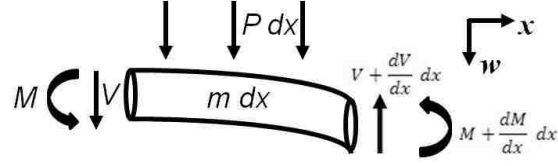


Figure F.9 Schematic illustration of an elastic beam under a uniformly distributed pressure P .

According to the moment-curvature relation, we have:

$$M = EI \frac{d^2 w}{dx^2} \quad (\text{F1})$$

where E is Young's modulus of the elastic material, I is the moment of inertia of the beam.

For a beam under a steady state, moment balance and force balance leads to:

$$\frac{dM}{dx} = -m - V \quad (\text{F2})$$

$$\frac{dV}{dx} = P \quad (\text{F3})$$

Combining Eqs. (F1) to (F3) give:

$$EI \frac{d^4 w}{dx^4} + \frac{dm}{dx} = -P \quad (\text{F4})$$

Figure F.2, shows the simplified model where the stiff pillars (I) are assumed to deform as beams. The compliant material (II) is assumed to serve primarily as a shear spring that exerts shear tractions onto the stiff beams. The shear forces, equal and opposite on two sides of the beam due to symmetry, are represented in the model by distributed body moments. The structure is periodic so by symmetry we study only a single period. The shear strain of the beam is:

$$\epsilon_{xy} = \frac{1}{2} \left(\frac{dw}{dx} \cdot \frac{h_1}{h_2} + \frac{dw}{dx} \right) = \frac{dw}{dx} \cdot \frac{h_1 + h_2}{2h_2} \quad (\text{F5})$$

Therefore, the shear stress can be expressed as:

$$\sigma_{xy} = 2G \cdot \epsilon_{xy} = G \frac{dw}{dx} \cdot \frac{h_1+h_2}{h_2} \quad (\text{F6})$$

The internal moment m is mainly generated by the shear stress, which is:

$$m = -\sigma_{xy} \cdot h_1 = -G \frac{dw}{dx} \cdot \frac{h_1(h_1+h_2)}{h_2} \quad (\text{F7})$$

When substituting Eq. (F7) into Eq. (F4), we can obtain the differential equation for the deflection of the stiff beam:

$$EI \frac{d^4w}{dx^4} - G \frac{h_1(h_1+h_2)}{h_2} \frac{d^2w}{dx^2} = -P \quad (\text{F8})$$

where G is the shear modulus of the compliant material. h_1 and h_2 denote the widths of stiff and compliant pillars, respectively, and l represents the length of each beam, as shown in Figure F.2a. In this case, $P = 0$, despite there is actual shear force at the edge ($x=l$).

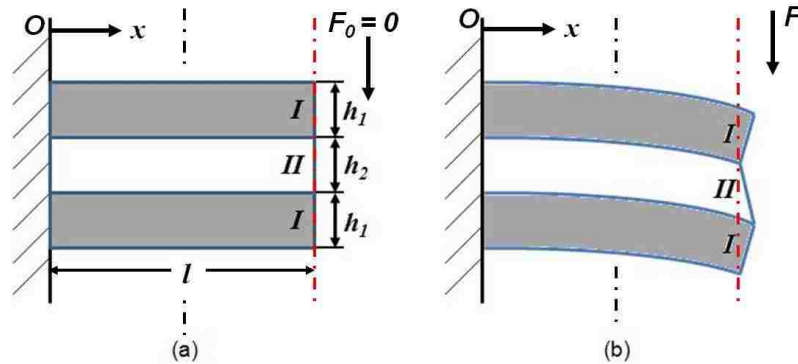


Figure F.10 Schematic illustration of a beam model for auto-roughening. Part I denotes the beam of stiff material and Part II denotes the compliant material served as a shear spring. (a) Initially each beam (Part I) is straight and connected by Part II without shear; (b) in the sliding phase, the beam of stiff material is bent and the surface becomes undulating after deformation.

To simplify the calculation, we define $\alpha^2 = \frac{Gh_1(h_1+h_2)}{Eh_2}$, and the dominate differential equation for this model can be normalized as:

$$\frac{d^4\bar{w}}{d\bar{x}^4} - \frac{d^2\bar{w}}{d\bar{x}^2} = 0 \quad (\text{F9})$$

where $\bar{x} = \alpha x, \bar{w} = \alpha w$.

Table F.1 Boundary conditions of analytical beam theory model

Position	Boundary Condition	Normalized Position	Normalized Boundary Condition
$x = 0$	$w = 0$	$\bar{x} = 0$	$\bar{w} = 0$
$x = 0$	$w' = 0$	$\bar{x} = 0$	$\bar{w}' = 0$
$x = l$	$w'' = 0$	$\bar{x} = \bar{l} = \alpha l$	$\bar{w}'' = 0$
$x = l$	$EIw''' - G \frac{h_1(h_1 + h_2)}{h_2} w' = F$	$\bar{x} = \bar{l} = \alpha l$	$\bar{w}''' - \bar{w}' = \bar{F}$

Table F.1 lists all the boundary conditions and their dimensionless form that applied to the model ($\bar{F} = \frac{F}{E\alpha^2}$ and $\bar{l} = \alpha l$). By substituting the normalized boundary conditions into Eq. (F9) gives us the final expression of the normalized deflection of the beam (stiff material).

$$\bar{w}(\bar{x}) = \frac{\bar{F} \cdot [e^{\bar{x}} - e^{(2\bar{l}-\bar{x})} + e^{2\bar{l}} - 1]}{1 + e^{2\bar{l}}} - \bar{F} \cdot \bar{x} \quad (\text{F10})$$

Note that, this simple beam theory is only apt for large modulus mismatch, since the shear strain is only considered by the compliant component.

References

- [1] Stuart, A.; Ord, K. *Kendall's Advanced Theory of Statistics*, 6th Edition, Vol. 1, Arnold: London, 1998, p351.
- [2] Elandt-Johnson, R. C.; Johnson, N. L. *Survival Models and Data Analysis* John Wiley & Sons: New York, 1980, p69.
- [3] Johnson, K. L. *Contact Mechanics* Cambridge University Press: New York, 1987.

Vita

Ying Bai was born on December 22, 1984 in Tianjin, China. He is the only child of Danlei Liang and Jingsheng Bai. He received a B.S. degree in Chemical Engineering from Tsinghua University, Beijing, China in 2006. After two years of graduate study, he was awarded a M.S. degree in Chemical Engineering, also from Tsinghua University in 2008.

He came to the United States for pursuing his Ph.D. degree and joined in Prof. Anand Jagota's research group in 2008. His research work involved the modification of mechanical properties of materials by surface topography, including both adhesion and friction, which were supported by the U.S. Department of Energy and Michelin[®] International Corporation, respectively. Parts of his research have been presented at Adhesion Society Meetings in 2012 and 2013, as well as the Materials Research Society Fall Meeting in 2012.

After completion of his requirements at Lehigh University, Mr. Bai intends to work as a postdoctoral research associate in the Polymer Science & Engineering Department at University of Massachusetts Amherst, working jointly in Prof. Todd Emrick and Prof. Alfred Crosby's groups.